POLITECNICO DI MILANO
MATHEMATICS DEPARTMENT "F. BRIOSCHI"
DOCTORAL PROGRAMME IN MATHEMATICAL MODELS AND METHODS IN ENGINEERING

NUMERICAL MODELING AND SIMULATIONS OF COMBUSTION PROCESSES IN HYBRID ROCKET ENGINES

Doctoral Dissertation of:
Alessandro Mazzetti

Supervisor:
Prof. P. Barbante

Tutor:
Prof. A. Frezzotti

Chair of the Doctoral Program:
Prof. R. Lucchetti

2014 - XXVI

Politecnico di Milano

Mathematics Department "F. Brioschi"

Doctoral Programme in Mathematical Models and Methods in Engineering

Author:
Alessandro MAZZETTI

Advisor:
Prof. Paolo F. BARBANTE

Tutor:
Prof. Aldo FREZZOTTI

Coordinator of the Doctoral Program:
Prof. Roberto LUCCHETTI

An expert is a man who has made all the mistakes which can be made in a very narrow field.
Niels Bohr

Ringrazio i miei genitori, che non soltanto mi hanno sostenuto in tanti anni di faticoso studio senza aver mai chiesto nulla in cambio, ma anche per avermi reso la persona che sono grazie al loro esempio di onestà, umiltà e intelligenza.

Ringrazio la mia compagna, per essere stata sempre al mio fianco con forza e dolcezza, per avermi sostenuto nei momenti più difficili ed essere sempre stata un punto di riferimento, giorno dopo giorno.

Ringrazio il Prof. Paolo Barbante per la supervisione durante il percorso di dottorato, di fondamentale importanza per la mia formazione scientifica e nondimeno personale, grazie a sempre costruttivi scambi di idee.

Ringrazio tutti i colleghi del dottorato, per aver sopportato le mie chiacchiere e lamentele, in particolare gli occupanti degli uffici al secondo piano, che sono, in ordine di "anzianità": Marco, Chiara, Gaetano, Raimondo, Anna, Andrea, Noemi, Matteo e Francesco.

Ringrazio M.Me Rigaux-Baumann, per il meraviglioso soggiorno dans le Royaume de Belgique e per l'eccellente gusto nell'arredamento.

Contents

List of Tables

List of Figures

Abstract

Hybrid rocket engines are nowadays considered the new frontier for space propulsion due to their low cost, operational flexibility and intrinsic safety. Their multiphase and multi-domain characteristics result in major difficulties in the numerical modeling of the phenomena involved. A reliable numerical model capable of predicting performance parameters and behavior of hybrid rockets is of major importance for the design of the next generation of hybrid rocket engines. In fact, nowadays, numerical simulations of combustion processes in hybrid rockets are only considered as a qualitative tool used to describe fluid-dynamic field inside the rocket. A research effort could be of major importance in order to change this trend, by obtaining results which are quantitatively accurate. This work faces this open research problem addressing the issues related to the simulation of such complex and interdependant problems as the ones present in the problem physics. The governing equations of the addressed problem are discussed, with particular attention to the accuracy of the closure models and of the boundary conditions. In fact, as the state of the art review reveals, several simplifications are generally applied in order to reduce problem modeling complexity. This work applies a more rigorous approach in the modeling of energy equation and in the modeling of closure terms. This requires the identification of adequate models for turbulence and chemical reactions. Moreover thermodynamic and transport properties of both the single reacting species and the gas mixture are to be modeled. Two different chemical models are evaluated in order to verify their coherence with problem physics. In addition, in order to address the limits of quasi-laminar chemistry versus a fully turbulent chemistry approach, both approaches for the chemistry source term are implemented and verified. In order to focus the work on the combustion modeling description, a modular object-oriented scientific computing environment is used: this is COOLFluID code, developed at von Karman Institute for Fluid Dynamics. Results are presented under an increasing problem complexity philosophy: at first non-reacting testcases are performed in both laminar and turbulent fashion, in order to obtain the base validation of the code. Reacting cases are then analyzed with increasing accuracy and model complexity, in order as:

1. simplified chemistry (two reactions, five species), fully laminar conditions;

2. simplified chemistry (two reactions, five species), turbulent governing equations and laminar chemistry source term;

3. more accurate chemistry (six reactions, nine species), turbulent governing equations and laminar chemistry source term;

4. more accurate chemistry (six reactions, nine species), turbulent governing equations and turbulent chemistry source term;

The case aforementioned are analyzed with a simplified boundary condition for the fuel inlet, with constant velocity of injected gaseous fuel based on experimental data, and at constant pressure. An accurate boundary condition considering the energy balance at the fuel inlet region is then described and implemented. This is mandatory in order to obtain an estimation of both local and average fuel regression rate, the most important parameter fot the comparison of hybrid rocket engines performance. An additional analysis is performed in order to assess the influence of both oxidizer mass flux and pressure increase on the combustion flowfield and on the regression rate. The effect of pressure on regression rate is yet an open research question in hybrid rocket science, with controversial interpretation. This work addresses the problem through the analysis of simulation results.

Objectives and Thesis Overview

Objectives

The main objective of present doctoral thesis is to realize a software tool able to simulate combustion processes in hybrid rocket engines. This involves the solution of viscous, compressible, turbulent, reacting, multi-species Navier-Stokes equations with conductive and convective heat transfer inside a suitable geometry for hybrid rocket engines. The governing equation system has to be closed with adequate models for turbulence and chemical kinetics. Consistent boundary conditions must be implemented in order to consider solid fuel regression rate. The implementation of physical models for combustion was realized within COOLFluiD code. This is a modular object-oriented scientific computing environment developed at von Kàrman Institute for Fluid Dynamics.

Thesis Overview

The general characteristics of hybrid rocket engines are described in **Chapter 1**. A short overview of the hybrid propulsion history is presented in this chapter, and the state of the art is presented in detail.

An introduction of numerical modeling in hybrid rockets is presented in **Chapter 2**, in which the open problems in CFD simulation of turbulent reacting flows are highlighted, and a review of the current state of the art is given.

Chapter 3 deals with the governing equations of turbulent reacting flows. In particular, the turbulent model closure is discussed in detail, and models for transport properties, thermodynamical properties and diffusion are described.

The COOLFluiD code used in this work is described in **Chapter 4**, together with a discussion of the original routines implemented.

Chapter 5 presents in detail the problem faced in this work, in term of geometry and initial and boundary conditions.

The obtained results are reported in **Chapter 6**, together with a detailed discussion of the different cases treated during the work.

Finally, **Chapter 7** gives some concluding remarks and outlines the future work envisaged for hybrid rocket simulations.

Chapter 1

General Features of Hybrid Rocket Engines

Nowadays, two are the most intriguing mid-long term challenges for space propulsion technology research and development. The first one is to achieve reliable, safe, flexible, low-cost and possibly mass access to space. The second one is to realize hypersonic aircrafts for goods and passenger transports which are able to cross intercontinental distances in a limited number of hours. Hybrid rockets might be the answer. They conjugate throttleability, precision and safety of liquid-fuelled rockets with design simplicity and low cost of solid-fuelled rockets. However a major drawback in hybrid rocket engines is the low regression rate of traditional fuels. This leads to inadequate performance levels in terms of thrust and specific impulse, forfeiting the reach for aforementioned achievements. Research effort to overcome low burning fuel speed is addressed towards testing of high energetic additives (micro- and nano- sized metals, metallic hydrides) and innovative paraffin-based fuel formulations. The latter rely on entrainment effect to increase performance: returning heat from the flame zone creates a molten layer on top of the fuel grain; injected oxidizer makes unstable this thin film and fuel spray is generated; these fuel droplets are then burned. Physical phenomena involved are very complex and difficult to model: the flow inside the rocket engine is turbulent, multi-species, multiphase and chemically reacting. Therefore main research is still fully experimental. The development of an accurate and reliable numerical tool could be a relevant contribution to research in this field. In fact this kind of tool can be used to analyze combustion processes in hybrid rockets, in order to get a better understanding of the problem physics. On the other hand the tool can be used as support and guidance for fuel formulation investigation and for engine performance estimation. Marxman et al. [1] investigated hybrid rocket combustion processes by analytical results of the classical boundary-layer theory, used to determine fuel regression rate from surface heat flux. Fuel regression rate is given by the exponential correlation $r_b = aG_{Ox}^n$, where G_{Ox} is the engine inlet flux of oxidizer and the exponent n is in the range 0.5-0.8. Such a simplified model is not able

to take into account phenomena linked to changes in the operating conditions, as chamber pressure oscillations and finite-rate chemistry. Chiaverini et al. [2] proposed a more accurate model, also accounting for radiative heat exchange. However this kind of models are only useful for qualitative and not quantitative information. Venkateswaran and Merkle [3] presented numerical simulation results for the hybrid rocket engine flowfield. This model solves compressible, viscous and unsteady 2D Navier-Stokes equations for a multi-species reacting, turbulent flow. Several other authors, such as Cheng [4] and [5] developed numerical models for the simulation of combustion processes in hybrid rockets. An increasing interest in CFD simulation for hybrid rocket engines is therefore noticeable. Numerical tools need further improvement in order to be fully able to predict the complex physical phenomena involved in hybrid combustion and overcome the very expensive, time consuming trials-and-error experimental approach.

This chapter presents a short introduction on hybrid rocket engines and on their current state of the art. Chapter 2 will deal with the importance of the numerical simulation of hybrid rocket combustion and will give some details on the state of the art of codes used so far.

1.1 Main Characteristics of Hybrid Rocket Engines

The main characteristic defining a hybrid rocket engine is that oxidizer and fuel are in different phases; in the typical configuration the fuel is a solid of cylindrical shape, while the oxidizer is injected into its port as a liquid spray or a gas. The resulting rocket motor shows features of both solid and liquid propellants systems.

The classical hybrid propulsion (HP) system (see Figure 1.1) uses a liquid oxidizer which is injected into a combustion chamber lined with a solid fuel. The oxidizer is stored in a separate tank and can be injected by using a pressurization system or a pump. Combustion occurs in a boundary layer above the fuel surface.

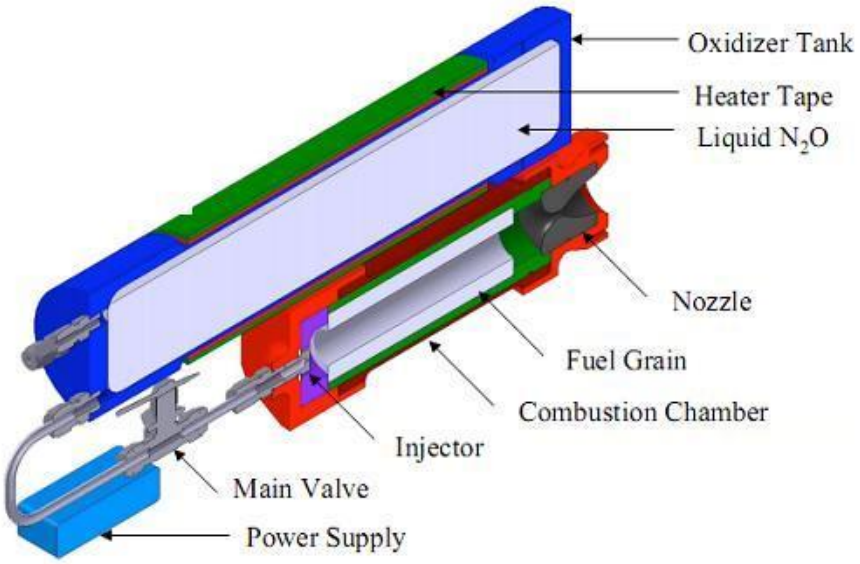

Figure 1.1: Sketch of the classical hybrid concept.

This is not the only possible configuration. Different fuel configurations are possible (cylindrical with single or multiple oxidizer port, plane slab) and several oxidizer/fuel couples are available. Also reverse hybrid rocket configuration exists: the fuel is in liquid or gaseous phase while the oxidizer is in solid phase.

The advantages of hybrid propulsion can be summarized in:

1. inherent safety: the system is nonexplosive since fuel and oxidizer are not premixed; no accidental ignitions due to shocks and vibrations (observed in solid propellants) are possible before the oxidizer injection; moreover, in case of emergency the shut down of the motor is possible simply stopping the oxidizer flux;

2. working flexibility: the hybrid system shows remarkable ease of throttling, multiple ignition possibility and extinguishing possibility;

3. working reliability: the system has notable costruction simplicity and shows high tolerance to cracks and debonds in the grain;

4. versatility in propellants selection;

5. low design and working costs;

6. low environmental impact;

7. good propulsive performance: the energy level of a liquid system is closely matched because the oxidizers are the same (the main reason for the lower I_s of solids is due to the lower energy of oxidizers in the solid propellant).

On the other hand, there are also some disadvantages:

1. low regression rate, due to the slow pyrolysis of the solid grain; this is the main shortcoming of this kind of propulsion and will be further discussed later;

2. low sensitivity of regression rate to operational conditions: this leads to the need of broad regression surfaces;

3. low combustion quality (rough, inefficient combustion with respect to solid propulsion and liquid propulsion);

4. longitudinal instabilities;

5. problems in large scale working.

1.2 Review of Hybrid Propulsion History

Thanks to their high degree of versatility, the past 80 years of research provides lots of examples of hybrid rockets applied to a large variety of applications including high performance space engines, large boosters, and various types of auxiliary power units [6].

The first efforts with hybrid propulsion date from the late 1930's, when the California Rocket Society designed and tested a hybrid rocket with static firing tests. The earliest significant effort in the mid-1940's was conducted by the Pacific Rocket Society which employed liquid oxygen (LOx) in conjunction with such fuels as wood, a wax loaded with carbon black, and finally a rubber base fuel.

An early analytical and experimental investigation in hybrids is that of G. Koore and K. Berman at General Electric initiated in the late 1940's, while several versions of the reverse hybrid were studied by both Thiokol and United Technology Center (CSD) in the mid-1960s utilizing hydrazine-based liquid fuels and such solid oxidizers as ammonium perchlorate, hydrazinium diperchlorate and nitronium perchlorate. This approach was abandoned because of poor combustion behavior and insufficient performance improvement to justify the difficulties experienced in compressing the charges.

In the mid-1960's, a series of NASA sponsored studies was begun devoted to high energy space engines. One concept was based on the utilization of the very energetic reaction between lithium and fluorine. This throttleable system burned smoothly and exhibited high performance with an efficiency of 93%, corresponding to a delivered vacuum impulse of about 380 s at an expansion ratio of 40.

Another approach to high performance space engines, also under a NASA contract, was based on the beryllium-oxygen-hydrogen reaction. This combination yields the highest performance calculated in a chemical rocket with readily available ingredients. Calculated I_s values of over 500 s in space were shown to be possible, but this investigation was later abandoned because of the anticipated toxicity problems that would be associated with the use of beryllium.

Various combinations of solid fuels and liquid oxidizers as well as liquid fuels and solid oxidizers have been experimentally evaluated for use in hybrid rocket motors. Because of the versatility in hybrid fuel selection, a very low cost combination was considered in the 60's, involving the use of discarded rubber tires. Although there was no technical objection to this approach, the collecting, sorting and grinding the tires would have made it too costly.

Several years later, NASA became interested in the feasibility of burning accumulated organic waste products (bits of clothing, uneaten food, human waste, etc.) in manned space stations to generate auxiliary power. Because of the variability in the trash composition, reliable physical properties could not be obtained and solid rocket motor operation was unacceptably hazardous.

An interesting comparison of different propellant selection alternatives has been done by Estey and Whittinghill [7] in 1992. They compared different promising combinations of fuel and oxidizer; for each combination, they took into account theoretical specific impulse, costs, handling hazards, materials compatibility. To choose the best combination for a given application, several different parameters must be taken in account: primarily performance and price, but also vehicle considerations like safety, packaging, feed system design, launch operations, ignition and thrust vector control.

None of these early tentatives resulted in a fully developed hybrid rocket system for practical application, because of the shortcomings of this technology - first of all, the overall low regression rate values. Nevertheless, things started to change in the mid 80's. The growing business worldwide in commercial satellites, which stimulated many industrialized nations to build their own versions of a space vehicle for placing communication satellites in orbit, caused a price competition and a search for a low cost approach to launch space vehicles. Moreover, the catastrophic failure of both a Shuttle flight (Challenger) and Titan 34D in 1986 with large solid motors resulted in a concern over the large solid, which stimulated NASA to sponsor a study of the use of hybrids for the Shuttle strap-on boosters. These two situations caused a significant revived interest in the hybrid rocket technology development.

The more interesting and relevant attempt to promote hybrid propulsion was certainly due to American Rocket Company (AMROC), in 1985 [8]. AMROC proved that it was possible to develop hybrid motors at a fraction of the cost of traditional rocket motors. It designed, manufactured and tested with success large liquid oxygen/hydroxyl terminated polybutadiene (HTPB) motors.

From 1999, Lockheed Martin and NASA/MSFC started a Hybrid Sounding Rocket program (HYSR), using a LOx-HTPB motor and launched to an altitude of 42 Km a sounding rocket. However, in spite of some impressive technological success, a high thrust hybrid motor based on LOx/HTPB combustion is far from being operational [9].

Currently, a suborbital, air-launched spaceplane designed for space tourism called SpaceShipTwo (SS2) is under development as part of the Tier 1b program under contract to The Spaceship Company, a California-based company that is wholly owned by its

sister company Virgin Galactic. SpaceShipTwo (see Figure 1.2) is carried to its launch altitude by a jet-powered mothership, the Scaled Composites White Knight Two, before being released to fly on into the upper atmosphere, powered by a rocket motor. It then glides back to Earth and performs a conventional runway landing. The spaceship was officially unveiled to the public on 7 December 2009 at the Mojave Air and Space Port in California. On 29 April 2013, after nearly three years of unpowered testing, the spacecraft successfully performed its first powered test flight. Virgin Galactic plans to operate a fleet of five SpaceShipTwo spaceplanes in a private passenger-carrying service, starting in 2014. The spaceplane could also be used to carry scientific payloads for NASA and other organisations.

Figure 1.2: Space Ship Two suborbital spaceplane designed for space tourism.

During the first years of this century, a new revival of hybrid motors was experienced; in fact, althought so many efforts were made during seven decades, only in recent years there have been promising progresses in terms of overcoming the intrinsic limits of hybrid propulsion.

The first use of paraffin fuel was envisaged by Arif Karabeyoglu at Stanford University. The first tests were reported in 2001 [10], and proved that regression rate increases, up to a factor of 3 to 5 over HTPB, when using paraffin and gaseous oxygen (GOx) axial injection. Altmann and Karabeyoglu are working with aerospace companies to consider the commercial feasibility of paraffin fuels in satellite launching systems.

With the increasing emphasis on safety, cost and versatility in missile systems, hybrid propulsion appears to be very promising for satisfying the current and future needs of the industry.

1.3 State of the Art

The peculiarities of hybrid propulsion lie on the characteristic combustion mechanisms. The combustion process in hybrid engines is very complex and includes several

coupled phenomena. As a result, the flow characteristics and the choice of ingredients strongly affect the combustion characteristics, and thus the motor performance.

1.3.1 Combustion Mechanisms and Scaling Effects

The basic combustion model for hybrid rocket engines using traditional fuels (see for example [6]) considers the boundary layer flow over the solid fuel surface and a flame zone inside the boundary layer near the fuel surface. Figure 1.3 shows a schematical representation of the mechanism.

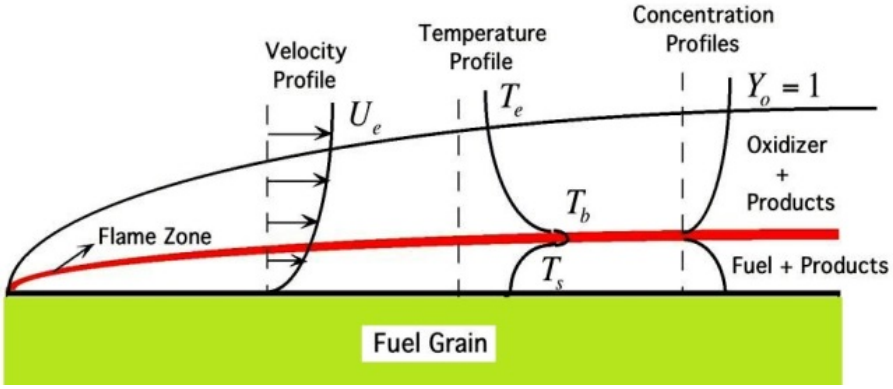

Figure 1.3: Scheme of the combustion mechanism in a classical hybrid system.

Heat transfer from the flame zone to the fuel surface leads to fuel pyrolisis. If traditional fuels are considered, this process leads to direct fuel sublimation, whose gaseous products enter the boundary layer. Here a combustion zone is formed and is the source of the heat flow to the surface to maintain fuel vaporization. This typical diffusion flame is approximately located at that point in the boundary layer where stoichiometric fluxes of fuel and oxidizer result. The thickness of that zone is dependent on the chemical reaction rates (see for example [1], [11]).

Several mechanisms are involved in the combustion: gasification of the oxidizer, sublimation of the fuel, diffusion of the gaseous fuel in the boundary layer flow, and chemical reactions in the flame. The gas coming from sublimated fuel has a temperature which is lower than the flame temperature: this has a cooling effect, unfavorable for the heat transfer process to the fuel surface; this effect is known as the *blocking effect*. Many formulas for the regression rate have been proposed. Today it is generally accepted [9] that the regression rate is weakly-dependent or not-dependent on the combustion pressure, at least at high oxidizer mass flux; and the regression rate r_b is generally calculated by the following expression

$$r_b = aG_{ox}^n \tag{1.1}$$

with

$$G = \frac{m_{ox}}{A_p}$$

Later this treatment was further refined to include the effects of radiation and chemical kinetics [12].

In recent years, Chiaverini and co-workers [13] investigated the solid-fuel regression rate and heat-transfer behavior in a lab-scale hybrid rocket motor burning HTPB and GOx. They developed semi-empirical equations to correlate the measured regression rates with the heat-transfer process.

The combustion processes in a hybrid engine are strictly dependent on the nature of the solid fuel: liquefying solid fuels potentially give higher regression rates than traditional solid fuels, but involve different combustion mechanisms if compared with traditional fuels (see for example [14], [15]).

The advantages of this kind of fuel were clearly explained with the researches by Karabeyoglu et. al. [10], [14], and [16]. The physical explanation of high combustion rate found was given by Karabeyoglu in his PhD at Stanford University, and, with D.Altman and B.J. Cantwell, the concept and the theory of liquefying hybrid fuels was established in 2002 [14]. The reason of that high regression rate is explained by a well known hydrodynamic phenomenon (figure 1.4). When a gas flows over a thin low viscosity liquid layer, there are unstable waves at the surface of the liquid and tiny droplets are produced at the tips of the waves. The droplets are entrained and burned in the oxygen flow. The key to high burning rate is this atomization effect, that substitutes the sublimation caused by heat transfer.

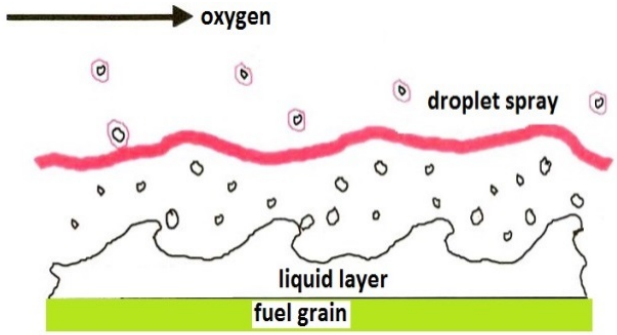

Figure 1.4: Scheme of the entrainment phenomenon.

This phenomenon leads to enhanced regression rate due to three reasons:

1. the burning specific area is enhanced by the presence of droplets;

2. traditional solid fuels are characterized by high pyrolisis temperature (near 800 °C) which leads from solid to gaseous phase, paraffin based fuels melt at low temperature (above 40°C) and then droplets evaporate - therefore paraffin based fuels require less heat to achieve the solid phase to gas phase conversion;

3. the blocking effect in this case is lower, which means the convective heat transfer is less impeded than it is with non-liquefying fuels.

The scaling effect for classical hybrids has been examined in several studies (see for example [17] and [18]), in which the authors took into account the most significant phenomena and effects in order to specify the main similarity conditions. It was concluded that oxidizer mass flow should be proportional to the motor port diameter, in order to preserve equality of O/F, Reynolds, Prandtl and Mach Number.
In a recent study by Kim et.al. [20], an investigation on the combustion characteristics of cylindrical multi-port grain of a traditionally fueled hybrid rocket motor was performed. In this study, several design parameters such as the port number, the distance between ports, and fuel type (polyethylene and polymethyl methacrylate) are experimentally analyzed using small and large size combustors. Small scale motor has diameter of 50 mm, while large scale motor has 96 mm. Oxidizer mass flux ranges from 10 kg/m^2s to 300 kg/m^2s for both cases. Large-scale (L) motor tests display a notable regression rate enhancement when compared to small-scale (S) motor tests. For instance, r_f increases from about 0.4 to about 0.6 mm/s (+50%) at 150 kg/m^2s oxidizer mass flux. For liquefying hybrid fuels the scaling effects seem to be much simpler than for classical hybrid fuels. In tests done at Stanford University with a 6,0 cm motor diameter and at NASA Ames Research Center with a 18,75 cm motor diameter, the authors conclude that the regression rate seems quite the same for small and large motors (experiments done with scale 1/3); moreover, no length or pressure effects were observed.

Tests done by authors of [19], with two motors having 1/10 thrust level, show that there is no scale effect on regression rate.

In a recent study by Kim et.al. [20], an investigation on the combustion characteristics of cylindrical multi-port grain of a hybrid rocket motor was performed. In this study, several design parameters such as the port number, the distance between ports, and fuel type (PE and PMMA) are experimentally analyzed using small and large size combustors. Small scale motor has diameter of 50 mm, while large scale motor has 96 mm. Oxidizer mass flux ranges from 10 kg/m^2s to 300 kg/m^2s for both cases. Large-scale (L) motor tests display a notable regression rate enhancement when compared to small-scale (S) motor tests. For instance, r_f increases from about 0.4 to about 0.6 mm/s (+50%) at 150 kg/m^2s oxidizer mass flux.

1.3.2 Combustion Instabilities

Some interesting researches were performed in order to investigate the pressure oscillations occurring in hybrid rocket engines, and confirmed there are pressure oscillations with all fuel types tested, althought the oscillations are never as dangerous as in solid rocket. However pressure oscillations make hybrid rockets unsuitable for manned missions (where instabilities could prove very harmful for crew and/or passengers) and strongly limit mission profiles. In a fundamental paper of 1968 [21], Woolridge and Marx-

man investigated the role of chemical kinetics in hybrid rocket instabilities. Their experiments confirmed the hypothesis that the pressure-dependent regression rate regime is particularly susceptible to combustion instability due to the coupling mechanism between regression rate and pressure. They also showed that metal loading does not appreciably affect either the steady-state pressure dependence or the combustion instability behavior of hybrid propellants. This led to the conclusion that gas-phase reaction kinetics is the limiting kinetic step in the overall combustion process.

In more recent years Wessel and co-workers [22] performed some testing for pressure oscillations by varying oxygen to fuel ratios, and by changing rocket motor geometries. The fuel tested in this work were high density polyethylene (HDPE), ultra-high-molecular-weight polyethylene (UHMW), paraffin wax, plexiglas, pure HTPB, and HTPB with 10% and 20% aluminum by weight. The authors concluded that probably air pockets in the fuel (due to mixing process) or unperfect curing would lead to higher pressure oscillations. The exploration of how the varying type of the fuel under the same oxygen to fuel ratios and rocket geometries effects the pressure oscillations in the hybrid rocket motor has yet to be explored.

Flame-holding combustion instabilities in hybrid rocket engines have been known to cause inefficiencies. Furthermore, this aspect is strictly related to ignition design.

Other researchers [23] have examined the combustion oscillations occurring in a hybrid rocket burning gaseous oxygen and paraffin wax through analysis of the chamber-pressure fluctuations measured by a high-speed transducer. Their results showed there were three distinct peaks in the chamber-pressure spectra at around 30, 100 and 350 Hz. The highest peak was associated with a non-acoustic mode at around 30 Hz, which is referred to as the dominant-hybrid oscillation. The other peaks in the chamber-pressure spectra were at around 100 and 350 Hz, and were associated with the Helmholtz mode and the longitudinal acoustic halfwave in the combustion chamber, respectively. Recent works from Karabeyoglu [24] and direct discussion with the author showed that it is possible to significantly reduce or solve hybrid rocket instabilities without compromising hybrid rocket simplicity, which is one of the main strengths of this application.

1.3.3 Regression Rate Enhancement

As previously mentioned, low regression rate is the main disadvantage of hybrid propulsion. Today the research on hybrid combustion is focused mainly on the aim of regression rate increase, in order to enhance the motor performance without losing the peculiar advantages offered by the hybrid propulsion. Fundamentally, the limit on regression rate for conventional hybrid fuels is set by the physical phenomena of heat and mass transfer from the relatively remote flame zone to the fuel surface. Heat transfer to the fuel surface is further reduced by the well-known blocking effect which is induced by the radial blowing of a large quantity of gas from the fuel surface. As a consequence, the regression rates of modern hybrids that utilize polymers as the fuel are much lower than conventional solid rocket burning rates. So far many techniques have been suggested

or tried to increase the regression rates of hybrids. These different approaches can be roughly divided in:

- chemical approach, based on the use of energetic additives in order to enhance solid fuel pyrolisis through an increase in gas enthalpy;
- fluid-dynamic approach, based on turbulence generation (enhance of thermal exchange coefficient);
- physical approach, based on droplets entrainment in the gas flow, which implies an enhanced combustion specific surface, together with a decreased convective heat transfer blocking factor and a lower heat absorption (due to the low melting temperature of the paraffins).

The chemical approach includes a number of different solutions. The most interesting results were found with ammonium perchlorate (AP) and with metal powders. Mixed hybrid propellants, like classical HTPB modified by AP and Aluminum additives, showed encouraging increase of regression rate up to 180% [9]; use of nano-sized Aluminum can also induce important improvements (more than 60%) in the regression rate [2], [25]. However the addition of AP can lead to a pressure dependence of the regression rate and the addition of nano-sized materials to performance loss and combustion instability. Mixed hybrid fuels is certainly an interesting method to improve regression rate but additional work is necessary in order to define a real hybrid mixed fuel able to deliver good performance.
In other works, different methods of enhancing the regression rate are compared [28]. In [29], the effects of the addition of ammonium perchlorate (AP) or aluminum in HTPB fuel, the variation of oxidizer-fuel ratio, and the variation of characteristic dimensions of fuel grain are presented. Apparently, both the addition of additives (AP and Al) and grain port diameter reduction are effective in enhancing the regression rate; anyway, the latter appears to be the more effective one.

A different approach is to increase the residence time in the combustion chamber by using swirl injectors or to increase the residence time and the burning area by imposing helical grain (see for example [26], [27]). The effect of swirl flow is to extend the residence time of oxidizer in the fuel grain. Meanwhile, it is well known that the embedded metal wires can increase the burning rate of a solid propellant by increasing heat transfer to solid fuel. Thus, metal wires may cause the same effect in a hybrid fuel by enhancing the regression rate.

In a study by Lee and co-workers [26], some experimental tests were done in order to investigate the enhancement of regression rate when swirl and the helical configuration are adopted together. Enhancement of regression rate up to 250% was achieved by combining both the helical grain configurations and swirl injector. However, the effect of swirl is limited in a region close to port inlet. This work suggests that the presence of swirl component of velocity at the inlet of the rocket motor influences the subsequent

flow evolution in terms of regression rate, but no attempt of finding an optimum strength of swirl was made.

Another interesting example is given by a recent work by Lazzarin and co-workers [62]. This paper presents a summary of the activities conducted at CISAS "'G. Colombo"'-University of Padova to analyse various methods aimed at increasing combustion efficiency in hybrid rockets. Combustion efficiency in hybrid rocket engines is usually low, due to the poor mixing of the core oxidizer flow with the gasified fuel entering the grain port from the grain walls. Two strategies have been investigated to enhance efficiency: the use of diaphragms and mixers located in the combustion chamber and a modification of the injection sub-system. These methods have been analysed using CFD results compared with experimental data.

Finally, the physical approach to increase the regression rate is based on liquefying fuels. Liquefying hybrid fuels, like paraffin, have high regression rate due to their peculiar process of combustion, as already mentioned. Very good results have been obtained at laboratory and semi-industrial scale motors; scaling effects seem to be negligible. This method seems very promising due to its simplicity, its low costs and the high regression rates obtained. Anyway, it is worth noticing that, in order to get good ballistic performance, it is necessary to work close to the optimum O/F ratio and to be sure that the combustion is complete in the combustion chamber. Moreover the mechanical characteristics of the fuel have to be good enough to sustain flight loads.

Several researchers have investigated the role of the injection system in the overall performance of a hybrid rocket engine. Some of the most interesting contributions can be found for example in [30], [27], as well as in the works of Carmicino and Russo Sorge [31], [32], [33].

In their work [31], an investigation is provided of the regression rate characteristics in a hybrid rocket where the oxidizer is injected through a conical axial nozzle rather than a stagnation chamber. Gaseous oxygen and polyethylene fuel cylindrical grains were used. The authors conclude that effects produced by the injection are of primary importance and worthy of further in-depth study. A nondimensional correlation involving the Reynolds number, the injector to grain diameter ratio, and the blowing number was developed with good accuracy of the predicted data. In any case, care has to be taken in the extrapolation of the results provided by this correlation to different rocket configurations. In particular, this correlation ignores the effect of grain length to diameter ratio, which certainly plays a fundamental role in the definition of the powers. The injection effect, indeed, is expected to be more important when the extent of the impinging region is larger compared to the grain length.

Gaseous oxygen and polyethylene fuel cylindrical grains were burned also in [32], where results from the firing tests conducted with two different injector configurations are discussed. The conical axial configuration provides highly stable combustion. A comparison with the results obtained with a radial injector is drawn in terms of average and

instantaneous regression rate, fuel consumption profiles, and combustion efficiency and stability. The authors concluded that the radial injector, at the same mass flux and pressure, produces lower regression rate, higher pressure oscillations and worse combustion efficiency.

In a more recent work [33], they also demonstrated that the oxidizer injection affects not only the regression rate of a hybrid rocket engine, but also its stability characteristics.

Chapter 2

Numerical Modeling in Hybrid Rocket Engines

2.1 CFD Modeling of Hybrid Rocket Engines

Hybrid rocket combustion flowfields involve fluid-dynamics coupled with combustion, turbulence, radiation, spray atomization, vaporization (if liquid oxidizers are used), fuel surface pyrolysis (if polymer-based fuels such as HTPB are used), and liquid fuel films (if liquefying fuels, such as paraffins, are used). Several approaches have been proposed for multiphase flowfields in the literature, including Eulerian-Eulerian homogeneous mixture formulation, Eulerian-Eulerian multifluid formulation, and Eulerian- Lagrangian approaches.

Analytical investigations of hybrid rocket combustion have usually been based on the classical boundary-layer analysis of Marxman et. al. [1] to determine the heat flux to the fuel surface and consequently the surface regression rate. Typically, the regression rate is given by simple correlations such as $r_b = aG_0^n$, where G_0 is the head end specific flow rate of the oxidizer and n is generally in the range 0.5-0.8. However, such simplified correlations cannot account for all the variations in operating conditions, chamber pressure, radiation, and finite-rate chemical kinetics. Some of these effects were characterized experimentally by Chiaverini et. al.[2], who also proposed a more complete model, which includes terms accounting for radiative fluxes. Nevertheless, such simplified models are limited to providing qualitative trends and are not adequate to give quantitative data.

Cheng et. al. [4] developed a model for hybrid rocket flowfields which solved the three-dimensional Reynolds averaged Navier-Stokes equations within a Lagrangian-Eulerian framework. In [5] Chen at al. successfully computed the 3D flowfield in two practical motor configurations and several simplified port configurations. Lin and Chiu [34] developed an Eulerian-Eulerian spray combustion model for hybrid rocket flowfields, focused on the post-atomization conditions prevailing in the downstream portion of the spray. These authors consider the spray as the oxidizer species. Computational results were

validated with experimental data, and parametric effects of droplet size and velocity distributions, as well as oxidizer flow rate on fuel regression and combustion efficiency, were performed.
In recent years, Venkateswaran [35] developed a computational model for hybrid rocket flowfields simulation. The model uses the complete time-dependent Navier-Stokes equations, coupled to auxiliary transport equations and physical submodels, and includes the effects of finite-rate chemistry, turbulence, gas-phase radiation, and coupling between gas and solid phases. The focus of [35] is the characterization of the fuel regression rate by comparing and calibrating the data using the experimental results by Chiaverini and co-workers [2], [13]. All the computational results shown in [35] are two-dimensional and obtained using a quasi-steady assumption, *e.g.* the fuel port dimensions were held fixed at values corresponding to different burning stages, and steady-state solutions were obtained to provide the instantaneous burning rates at the operating conditions. The quasi-steady assumption is adequate because the fuel surface regression rate is typically much smaller than the axial velocity in the port. A recent study by Coronetti and Sirignano [36] predicts the regression rate of the Hydroxyl-Terminated Poly-Butadiene (HTPB)/ Gaseous Oxygen formulation and its sensitivities to some operating parameters, such as combustion chamber pressure, oxygen inlet temperature, and mass flow rate. Furthermore, an analysis of other variables is used to explain the experimentally observed regression rate behavior. Particular emphasis is placed on the effect of the oxygen between the flame and the surface, which is considered responsible for the pyrolysis process enhancement.

In conclusion, it can be observed that even if many interesting (mostly qualitative) results were obtained so far, the use of CFD to model hybrid rocket flowfields need to be improved. In particular, further investigation is needed in order to model multiphase flows, turbulence, solid- and gas-phase interface combustion, and radiation. Liquefying fuels, such as paraffin-based fuels, have proved to result in a notable regression rate enhancement when compared to standard hybrid fuels, such as HTPB. This is due to the entrainment phenomenon, investigated by Karabeyoglu and co-workers [14]. Several experimental results confirm this conclusion [15] [37], but a reliable numerical simulation of paraffin based fuels is currently missing.

2.2 Numerical Codes: State of the Art

To date, the use of numerical tools to predict reacting turbulent flows is still largely qualitative, and the validation of the codes using experimental data is needed. The general requirements for a numerical code are reliability, accuracy and applicability to different: geometries, fuel/oxidizer couples and fluid-dynamic conditions. Actually no code is used as an accurate and reliable tool for prediction of the behavior of hybrid rocket motors concerning the fluid-dynamic field nor the fuel regression rate. Current employment of numerical simulation tools is about a qualitative analisys of the flow field and to give

general indications for the fluid-dynamics design of hybrid rocket engines. In particular, recent works deal with injectors, combustion chamber, and diaphragm design [38], [39], [40], [41]. For instance, [38] describes the use of a CFD code (ANSYS CFX 12) for the analysis of a hybrid rocket motor with a diaphragm placed in the combustion chamber in order to enhance rocket performance. This work follows the experimental campaign of Grosse [43] who tested the motor using nitrous oxide and paraffin wax as propellants. In a work by Nasuti and co-workers [44], numerical simulations of the flow in a GOX/HTPB hybrid rocket engine are carried out with a Reynolds averaged Navier-Stokes solver including detailed gas surface interaction mass and energy balances. Global mechanisms are considered for the gas-phase chemistry. Results show the role of the gas-phase chemistry modeling and surface boundary condition modeling on the solution. The effect of chemical species distribution in the wall region on a nozzle carbon-carbon wall is finally discussed. Analysing the literature results, it can be pointed out that the commercial codes (eg. ANSYS Fluent) used by several researchers are not the best choice for numerical simulation of reacting turbulent flows. In fact, although they are ready and relatively easy to use, with support offered by supplier, they are nevertheless a "'black box"' (no direct access to source code is possible) and lack of tailorability/customizability, which is fundamental in facing complex problems like hybrid rocket engines behavior. Therefore, the choice of *ad hoc* codes, such as COOLFluiD [87], OpenFOAM [45], SU^2 [46] appears to be the most promising in such an investigation. An example of customized simulation code is the use of OpenFOAM to create a moving regression surface to correctly simulate the fuel surface regression during combustion. Some preliminary results are shown in [48]. From the conclusions of present doctoral thesis and joint work, a need for further improvement of the simplified regression model arises. In fact, in order to achieve full modeling accuracy, an adequate boundary condition and pyrolisis law are needed to simulate the non-uniform regression behavior along the fuel grain due to differences in fuel surface temperature. Figure 2.1 shows the flowfield computed in three different positions of the regressing surface, from [48]. The advantage of this approach is that no quasi-steady approximation needs to be used; the cost is, of course, the need to develop and validate one's own code. This requires also the capability to continuously maintain and upgrade the code in order to keep an edge in the research field, with all the difficulties connected to a multi-user and multi-developer platform.

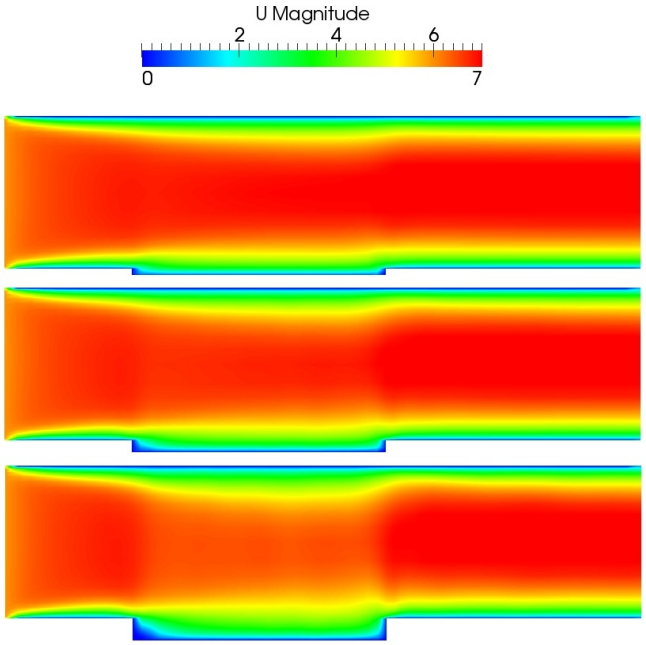

Figure 2.1: Computed flowfield for regressing fuel surface. From [47].

The future perspective of numerical simulation tools will be the prediction capability of fuel formulation behavior and performance in order to become a guide for experimental tests, with numerical results becoming not only qualitative but also quantitatively accurate. This could prove an important benefit not only from the academic point of view, but also from an industrial point of view. In fact, a reduced number of tests, limited by the directions given by numerical results, could prove both cost- and time-effective.

2.3 Open Challenges

The open challenges in the numerical simulation of complex, reacting, turbulent flows lies essentially in obtaining a reliable numerical tool which can be customized, as said, to several fluid-dynamics conditions, to different geometries, different reactants and different applications. In addition such a tool could prove useful in understanding the physical phenomena involved in the combustion processes of hybrid rocket engines, nowadays not yet fully understood, because of their multi-physics, multi-species and multi-phase nature with convective, conductive and radiative heat transfer. Optical techniques are also very difficult to apply on high-temperature, reacting conditions. Therefore it is often impossible to actually see what is happening inside an hybrid rocket combustion chamber. Again it is very difficult to assess analytically or experimentally the mutual interaction between many parameters, such as but not limited to: fluid-dynamics (e.g. pressure, speed, swirl effects), chemical formulation, solid particles, droplets, chamber geometry and acoustic instabilities. Numerical simulation tools could prove a benefit in order to increase the knowledge about such physics. The first step in obtaining such a tool is to

develop a code which is able to treat the different phenomena involved in hybrid rocket behavior. The following Chapters deal with a strategy to develop such a code.

Chapter 3

Governing Equations for Turbulent Reacting Flows

3.1 Introduction

In this chapter the equations we will use to model the turbulent flow field inside hybrid rockets are shown. For such equations *Favre-averaging* (or *mass-averaging*) will be introduced. This in order to avoid explicit modeling of density fluctuation correlations, such as $\overline{\rho' u'}$, which appear if the extended Reynolds averaging is used. Every generic quantity is splitted into a mass-weighted mean value and a fluctuating value:

$$Q = \widetilde{Q} + Q'' \tag{3.1}$$

With the following properties:

$$\widetilde{Q} = \frac{\overline{\rho Q}}{\overline{\rho}} \tag{3.2}$$

$$\widetilde{Q''} = \frac{\overline{\rho(Q - \widetilde{Q})}}{\overline{\rho}} = 0 \tag{3.3}$$

Favre-averaging equation (3.1) gives:

$$\widetilde{Q} = \widetilde{\widetilde{Q}} + \cancel{\widetilde{Q''}} = \widetilde{Q} \tag{3.4}$$

Equations (3.3) and (3.4) show two important properties useful for the following discussion:

1. the average taken over a fluctuating value is zero;
2. the average of the average is still an average value.

All gaseous species are treated under the perfect gas hypothesis. Therefore the ideal gas law is considered valid:

$$p = \rho R_{mix} T \tag{3.5}$$

where R_{mix} indicates the mixture gas constant, calculated using the single species molar masses M_i. The mixture density $\rho = \sum_{i=1}^{NS} \rho_i$ is calculated as the sum of species partial densities. In this case, mass fractions are defined as the ratio between the species partial density and the mixture density, such as $Y_i = \frac{\rho_i}{\rho}$. In this case i-th species molar concentration is also defined as the ratio between i-th species partial density and its molar mass, such as: $c_i = \frac{\rho_i}{M_i}$. Conservation equations for mass, chemical species, momentum and energy are described in the following sections. The first three do not represent a great challenge when expressed as Favre-averaged while the latter requires a more detailed description, also presented in the following sections.

3.2 Mass Conservation

In this work, the Einstein summation convention is used. Favre-averaged mass conservation equation remains formally identical to its instantaneous counterpart,

$$\frac{\partial \overline{\rho}}{\partial t} + \frac{\partial \overline{\rho}\widetilde{u}_j}{\partial x_j} = 0 \tag{3.6}$$

3.3 Momentum Conservation

Using Einstein summation convention, Favre-averaged momentum conservation equation results (for i=1,2,3):

$$\frac{\partial \overline{\rho}\widetilde{u}_i}{\partial t} + \frac{\partial \overline{\rho}\widetilde{u}_j\widetilde{u}_i}{\partial x_j} = -\frac{\partial \overline{\rho}\widetilde{u_i'' u_j''}}{\partial x_j} - \frac{\partial \overline{p}}{\partial x_i} + \frac{\partial \bar{\tau}_{ij}}{\partial x_j} + \overline{f}_i \tag{3.7}$$

Where $\bar{\tau}_{ij}$ is the laminar viscosity-dependant part of Reynolds stress tensor:

$$\bar{\tau}_{ij} = \mu\left(\frac{\partial \bar{u}_i}{\partial x_j} + \frac{\partial \bar{u}_j}{\partial x_i} - \frac{2}{3}\delta_{ij}\frac{\partial \bar{u}_k}{\partial x_k}\right) \tag{3.8}$$

Reynolds stress tensor $\overline{\rho}\widetilde{u_i'' u_j''}$ is also introduced and it has to be closed e.g. introducing turbulent viscosity μ_T and an additional term $\frac{2}{3}\bar{\rho}k$ (in order to obtain the correct value for the stress tensor trace, as in [54]), where k is the turbulence kinetic energy. The discussion for the closure of the turbulence terms will be introduced in the following sections. The term $\overline{f}_i$, representing body forces, can be neglected if these forces are not present in the considered physical system.

3.4 Chemical Species

In presence of a multi-component reacting gas mixture it is necessary to add the equation for the conservation of species' mass fraction $Y_k = \frac{\rho_i}{\rho}$:

$$\frac{\partial \overline{\rho}\widetilde{Y}_k}{\partial t} + \frac{\partial \overline{\rho}\widetilde{u}_j\widetilde{Y}_k}{\partial x_j} = -\frac{\partial \overline{\rho}\widetilde{u_j'' Y_k''}}{\partial x_j} - \frac{\partial \bar{\mathcal{F}}_j^k}{\partial x_j} + \bar{\dot{\omega}}_k \tag{3.9}$$

Where:

- $\overline{\rho}\widetilde{u_j''Y_k''}$ represents the turbulent flux of k-th species;
- $\bar{\mathcal{F}}_j^k = \overline{\rho V_{k,j} Y_k}$ represents the molecular diffusion flux of k-th species;
- $V_{k,j}$ represents the component of the diffusion velocity of species k in direction j, which is possible to express with Fick's diffusion law;
- $\bar{\dot{\omega}}_k$ represents the source term from chemical reactions.

In order for mass to be conserved, the following equations have to be valid:

$$\sum_k \overline{\rho}\widetilde{u_i''Y_k''} = 0, \quad \sum_k \bar{\dot{\omega}}_k = 0 \tag{3.10}$$

All the three terms on the right hand side of equation (3.9) have to be closed: usually the first two with a gradient transport hypothesis and the third through a chemical reaction model.

3.5 Energy Conservation

As previously stated, performing Favre-averaging on energy equation leads to results that are to be considered with more caution. The following definitions are used:

- $h_s = \sum_i Y_i h_{s,i}$, with $h_{s,i} = \int_{T_0}^{T} C_{p,i}\mathrm{d}T$, represents the sensible enthalpy per unit mass;
- $h_{st} = h_s + \sum_{k=1}^{NS} \Delta h_{f,k}^0 Y_k$ represents the static enthalpy, as sum of sensible enthalpy and enthalpy of formation;
- $h_t = h_s + \sum_{k=1}^{NS} \Delta h_{f,k}^0 Y_k + \frac{1}{2} u_i u_i$ represents the total enthalpy as sum of static enthalpy and kinetic energy;
- $e_s = h_s - \frac{p}{\rho}$ represents the sensible energy;
- $e_t = h_t - \frac{p}{\rho}$ represents the total energy;

Energy conservation equation can be expressed in terms of total energy:

$$\frac{\partial}{\partial t}(\rho e_t) + \frac{\partial}{\partial x_j}(\rho u_j e_t) + \frac{\partial}{\partial x_i}(p u_i) = -\frac{\partial q_j}{\partial x_j} + \frac{\partial}{\partial x_i}(\tau_{ji} u_i) + \dot{Q}_{ext} + \rho \sum_{k=1}^{N} Y_k f_{k,j}(u_j + V_{k,j}) \tag{3.11}$$

Where:

- τ_{ji} represents the total stress tensor;
- $f_{k,j}$ represents the body forces acting on species k in direction j;
- $\dot{Q}_{ext}$ represents the heat source term, not including the heat from chemical reactions;
- q_j represents the heat flux due to conduction, diffusion and Dufour effect.

It is possible to express equation (3.11) in the form of total enthalpy:

$$\frac{\partial}{\partial t}(\rho h_t) + \frac{\partial}{\partial x_j}(\rho u_j h_t) = \frac{\partial p}{\partial t} - \frac{\partial q_j}{\partial x_j} + \frac{\partial}{\partial x_j}(u_i \tau_{ij}) + \dot{Q}_{ext} + \rho \sum_{k=1}^{N} Y_k f_{k,j}(u_j + V_{k,j}) \quad (3.12)$$

Heat flux term can be expressed as in [51], [52], [50]:

$$q_j = -\kappa \frac{\partial T}{\partial x_j} + \rho \sum_{k=1}^{NS} h_k Y_k V_{k,j} + q_{Dufour} \quad (3.13)$$

The first term in (3.13) represents the heat conduction expressed by the Fourier Law; the second term is an heat term due to diffusion of species with different enthalpies (which is specific of multi-species conditions); the third term is the contribution of Dufour effect which is an heat diffusion effect due to gradients in mass concentrations. q_{Dufour} can be expressed as in [53]:

$$q_{Dufour} = -p \sum_i \alpha_i \underline{d}_i = p \sum_i \chi_i \underline{V}_i \quad (3.14)$$

and $\underline{d}_i$ is expressed as:

$$\underline{d}_i = \nabla X_i + (X_i - Y_i) \nabla \ln p - \frac{Y_i}{p} \left(\rho \underline{f}_i - \rho \sum_k Y_k \underline{f}_k \right) \quad (3.15)$$

The contribution of Dufour effect is negligible [50], in particular with respect to enthalpy contribution in combusting flows. Neglecting the body-forces dependant term for simplicity (it is also possible to use the assumption that no external body forces are present) and Favre-averaging, the total energy equation can be expressed as follows:

$$\frac{\partial \overline{\rho} \widetilde{e}_t}{\partial t} + \frac{\partial \overline{\rho} \widetilde{u}_j \widetilde{e}_t}{\partial x_j} + \frac{\partial}{\partial x_i}(p \bar{u}_i) = -\frac{\partial \overline{\rho} \widetilde{u_j'' e_t''}}{\partial x_j} + \frac{\partial}{\partial x_j}\left(\overline{u_i \tau_{ij}} - \overline{q}_j \right) + \bar{\dot{Q}}_{ext} \quad (3.16)$$

Or, in terms of total enthalpy:

$$\frac{\partial \overline{\rho} \widetilde{h}_t}{\partial t} + \frac{\partial \overline{\rho} \widetilde{u}_j \widetilde{h}_t}{\partial x_j} = -\frac{\partial \overline{\rho} \widetilde{u_j'' h_t''}}{\partial x_j} + \frac{\partial \bar{p}}{\partial t} + \frac{\partial}{\partial x_j}\left(\overline{u_i \tau_{ij}} - \overline{q}_j \right) + \bar{\dot{Q}}_{ext} \quad (3.17)$$

Usually in literature [49], [50] ideal gas law and Fourier law are applied in order to obtain a simplified energy or enthalpy equation expressed in terms of temperature.

Using equation (3.13) in equation (3.17), gives:

$$\frac{\partial \overline{\rho} \widetilde{h}_t}{\partial t} + \frac{\partial \overline{\rho} \widetilde{u}_j \widetilde{h}_t}{\partial x_j} = -\frac{\partial \overline{\rho} \widetilde{u_j'' h_t''}}{\partial x_j} + \frac{\partial \bar{p}}{\partial t} + \frac{\partial}{\partial x_j} \overline{u_i \tau_{ij}} + \frac{\partial}{\partial x_j}\left(-\lambda \overline{\frac{\partial T}{\partial x_j}} + \overline{\rho \sum_{k=1}^{N} h_k Y_k V_{k,j}} \right) + \bar{\dot{Q}}_{ext} \quad (3.18)$$

The most delicate term inside this equation is $\overline{\rho} \widetilde{u_j'' h_t''}$, representing the transport of total enthalpy fluctuations due to velocity fluctuations or, in other words, the turbulent transport of energy. In a turbulent reacting flow, where multiple mass fractions and turbulent kinetic energy contribution are present, it is important to check all the components

hidden in this turbulent energy term. In order to achieve this it is hereby presented the Favre-averaging of total enthalpy term, where the subscripts st and t indicate respectively static and total enthalpy.

$$v^2 = u_i u_i = (\widetilde{u}_i + u_i'')(\widetilde{u}_i + u_i'') = \widetilde{u}_i^2 + (u_i'')^2 + 2\widetilde{u}_i u_i'' \tag{3.19}$$

Total enthalpy is the sum of static enthalpy and kinetic contribution, thus using equation (3.19):

$$h_t = h_{st} + \frac{1}{2}u_i^2 = \widetilde{h}_{st} + \frac{1}{2}\widetilde{u}_i{}^2 + h_{st}'' + \frac{1}{2}u_i''^2 + \widetilde{u}_i u_i'' \tag{3.20}$$

Averaging equation (3.20), with the properties shown in equations (3.3) and (3.4) gives:

$$\widetilde{h}_t = \widetilde{\widetilde{h}}_{st} + \widetilde{\frac{1}{2}\widetilde{u_i^2}} + \cancel{\widetilde{h_{st}''}} + \widetilde{\frac{1}{2}u_i''^2} + \cancel{\widetilde{\widetilde{u_i}u''}_i} = \widetilde{h}_{st} + \frac{1}{2}\widetilde{u}_i{}^2 + \widetilde{\frac{1}{2}u_i''^2} \tag{3.21}$$

Where $\widetilde{\frac{1}{2}u_i''^2}$ represents the turbulence kinetic energy, as in [54] Using the definition from equation (3.1), applied to enthalpy:

$$h_t'' = h_t - \widetilde{h}_t \tag{3.22}$$

it is possible to obtain an expression for h_t'', subtracting equation (3.21) from equation (3.20):

$$h_t'' = h_{st}'' + \frac{1}{2}u_i'' u_i'' - \widetilde{\frac{1}{2}u_i'' u_i''} + \widetilde{u}_i u_i'' \tag{3.23}$$

Now, given:

$$\overline{\rho u_i h_t} = \bar{\rho}\widetilde{u}_i\widetilde{h}_t + \bar{\rho}\widetilde{u_i'' h_t''} \tag{3.24}$$

$$\bar{\rho}\widetilde{u_i'' h_t''} = \bar{\rho}\widetilde{u_i'' h_{st}''} + \bar{\rho}u_i''\widetilde{\frac{1}{2}u_j'' u_j''} - \bar{\rho}u_i''\widetilde{\frac{1}{2}u_j'' u_j''} + \widetilde{u_i'' u_j}'' u_j \tag{3.25}$$

Simplifying:

$$\bar{\rho}\widetilde{u_i'' h_t''} = \bar{\rho}\widetilde{u_i'' h_{st}''} + \bar{\rho}u_i''\widetilde{\frac{1}{2}u_j'' u_j''} - \cancel{\bar{\rho}\widetilde{u_i''}\frac{1}{2}\widetilde{u_j'' u_j''}} + \widetilde{u_i'' u_j}'' u_j \tag{3.26}$$

It is necessary now to better define static enthalpy term $\bar{\rho}\widetilde{u_i'' h_{st}''}$ from equation (3.26). In order to enhance readability, the notation for the summations $\sum_k$ is used in order to express the summation over the number of species, as $\sum_{k=1}^{NS}$. Static enthalpy of the mixture h_{st} is the sum of static enthalpy of the k-th species times the species' mass fraction:

$$h_{st} = \sum_k Y_k h_{st,k} \tag{3.27}$$

It has also to be considered that, as said, static enthalpy is the sum of two contributions: enthalpy from the integral of specific heat at constant pressure $h_{s,i} = \int_{T_0}^{T} C_p \mathrm{d}T$ and enthalpy from the heat of formation of the k-th species, which is constant:

$$h_{st} = \sum_k Y_k h_{st,k} = \sum_k Y_k \left(h_{s,k} + \Delta h_{0,k}\right) = \sum_k Y_k h_{s,k} + \sum_k Y_k \Delta h_{0,k} \tag{3.28}$$

It is possible to express h_{st} as:

$$h_{st} = \widetilde{h}_{st} + h''_{st} = \sum_k \left(\widetilde{Y}_k + Y''_k\right)\left(\widetilde{h}_{s,k} + h''_{s,k}\right) + \left(\widetilde{Y}_k + Y''_k\right)\sum_k \Delta h_{0,k} \tag{3.29}$$

Expliciting the terms inside parentheses in (3.29), h_{st} becomes:

$$h_{st} = \sum_k \widetilde{Y}_k\widetilde{h}_{s,k} + \sum_k \widetilde{Y}_k h''_{s,k} + \sum_k Y''_k\widetilde{h}_{s,k} + \sum_k Y''_k h''_{s,k} + \sum_k \widetilde{Y}_k\Delta h_{0,k} + \sum_k Y''_k\Delta h_{0,k} \tag{3.30}$$

Now static enthalpy h_{st} can be Favre-averaged, using the equivalence $\widetilde{\widetilde{Q}} \equiv \widetilde{Q}$:

$$\widetilde{h}_{st} = \sum_k^N \widetilde{Y}_k\widetilde{h}_{s,k} + \cancel{\sum_k \widetilde{Y}_k\widetilde{h''_{s,k}}} + \cancel{\sum_k \widetilde{Y''_k}\widetilde{h}_{s,k}} + \sum_k \widetilde{Y''_k h''_{s,k}} + \sum_k \widetilde{Y}_k\Delta h_{0,k} + \cancel{\sum_k \widetilde{Y''_k}\Delta h_{0,k}} \tag{3.31}$$

Cleaning up the simplified terms, it is obtained:

$$\widetilde{h}_{st} = \sum_k \widetilde{Y}_k\widetilde{h}_{s,k} + \sum_k \widetilde{Y''_k h''_{s,k}} + \sum_k \widetilde{Y}_k\Delta h_{0,k} \tag{3.32}$$

It is known that:

$$h''_{st} = h_{st} - \widetilde{h}_{st} \tag{3.33}$$

In fact, using equation (3.33) and thus subtracting equation (3.32) for $\widetilde{h}_{st}$ from equation (3.30) for h_{st}, gives:

$$h''_{st} = \sum_k \widetilde{Y}_k h''_{s,k} + \sum_k Y''_k\widetilde{h}_{s,k} + \sum_k Y''_k h''_{s,k} - \sum_k \widetilde{Y''_k h''_{s,k}} + \sum_k Y''_k\Delta h_{0,k} \tag{3.34}$$

It is now possible to multiply right hand terms from equation (3.34) by $\bar{\rho}u''_i$ then to perform Favre-averaging. In this step the summation over k is omitted for better understandability, but it will be adequately considered later on:

$$\widetilde{\bar{\rho}u''_i\widetilde{Y}_k h_{s,k}}'' + \widetilde{\bar{\rho}u''_i Y''_k}\widetilde{h}_{s,k} + \widetilde{\bar{\rho}u''_i Y''_k h''_{s,k}} - \cancel{\widetilde{\bar{\rho}u''_i Y''_k h''_{s,k}}} + \widetilde{\bar{\rho}u''_i Y''_k}\Delta h_{0,k} \tag{3.35}$$

It is possible to factorize common terms in (3.35):

$$\widetilde{\bar{\rho}u''_i\widetilde{Y}_k h_{s,k}}'' + \widetilde{\bar{\rho}u''_i Y''_k h''_{s,k}} + \widetilde{\bar{\rho}u''_i Y''_k}\left(\widetilde{h}_{s,k} + \Delta h_{0,k}\right) \tag{3.36}$$

It is now easy to re-apply the previously omitted summation and to re-arrange all the terms, getting the final expression for $\widetilde{\bar{\rho}u''_i h''_{st}}$:

$$\widetilde{\bar{\rho}u''_i h''_{st}} = \sum_k \left[\widetilde{\bar{\rho}u''_i Y''_k}\left(\widetilde{h}_{s,k} + \Delta h_{0,k}\right)\right] + \underbrace{\sum_k \widetilde{\bar{\rho}u''_i\widetilde{Y}_k h_{s,k}}'' + \sum_k \widetilde{\bar{\rho}u''_i Y''_k h''_{s,k}}}_{\text{A}} \tag{3.37}$$

It is possible to take outside of the sum over k-th chemical species and to collect the term $\bar{\rho}u_i''$ for highlighted A term:

$$\sum_k \widetilde{\bar{\rho}u_i''\tilde{Y}_k h_{s,k}}'' + \sum_k \widetilde{\bar{\rho}u_i''Y_k''h_{s,k}''} = \sum_k \widetilde{\bar{\rho}u_i''\left(Y_k h_{s,k}''\right)} \tag{3.38}$$

In equation (3.38) contributions from $\widetilde{Y}_k$ and Y_k'' were collected using the definition of Favre-averaging for Y_k: $Y_k = \widetilde{Y}_k + Y_k''$. With the expression for h_{st}'' now known from equation (3.37), it is possible to define all the contributions in h_t'' as requied to close equation (3.26):

$$\widetilde{\bar{\rho}u_i''h_t''} = \underbrace{\sum_k \left[\widetilde{\bar{\rho}u_i''Y_k''}\left(\widetilde{h}_{s,k} + \Delta h_{0,k}\right)\right]}_{1} + \underbrace{\bar{\rho}\sum_k \widetilde{u_i''Y_k''h_{s,k}''}}_{2a} + \underbrace{\bar{\rho}\sum_k \widetilde{u_i''\tilde{Y}_k h_{s,k}}''}_{2b} + \underbrace{\bar{\rho}\sum_i \widetilde{u}_j\widetilde{u_i''u_j''}}_{3a} \underbrace{\bar{\rho}\sum_i \widetilde{u_i''\frac{1}{2}u_j''u_j''}}_{3b} \tag{3.39}$$

It is now possible to discuss all the terms appearing in equation (3.39):

Term 1 represents the transport of mean static enthalpy with turbulent flux of mass;

Terms 2a, 2b can be added to each other and represent turbulent flux of specific enthalpy;

Term 3a represents the work performed by the Reynolds stress tensor, as defined in next section;

Term 3b is related to the transport of turbulence kinetic energy by velocity fluctuations;

It is important to discuss how all these terms can be modeled correctly. The work of Veynante and Vervisch [49] suggests that *Term 3b* could be neglected for $k << h$, far from being uncommon in combusting flows. However, for better accuracy, in this work this term will be considered in energy balance. Anyhow, the complete closure of governing equation will be discussed in the following sections.

3.6 Turbulence Model Closure

This system of equations is to be closed with models for turbulent fluxes of mass fractions, turbulent transport of energy, Reynolds stress tensor and chemical reaction source term. Turbulent transport of mass term is closed with a gradient hypothesis, defining turbulent Prandtl [55] and Lewis [49] numbers ($Pr_T \approx 0.7$ - 0.9, $Le_T \approx 1.0$ - 1.4), as shown in equation 3.40:

$$\widetilde{\bar{\rho}u_j''Y_k''} = -\frac{\mu_T}{Pr_T Le_T}\frac{\partial \tilde{Y}_k}{\partial x_j} \tag{3.40}$$

Reynolds stress tensor can be expressed using standard mean quantities for velocity components, under Boussinesq hypothesis, as:

$$\tau_{ij}^{R} = -\bar{\rho}\widetilde{u_i'' u_j''} = \mu_T \left(\frac{\partial \bar{u_i}}{\partial x_j} + \frac{\partial \bar{u_j}}{\partial x_i} - \frac{2}{3}\frac{\partial \bar{u_k}}{\partial x_k}\delta_{ij} \right) - \frac{2}{3}\bar{\rho}k\delta_{ij} \tag{3.41}$$

where k is the aforementioned turbulence kinetic energy. In literature Veynante, Vervisch [49] and Veynante, Poinsot [50] proposed a simple closure for turbulent transport of energy as $C_p \nabla T$. However in this work a more accurate approach is preferred. In fact the exact expression for turbulent transport of energy, from mass-averaged energy balance equation, is:

$$\begin{aligned} \bar{\rho}\widetilde{u_i'' h_t''} &= \underbrace{\sum_{k=1}^{NS} \left[\bar{\rho}\widetilde{u_i'' Y_k''} \left(\widetilde{h}_s^k + \Delta h_0^k \right) \right]}_{1} + \\ &+ \underbrace{\bar{\rho}\sum_{k=1}^{NS} \widetilde{u_i'' Y_k'' h_s^k}''}_{2a} + \underbrace{\bar{\rho}\sum_{k=1}^{NS} \widetilde{u_i'' Y_k^k h_s}''}_{2b} - \underbrace{\tilde{u_j}\tau_{ij}^{R}}_{3a} + \underbrace{\bar{\rho}\widetilde{u_i'' \frac{1}{2} u_j'' u_j''}}_{3b} \end{aligned} \tag{3.42}$$

Referring to the terms appearing in equation 3.42: *term 1* represents the transport of mean static enthalpy with turbulent flux of mass; *terms 2a* and *2b* can be added to each other and represent turbulent flux of specific enthalpy; *term 3a* represents the work performed by the Reynolds stress tensor; *term 3b* is related to the transport of turbulence kinetic energy by velocity fluctuations. The closure for turbulent transport of mass from equation 3.40 is consistently used in *term 1* of equation 3.42. This gives *Term 1* in equation 3.43, which is the same as in equation 3.42, with specific and formation enthalpies of each species expressed as static enthalpy. It is also possible to add *Term 2a* and *2b* from equation 3.42, obtaining *term 2* in equation 3.43 with a gradient closure. *Terms 3a* and *3b* from equation 3.42 are closed as in Wilcox in [54], resulting in *term 3* of equation 3.43.

$$\bar{\rho}\widetilde{u_i'' h_t''} = \underbrace{-\frac{\mu_T}{Pr_T Le_T}\frac{\partial \tilde{Y_k}}{\partial x_j}\left(\tilde{h}_t^k\right)}_{1} \underbrace{-\frac{\mu_T}{Pr_T}\frac{\partial \tilde{h_s^k}}{\partial x_j}}_{2} + \underbrace{\left(\mu + \frac{\mu_T}{\sigma_k}\right)\frac{\partial k}{\partial x_j}}_{3} \tag{3.43}$$

3.6.1 Turbulent Viscosity Model

In order to close the system for the conservation equations, it is necessary to introduce a turbulence model for the determination of the turbulent viscosity coefficient μ_T. The choice for present work is Wilcox [54] $k-\omega$ model, which gives better results for reacting flows in internal geometries at low Mach numbers with respect to, for instance, the $k-\epsilon$ model [54]. Therefore turbulent viscosity is defined as:

$$\mu_T = \bar{\rho}\frac{k}{\omega} \tag{3.44}$$

where k is the turbulence kinetic energy and ω is the turbulence specific dissipation rate (the characteristic frequency of turbulence). Transport equations are to be resolved for

turbulence kinetic energy and specific dissipation rate, from [54], [50]:

$$\frac{\partial}{\partial t}\left(\bar{\rho}k\right) + \frac{\partial}{\partial x_j}\left(\bar{\rho}\tilde{u_j}k\right) = P - \beta^{\star}\bar{\rho}\omega k + \frac{\partial}{\partial x_j}\left[\left(\mu + \sigma_k\frac{\bar{\rho}k}{\omega}\right)\frac{\partial k}{\partial x_j}\right] \tag{3.45}$$

and:

$$\frac{\partial}{\partial t}\left(\bar{\rho}\omega\right) + \frac{\partial}{\partial x_j}\left(\bar{\rho}\tilde{u_j}\omega\right) = \frac{\gamma\omega}{k}P - \beta\bar{\rho}\omega^2 + \frac{\partial}{\partial x_j}\left[\left(\mu + \sigma_\omega\frac{\bar{\rho}k}{\omega}\right)\frac{\partial \omega}{\partial x_j}\right] \tag{3.46}$$

Where P is defined as:

$$P = \tau_{ij}\frac{\partial \bar{u}_i}{\partial x_j} = \left\{\mu_T\left[\left(\frac{\partial \bar{u_i}}{\partial x_j} + \frac{\partial \bar{u_j}}{\partial x_i}\right) - \frac{2}{3}\frac{\partial \bar{u_k}}{\partial x_k}\delta_{ij}\right] - \frac{2}{3}\bar{\rho}k\delta_{ij}\right\}\frac{\partial \bar{u}_i}{\partial x_j} \tag{3.47}$$

Closure coefficients for the $k-\omega$ two-equations turbulence model from are listed as follows:

$$\gamma = 13/25, \quad \beta = \beta_0 f_\beta, \quad \beta^* = 9/100, \quad \sigma = 1/2, \quad \sigma^* = 3/5, \quad \sigma_{ab} = 1/8 \tag{3.48}$$

$$\beta_0 = 0.0708, \quad Pr_t = 0.9 \tag{3.49}$$

$$\sigma_d = \begin{cases} 0, & \text{if } \frac{\partial k}{\partial x_j}\frac{\partial \omega}{\partial x_j} \leq 0 \\ \sigma_{d0} = 1/8, & \text{if } \frac{\partial k}{\partial x_j}\frac{\partial \omega}{\partial x_j} > 0 \end{cases} \tag{3.50}$$

$$f_\beta = \frac{1 + 85\chi_\omega}{1 + 100\chi_\omega}, \quad \chi_\omega = \left|\frac{\Omega_{ij}\Omega_{jk}\hat{S}_{ki}}{(\beta^*\omega)^3}\right|, \quad \hat{S}_{ki} = S_{ki} - \frac{1}{2}\frac{\partial \tilde{u}_m}{\partial x_m}\delta_{ki} \tag{3.51}$$

$$\Omega_{ij} = \frac{1}{2}\left(\frac{\partial u_i}{\partial x_j} - \frac{\partial u_j}{\partial x_i}\right), \quad S_{ij} = \frac{1}{2}\left(\frac{\partial u_i}{\partial x_j} + \frac{\partial u_j}{\partial x_i}\right), \tag{3.52}$$

Equation (3.52) represents mean-rotation and mean strain-rate tensors. As a remark, the term χ_ω is equal to zero for 2D flows. In addition, as expressed by (3.49), turbulent Prandtl number is considered constant and equal to 0.9 and turbulent Lewis number equal to 1.0.

3.6.2 Chemistry Closure

This work presents two different closure models for chemical reactions' source term. The first one, as in Venkateswaran and Merkle [56] considers chemical reactions in a pseudo-laminar condition, the Perfectly Stirred Reactor (PSR) hypothesis. The second one, as in Golovitchev [57], considers chemical reactions in a fully turbulent condition. This is the Partially Stirred Reactor (PaSR) approach. Each one of this schemes will be discussed in detail in the next sections.

Perfectly Stirred Reactor (PSR)

A simpler approach to obtain chemical source term closure is the PSR hypothesis, as:

$$\bar{\dot{\omega}}_k = M_k \sum_{r=1}^{NR} \left(\nu''_{k,r} - \nu'_{k,r}\right) \left\{ k_{f,r} \prod_{i=1}^{NS} \left[\frac{\bar{\rho}\tilde{Y}_i}{M_i}\right]^{\nu'_i} - k_{b,r} \prod_{i=1}^{NS} \left[\frac{\bar{\rho}\tilde{Y}_i}{M_i}\right]^{\nu''_i} \right\} \tag{3.53}$$

Equation (3.53) expresses the net source term for each chemical species as the sum over the NR reactions (that the considered species participate in) of the rate of production and destruction using the Law of Mass Action. This law has dependance on the stoichiometric coefficients ν (and their difference), on forward and backward reaction rates $k_{f,b}$ and on species concentration $c_k = \frac{\bar{\rho}\tilde{Y}_i}{M_i}$.

Partially Stirred Reactor (PaSR)

In order to obtain more accurate results for turbulence-chemistry interaction, a Partially Stirred Reactor (PaSR) approach is also implemented. This approach is of a far more recent use for hybrid rocket numerical simulations, as in Lazzarin et al. [62] or Sirignano and Coronetti [36] with respect to PSR. Initially proposed by Golovitchev [57], PaSR model overcomes the simplified approach given by a pseudo-laminar chemistry by considering that only a partial volume of each computational cell is affected by the presence of a chemically reacting zone. In PaSR approach, combustion is considered as the combination of two different processes. The first one considers the change of concentration from c_0 (unburnt gases) to c, burnt gases. The second one considers the turbulent mixing of burnt gases with oncoming fresh reactants, therefore with the change of concentration from c to c_1. Figure 3.1 shows a conceptual diagram of PaSR reactor. Reacting volume

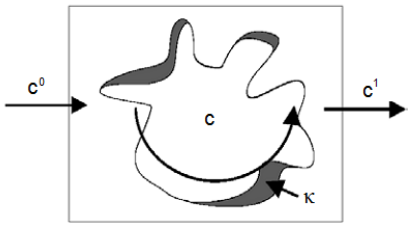

Figure 3.1: PaSR reactor conceptual scheme

fraction of each computational cell is proportional to the ratio κ of chemical reaction time τ_c and total time $\tau_c + \tau_{mix}$, as shown in [63]. The chemistry source term is modified using the aforementioned time ratio κ, as:

$$\bar{\dot{\omega}}_T = \kappa \bar{\dot{\omega}} = \frac{\tau_c}{\tau_c + \tau_{mix}} \bar{\dot{\omega}} \tag{3.54}$$

Several definitions for these characteristic times are possible, as proposed by Golovitchev [57] and [63], Nordin [64] or Fureby and Sabel'nikov [65]. All literature sources propose the

choice of a single chemistry characteristic time, common to all chemical reactions. However, the choice of a common time for a given group of chemical reactions, which might be very different in nature (e.g. oxidations and decompositions), can be difficult. This because the characteristic time of each reaction might be very different from the others. Moreover a poor choice of chemical characteristic time could compromise model accuracy. This work tries to overcome these problems with a novel approach: a multi-time PaSR model. For each chemical reaction one time is chosen from the chemical system jacobian matrix, therefore representing the sensitivity of a given reaction to variations in concentration for a given chemical species. For reactions depending on several concentrations, the one corresponding to the smallest time is chosen and calculated in dependence of the sensitivity of the r-th reaction rate to the variations of k-th chemical species partial density (or concentration, being these two quantities strictly linked):

$$\frac{1}{\tau_c} = -\frac{\partial f_r\left(\rho_k, T\right)}{\partial \rho_k} \tag{3.55}$$

Coherently with equation (3.54), this choice is due to the consideration that the influence of turbulence is greater if the chemical time is small enough. On the other hand if the chemistry time is big enough, the time ratio κ could not be influenced by turbulence because τ_{mix} becomes negligible with respect to τ_c and κ ratio becomes close to unity. Therefore the smallest chemical time is more influenced by turbulence while the largest chemical time is the least influenced by turbulence. For the considered reaction scheme this results in a characteristic chemical time for each one of the six reactions involved. Of coures this is one of the possible approaches, which the author considers more accurate with respect to the single-time PaSR. The turbulent mixing time is chosen accordingly to [64], therefore:

$$\tau_{mix} = C\frac{k}{\epsilon} = \frac{1}{C_\mu \omega} \tag{3.56}$$

C is a model constant, with values ranging from 0.001 to 0.03. The value chosen for this work is 0.005. C_μ is the turbulence model constant 0.09.

3.7 Models

In order to complete the closure for previously described equation system, it is necessary to use thermodynamic and transport properties from available scientific literature. Each property has to be either collected as data table or, for global mixture parameters, reconstructed through a specific correlation. In particular, data needed are:

1. chemical model composed of an adequate number of reactions;
2. molecular viscosity of single species μ_i and for the mixture μ;
3. thermal conductivity of single species κ_i and for the mixture κ;

4. single reacting species enthalpy h_k;
5. mixture specific heat at constant pressure c_p;
6. the molecular diffusion flux $\bar{\mathcal{F}}_j^k$, by an adequate model.

3.7.1 Chemical Model

In order to choose the correct chemical model, an assumption has to be made about pyrolisis products of the considered fuel (HTPB). Accordingly to [58] and [59], main product during pyrolisis process is gaseous 1,3 butadiene (C_4H_6). The first approach is to implement a very simple chemical model for the combustion of butadiene gas. As shown in [56], it is possible to introduce a two step, five species combustion model:

$$\begin{aligned} C_4H_6 + 3.5O_2 &\xrightarrow{k_{f1}} 4CO + 3H_2O \\ CO + 0.5O_2 &\underset{k_{b2}}{\overset{k_{f2}}{\longleftrightarrow}} CO_2 \end{aligned} \tag{3.57}$$

Where reaction rates k_{f1}, k_{f2} and k_{b2} are expressed as Arrhenius functions which consider also the effect of species concentrations:

$$k = AT^n \cdot exp\left[\frac{Ea}{RT}\right] \prod_{k=1}^{NS} [c_k]^m \tag{3.58}$$

Values are found in [60] and summarized in the following table:

Table 3.1: Chemical reaction scheme, 2 reactions

k	**A** $[\mathbf{m^3/mol \cdot s}]$	**Ea [cal/mol]**	**n**	**Reaction Rate**	**a**	**b**	
k_{f1}	8.80×10^{11}	-30000	0	$k_1[C_4H_6]^a[O_2]^b$	0.15	1.60	-
k_{f2}	$1.00 \times 10^{14.6}$	-40000	0	$k_2[CO]^a[H_2O]^b[O_2]^c$	1.00	0.50	0.25
k_{b2}	5.00×10^{08}	-40000	0	$k_3[CO_2]^a$	1.00	–	–

Even if representing a possibly adequate and relatively simple starting point, the two-step reaction mechanism could prove excessively simplified. A more detailed six reaction, nine species global reaction mechanism from Jones and Lindstedt [61] is found and chosen as a compromise between number of chemical species involved and computational cost. Also this model, as the previous one, considers gaseous butadiene as the only pyrolisis product of HTPB, in accord with the work of Risha et al. [25]. Reaction scheme is as follows:

$$\begin{aligned} 1) \quad & C_4H_6 + 2O_2 \rightarrow 4CO + 3H_2 \\ 2) \quad & C_4H_6 + 2H_2O \rightarrow 4CO + 7H_2 \\ 3) \quad & CO + H_2O \leftrightarrow CO_2 + H_2 \\ 4) \quad & H_2 + 0.5O_2 \leftrightarrow H_2O \\ 5) \quad & O_2 + M \leftrightarrow O + O + M \\ 6) \quad & H_2O + M \leftrightarrow OH + H + M \end{aligned} \tag{3.59}$$

Again, Arrhenius type reaction constants are used and expressed as in equation (3.58). Chemical kinetics data is reported in table 3.2:

Table 3.2: Chemical reaction scheme, 6 reactions

Reaction	**A** $[\mathbf{m^3/mol \cdot s}]$	**Ea [cal/mol]**	**n**	**Reaction Rate**	**a**	**b**
1)	3.08×10^{08}	-30000	0	$k_1[C_4H_6]^a[O_2]^b$	0.5	1.25
2)	3.79×10^{11}	-30000	0	$k_2[C_4H_6]^a[H_2O]^b$	1.00	1.00
3)	2.75×10^{09}	-20000	0	$k_3[CO]^a[H_2O]^b$	1.00	1.00
4)	7.50×10^{15}	-40000	-1	$k_4[H_2]^a[O_2]^b$	0.25	1.50
5)	1.50×10^{09}	-113000	0	$k_5[O_2]^a$	1.00	–
6)	2.30×10^{22}	-120000	-3	$k_6[H_2O]^a$	1.00	–

3.7.2 Transport Properties

Viscosity

For molecular viscosity of the single species, the interpolations from [66] is used for all the species except for 1,3-butadiene (C_4H_6), which is not available in given reference. It is an interpolation of the form:

$$\ln \mu = A \ln T + \frac{B}{T} + \frac{C}{T^2} + D \tag{3.60}$$

Where coefficients A, B, C and D are given in [66] for 200 - 1000 K and 1000 - 6000 K temperature ranges. For 1,3-butadiene the Chapman-Enskog correlation from [51], with data for C_4H_6 from [67], is used:

$$\mu_i = 26.69 \frac{(MT)^{\frac{1}{2}}}{\sigma^2 \Omega_v} \tag{3.61}$$

Where:

$$\Omega_v = a(T^*)^{-b} + c\exp(-dT^*) + e\exp(-fT^*) \tag{3.62}$$

$$\sigma = 0.809 V_c^{\frac{1}{3}} \tag{3.63}$$

$$T^* = T(\frac{\epsilon_c}{k_b})^{-1} \tag{3.64}$$

where ϵ_c is the characteristic energy and V_c is the critical volume. In addition:

$$\begin{aligned} a &= 1.16145 \qquad d = 0.77320 \\ b &= 0.14874 \qquad e = 2.16178 \\ c &= 0.52487 \qquad f = 2.43787 \end{aligned} \tag{3.65}$$

Results from (3.61) do not consider molecular polarity. Therefore, in order to correct viscosity also considering acentric factor and molecular polarity, the following correlation from [68] is used:

$$\mu_i = 40.785 \frac{F_c (MT)^{\frac{1}{2}}}{V_c^{\frac{2}{3}} \Omega_v} \tag{3.66}$$

C_4H_6 Parameters	
$M[g/mol]$	54.092
$T_c\ [K]$	425.17
$p_c\ [Pa]$	$4.3 \cdot 10^{-6}$
$V_c\ [cm^3/mol]$	220
Z_c	0.268
AF	0.192

Table 3.3: Parameters for 1,3-butadiene viscosity calculations, from [67]

Where correction factor F_c expression depends on the polarity characteristics of butadiene molecule, and has the form:

$$F_c = 1 - 0.2765AF \tag{3.67}$$

Following table 3.3 shows the parameters used for 1,3-butadiene viscosity calculations:

Results of viscosity calculations are presented in the following figure:

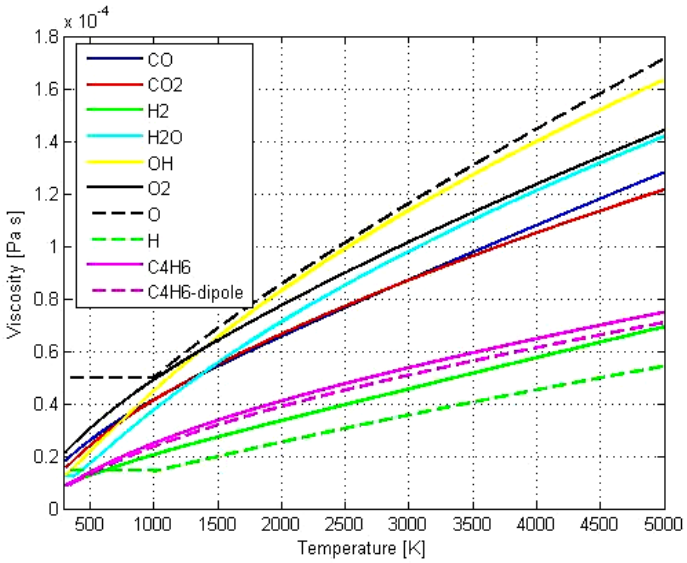

Figure 3.2: Chemical species viscosity as function of temperature

As shown in figure 3.2 available data ranges for H_2O and O are available respectively from 300 K and from 1000 K. Below these values, viscosity was not extrapolated, but considered constant and with value corresponding to the first available data. For molecular viscosity of the mixture μ, the approach from [69] is chosen:

$$\mu = \sum_{i=1}^{NS} \frac{\mu_i}{1 + \frac{1}{\chi_i} \cdot \Sigma_\phi} \tag{3.68}$$

where χ_i is the mole fraction, and:

$$\Sigma_\phi = \sum_{j=1, j\neq i}^{NS} \chi_j \phi_{ij} \tag{3.69}$$

and:

$$\phi_{ij} = \frac{\left[1 + \left(\frac{\mu_i}{\mu_j}\right)^{\frac{1}{2}} \left(\frac{M_i}{M_j}\right)^{\frac{1}{4}}\right]^2}{\frac{4}{\sqrt{2}}\left[1 + \left(\frac{M_i}{M_j}\right)\right]^{\frac{1}{2}}} \tag{3.70}$$

Thermal Conductivity

For thermal conductivity of the species κ_i, the same kind of interpolation as the one previously shown for viscosity from [66] can be used. Coefficients A, B, C and D coefficients are conductivity-specific and are given by the reference. This again does not apply to 1,3-butadiene, which is not available in given reference, as for viscosity. For butadiene, different approaches from [67] are compared: two modified Eucken models (original, Stiel and Thodos [70]) and Chung et al. method [68], both valid for the required temperature range (200 - 6000 K). These results are compared with cubic regression from [71] (valid only between 250 K and 1500 K) and with experimental values from [72] and [73]. Modified Eucken model expresses thermal conductivity as a function of viscosity and specific heat. Viscosity was calculated in the previous section while specific heat is from [75] and will be discussed in the following section. These methods imply ideal gas hypothesis and are expressed as follows:

$$\kappa_i = 1.32\frac{\mu_i c_v}{M} + \frac{1.77}{\frac{c_p}{R} - 1} \tag{3.71}$$

Stiel and Thodos [70] suggested a modification of equation (3.71), as follows:

$$\kappa_i = 1.15\frac{\mu_i c_v}{M} + \frac{2.03}{\frac{c_p}{R} - 1} \tag{3.72}$$

Chung et al. [68] method is expressed as:

$$\kappa_i = \frac{\mu_i c_v}{M} \cdot \frac{3.77\Psi}{\frac{c_v}{R}} \tag{3.73}$$

Ψ is function of three parameters: α, β and Z. Such as:

$$\Psi = 1 + \alpha\left[\frac{(0.215 + 0.28288\alpha - 1.061\beta + 0.26665Z)}{(0.6366 + \beta Z + 1.061\alpha\beta)}\right] \tag{3.74}$$

with:

$$\begin{aligned} \alpha &= \frac{c_v}{R} - \frac{3}{2} \\ \beta &= 0.7682 - 0.7109AF + 1.3168(AF)^2 \\ Z &= 2.0 + 10.5\left(\frac{T}{T_c}\right)^2 \end{aligned} \tag{3.75}$$

Experimental results for thermal conductivity are available only in a narrow range of temperatures 273.15 - 673.15 K and present work requires a more extended range. Consequently to choose a method for C_4H_6 is no trivial task. Figure 3.3 compares results from all the methods, and figure 3.4shows a detail in the range of experimental data.

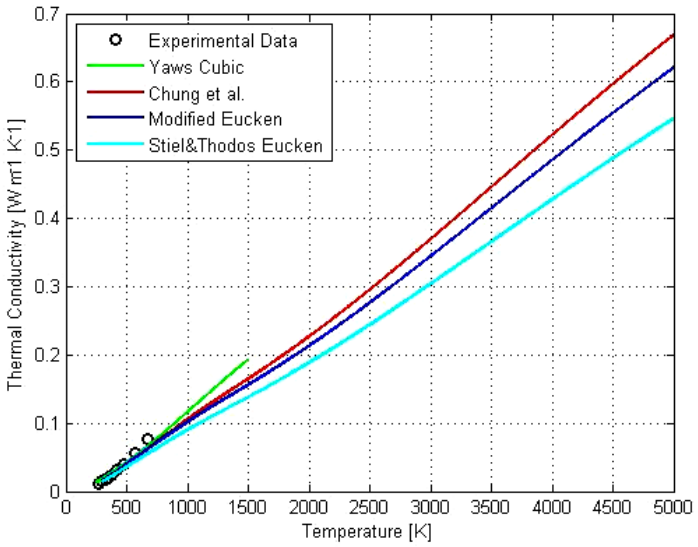

Figure 3.3: Comparison of methods for C4H6 thermal conductivity calculation

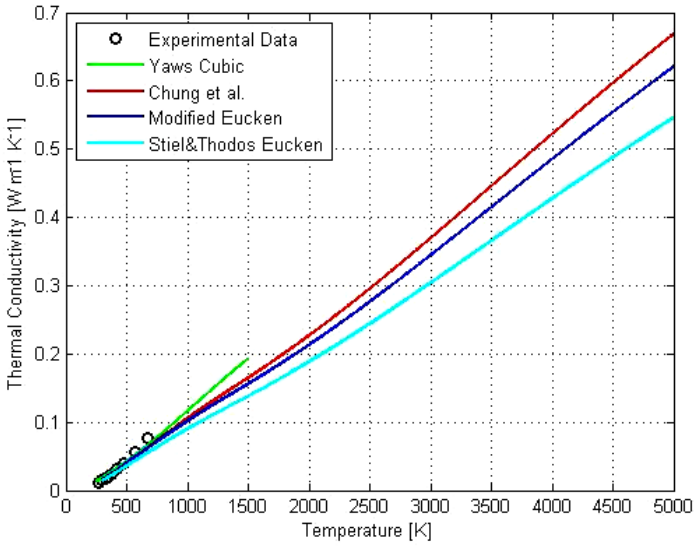

Figure 3.4: Comparison of methods for C4H6 thermal conductivity, detail

Previous figures show that possibly modified Eucken and Chung et al. approaches are the best found for 1,3-butadiene thermal conductivity estimation. Following the more general discussion from [67], Chung et al. method is usually characterised by smaller

error for a wide variety of substances. Consequently this method is chosen. Summarizing, results of species thermal conductivities calculation κ_i is presented in figure 3.5:

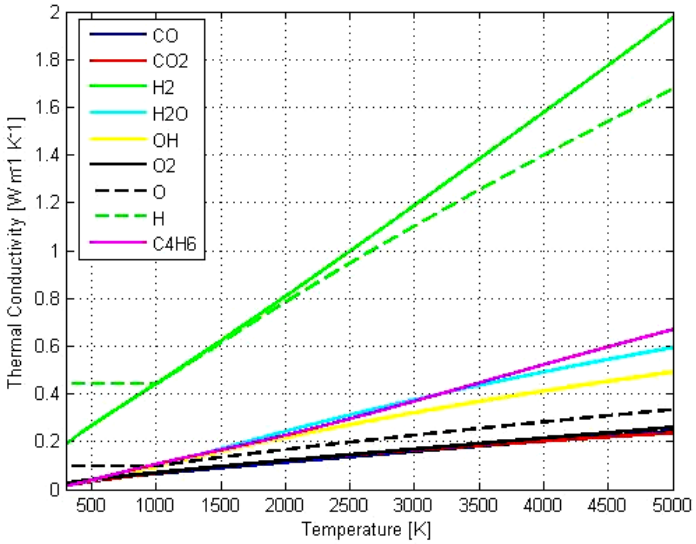

Figure 3.5: Chemical species thermal conductivity as function of temperature

For mixture thermal conductivity κ, the approach for polyatomic gas mixtures from [74] is chosen. This represents an adequate approximation even if monoatomic species are present, such as O and H, as in the six-reaction model used.

$$\kappa = \sum_{i=1}^{NS} \kappa_i \left[1 + \sum_{k=1, k\neq i}^{NS} G_{ik} \frac{\chi_k}{\chi_i} \right]^{-1} \tag{3.76}$$

where:

$$G_{ik} = \frac{1.065}{2\sqrt{2}} \left(1 + \frac{M_i}{M_k} \right)^{-\frac{1}{2}} \left[1 + \left(\frac{\kappa_i^0}{\kappa_k^0} \right)^{\frac{1}{2}} \left(\frac{M_i}{M_k} \right)^{\frac{1}{4}} \right]^2 \tag{3.77}$$

and:

$$\frac{\kappa_i^0}{\kappa_k^0} = \frac{\mu_i}{\mu_k} \frac{M_k}{M_i} \tag{3.78}$$

It is important to indicate that in reference [74], the value of κ is not expressed in SI units, but as $[erg/cm \cdot s \cdot K]$. Therefore the validity of coefficients in (3.77) for other dimensional units is not guaranteed and a careful conversions from and to SI units is to be accounted for.

3.7.3 Thermodynamical Properties

Enthalpy and Specific Heat

Single reacting species static enthalpy $h_{st,k}$ and specific heat (at constant pressure) $c_{p,k}$ is taken from NASA polynomials, as given by [75], who extended the original database

from Gordon and McBride [76]. These data are the same used by NASA CEA and Thermobuild codes, therefore their validity in the given temperature range of 200 – 6000 K is guaranteed by an extensive use since several decades. It is important to notice that the static enthalpy given by the polynomial expression includes the enthalpy of formation, as:

$$h_t = \Delta_f h^0_{298} + \int_{298}^{T} c_p \mathrm{d}T \tag{3.79}$$

The polynomials have the form:

$$\frac{h_t}{RT} = a_1 + \frac{a_2 T}{2} + \frac{a_3 T^2}{3} + \frac{a_4 T^3}{4} + \frac{a_5 T^4}{5} + \frac{a_6}{T} \tag{3.80}$$

and:

$$\frac{c_p}{R} = a_1 + a_2 T + a_3 T^2 + a_4 T^3 + a_5 T^4 \tag{3.81}$$

In order to obtain the mixture total enthalpy, sensible enthalpy and specific heat it is possible to average single values over single species mass fraction Y_i:

$$c_p = \sum_{i=1}^{NS} Y_i c_{p,i} \tag{3.82}$$

$$h_{s,t} = \sum_{i=1}^{NS} Y_i h_{s,t,i} \tag{3.83}$$

3.7.4 Diffusion

As previously seen, in order to close the conservation equation for chemical species mass fraction, it is necessary to model both molecular and turbulent diffusive fluxes. It is possible to obtain this using a gradient hypothesis, which gives, for laminar diffusion:

$$J_j^k = -\frac{\mu}{Sc_k} \frac{\partial Y_k}{\partial x_j} \tag{3.84}$$

The Fick's law approach expressed in (3.84) however is in general non-conservative, and the equation for the sum of diffusion fluxes:

$$\sum_i J_i = 0 \tag{3.85}$$

is not respected. In order to overcome this non-physical behavior, three different strategies are possible:

1. diffusion coefficients for all chemical species are equal (therefore only one diffusion value is computed), under the approximation of constant Lewis number:

$$Le = \frac{Sc}{Pr} = \frac{\mu}{\rho D} \frac{1}{Pr} \tag{3.86}$$

Therefore the only diffusion coefficient is:

$$D = \frac{\mu}{\rho} \frac{1}{Pr} \frac{1}{Le} = \frac{\cancel{\mu}}{\rho} \frac{\kappa}{c_p \cancel{\mu}} \frac{1}{Le} = \frac{\kappa}{\rho c_p} \frac{1}{Le} \tag{3.87}$$

With constant Lewis number e.g. $C = \frac{1}{Le}$, which is a numerical value, it is possible to write:

$$D = C\frac{\kappa}{\rho c_p} \tag{3.88}$$

2. Fick's law modified with Ramshaw [77] self-consistent modification of fluxes, where (3.85) is valid.

$$J_i = -cM_i D_i G_i + \frac{\rho_i c}{\rho}\sum_j M_j D_j G_j \tag{3.89}$$

$c = \sum_{i=1}^{NS} \frac{\rho_i}{M_i}$ represents the total molar concentration of the mixture and where:

$$D_i = (1-\chi_i)\left(\sum_j \frac{\chi_j}{D_{ij}}\right)^{-1} \tag{3.90}$$

where $\chi_i = Y_i\frac{M}{M_i}$ represents the mole fraction of each species, M is the average molar mass of the mixture and:

$$G_i = \nabla\chi_i + (\chi_i - Y_i)\nabla\ln p + D_i^T\nabla\ln T - \frac{1}{p}\left(\rho_i F_i - Y_i\sum_j \rho_j F_j\right) \tag{3.91}$$

D_i^T for multi-component gas mixtures is obtained from [78] and depends on integral functions of transport cross sections and on binary collision angles. It is important to notice that these values where not readily available in literature for the considered gaseous fuel species, 1,3-butadiene.

3. introduction of Stefan-Maxwell equations (from [79]), which express the gradient of mole fractions of species i in j-th direction as function of fluxes of each binary couple, as follows:

$$G_i = \sum_{j=1}^{NS}\frac{c_i c_j}{c^2 D_{ij}}\left(\frac{J_j}{c_j} - \frac{J_i}{c_i}\right) \tag{3.92}$$

This approach, validated in [80], requires numerical iteration, because flux ratio is not known a-priori.

Between the three approaches previously described, the second and the third require the calculation of binary diffusivity for all chemical species, paired with all the possible couples. An extensive research in available literature has been performed, with the most interesting results in [67] and from [81] to [86]. The method discussed by Fuller et al. in [82] is considered the most promising above all others (such as Wilke-Lee [83] and Chapman-Enskog [84]) for simplicity of use and coherence wih esperimental data, as in [85] and [86]. The method itself is charaterised by a semi-empirical equation which is dependant on temperature, pressure, molar masses and diffusion volumes:

$$D_{ij} = \frac{0.0143\cdot T^{1.75}}{pM_{ij}^{\frac{1}{2}}\left[(\Sigma_v)_i^{\frac{1}{3}} + (\Sigma_v)_j^{\frac{1}{3}}\right]^2} \tag{3.93}$$

Σ_v, diffusion volume	
CO	18.00
CO_2	26.90
C_4H_6	77.46
H	2.31
H_2	6.12
H_2O	13.10
O	6.11
O_2	16.30
OH	8.42

Table 3.4: Molecular diffusion volumes of considered species

where:

$$M_{ij} = 2\left[\left(\frac{1}{M_i}\right) + \frac{1}{M_j}\right]^{-1} \tag{3.94}$$

It is important to notice that p and T are the mixture pressure expressed in atmospheres and temperature expressed in K. Σ_v is the sum of atomic and structural volume of the species. Table 3.4 shows the calculated Σ_v values for the nine chemical species considered for present work:

Even if this approach is able to give the binary diffusion for couples concerning also butadiene gas, it is important to notice that it is based on an semi-empirical relation which is affected by a certain degree of approximation. In conclusion, it was necessary to choose one of the described approaches for diffusion. In order to maintain the best compromise between implementation simplicity and model accuracy, diffusivity is modeled as the same value for all chemical species. Even if this is the most simple approach, keeping a common value for diffusivity does not represent a violation of mass conservation. Therefore the possibilities described in the present section can be used for further developments of this work.

Chapter 4

COOLFluiD Code

The system of equations previously introduced is implemented in the COOLFluiD object-oriented scientific computing environment, developed at von Karman Institute for Fluid Dynamics, see [87], [88] and [89]. Present chapter aims to describe three topics:

- general description of COOLFluiD code and its features;
- description of the numerical methods used for the numerical modeling and computation of combustion processes in HRE within the COOLFluiD environment;
- description of the combustion model library - the library which implements all the required properties (chemistry, thermodynamics, transport) for the aforementioned closure of the governing equations.

4.1 General Features

COOLFluiD code was created as a maintainable and updatable platform to solve multiple physical problems with specific computing algorithms. In order to achieve this goal, the code has a multi-layered structure:

- *the kernel* is where data structures, abstract interfaces and basic functionaliyies are supplied;
- *the plug-in modules* are used to describe physical models and numerical methods.
- *the application*, which selects the libraries needed for a specific physical simulation.

This is better described by figure 4.1, where it is possible to recognize the layered structure with the distinction between the kernel, the problem physics / the numerics and the application. In fact from top to bottom it is possible to say that the abstract interfaces and data structres of the code become concrete, with the actual implementation.

In order to achieve the possibility for the code to evolve in time, with the addition of new features (both physical models and numerical schemes), a component *plug-in* philosophy is enforced. Each capability is encapsulated in a separate component which is

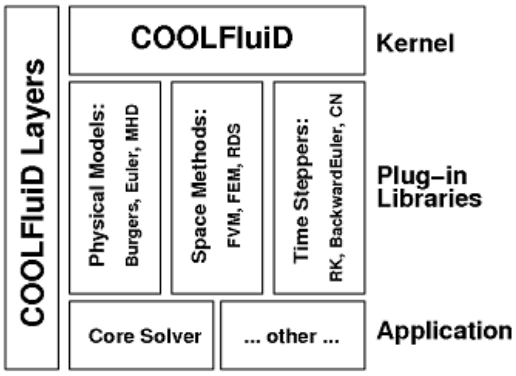

Figure 4.1: COOLFluiD code structure

connected to the others at run-time on a need-to basis. This strategy allows the realization of application-based solvers from an extensible base of components. Figure 4.2 shows this plug-in architecture, where external plug-in capability is shown. Therefore, in

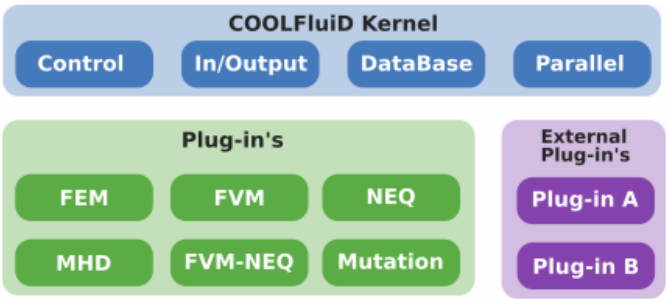

Figure 4.2: COOLFluiD plug-in architecture

order to actually realize a multi-physics computing environment able to apply efficiently arbitrary numerical algorithms, three ideal structures are needed:

- the discretization data, which is related to the mesh structure geometry and solution on computational domain;
- the set of governing equations of the physical problem;
- the set of numerical algorithms used to solve the PDE system.

The COOLFluiD code is realized in order to be able to implement the numerical methods, the physical models and the mesh data independently. For a detailed description of this, see the works of Lani see [87], Quintino [88] and Wuilbaut [89]. In conclusion, COOLFluiD is an MPI parallel code, constituted by a kernel plus dynamic plugins structure which solves multiple physical models (on 2D and 3D meshes) and offers multiple discretization techniques (finite differences, finite elements and finite volumes). In order to solve the multi-species, turbulent reacting flow for the modeling of HRE a specific mix

of modules where chosen if present or realized ad-hoc during this thesis work. A space second order cell-centered finite volume method for the solution of Navier-Stokes system of equations, with Liou [90] AUSM+-Up flux-splitting upwinding technique for convective terms was used. Diffusive fluxes, which are also dependant on variable gradients, are calculated by nodal extrapolation on a diamond-shaped volume, as described in [87]. Source terms are discretized in the same fashion as diffusive fluxes, but using cell center values and cell volume (this instead of diamond-shaped volumes). The linear system is solved using PETSc [91] libraries with Generalized Minimum Residual (GMRES) technique. In the following section a more detailed discussion of finite volume method will be introduced together with a more complete description of the discretization of convective flux, diffusive flux and source term.

4.2 Numerics

4.2.1 Cell-Centered Finite Volume Method

Finite Volume method is nowadays a standard technique for the simulation of flows in a wide range of conditions [92], [93], [94]. These methods are based on the integral form of conservation laws instead of the differential equation. The domain is divided into finite grid cells, the *volumes*, and the solution is approximated as a cell-averaged value (the integral divided by the volume of the cell). In the case of cell-centered finite volumes, the average is taken at the cell center. At each time step these integrals are modified by the fluxes at the cell edges: therefore the problem is to choose functions for the numerical fluxes which are able to approximate well the actual physical fluxes. Finite volume methods overcome the problem present in finite difference methods, where derivatives are approximated by finite differences: in the presence of discontinuities, the differential equation does not hold anymore and the physical solution is not captured. In general, a set of governing equations can be expressed in a general conservative form as:

$$\frac{\partial \boldsymbol{U}}{\partial t} + \frac{\boldsymbol{F_i^c}}{\partial x_i} = \frac{\partial \boldsymbol{F_i^d}}{\partial x_i} + \boldsymbol{S} \tag{4.1}$$

where $\boldsymbol{U}$ are the conservative variables, $\boldsymbol{F}^c$ are the convective fluxes, $\boldsymbol{F}^d$ are the diffusive fluxes and $\boldsymbol{S}$ represents the source term. Finite volume method discretizes the PDE system expressed in equation (4.1) in an integral form:

$$\frac{d}{dt}\int_\Omega \boldsymbol{U}\mathrm{d}\Omega + \oint_\Sigma \boldsymbol{F}^c \cdot \boldsymbol{n}\mathrm{d}\Sigma \;=\; \oint_\Sigma \boldsymbol{F}^d \cdot \boldsymbol{n}\mathrm{d}\Sigma + \int_\Omega \boldsymbol{S}\mathrm{d}\Omega \tag{4.2}$$

where Gauss theorem was applied in order to convert the volume integrals in contour integrals for convective and diffusive fluxes and Ω represents the volume of the computational cells. The solution is assumed piecewise constant on a cell basis and stored in the cell centroid. This cell average corresponds to a discontinuity at cell interfaces. The

numerical fluxes, used to approximate the physical fluxes at cell interfaces, must satisfy the following properties:

- *flux conservation* - the flux resulting from adjacent control volumes sharing an interface must be equal in modulus and opposite in sign (exact elimination under summation);
- *consistency* - the numerical flux evaluated for identical arguments must be equal to the physical flux.

It is also important to notice that the solution is available only at the computational nodes, in this case the cell centers. In order to obtain the solution at cell vertices, an adequate interpolation is needed. Figure 4.3 depicts the cell-centered finite-volume discretizations. It

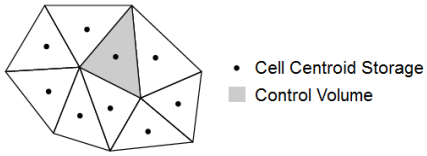

Figure 4.3: Cell-centered finite volume discretization

is possible to understand that the discretization of equation (4.2) terms can be performed separately. In partucular, for combustion modeling an AUSM upwind method is applied to convective fluxes and central discretizations are applied to diffusive flux and source term. The strategies present in the COOLFluiD code and used for the HRE combustion modeling are described in the following sections.

4.2.2 Fluxes and Source Term Discretization

Convective Fluxes

From the discretization of convective flux term in equation (4.2), the following equation is obtained:

$$\oint_{\Sigma} \boldsymbol{F}^c \cdot \boldsymbol{n} \mathrm{d}\Sigma = \sum_{f=1}^{Nf} \boldsymbol{F}_f \Sigma_f \tag{4.3}$$

where subscript f indicates the f-th interface of area Σ_f. $\boldsymbol{F}_f$ is the convective numerical flux projected in direction normal to the interface. The numerical flux $\boldsymbol{F}$ depends on the state vectors corresponding to left and right neighboring cells: this originates non-linear Riemann problems at the interfaces, which can be treated as described by [95]. Methods for the solution of this problem should be able to capture accurately the discontinuities which might arise from compressible conditions. In addition the entropy condition must be respected: expansion shocks are not admissible weak solutis of equation (4.2). Several techniques are possible such as: Flux Vector Splitting (FVS), Flux Difference Splitting (FDS) or an hybrid of both the previous. The choice for multi-species, turbulent, reacting flow is the flux splitting AUSM family which is described in the next section.

AUSM Family

Liou and Steffen [96], [97], [96], [90] tried to conjugate the robustness of Godunov schemes with the efficiency of FVS methods. This originated the Advection Upstream Splitting Method - AUSM. The main idea of AUSM methods is the splitting of the numerical flux into two parts. The first represents a convective term and the second a pressure term, such as:

$$\boldsymbol{F}(\boldsymbol{U}) = \boldsymbol{F}^{(c)} + \boldsymbol{F}^{(p)} \tag{4.4}$$

The discretization of the numerical flux at the interface depends on the left and right state vectors $\boldsymbol{U}_L$ and $\boldsymbol{U}_R$, becoming:

$$\boldsymbol{F}_{1/2}(\boldsymbol{U}_L, \boldsymbol{U}_R, \boldsymbol{n}) = \dot{m}_{1/2}(\boldsymbol{U}_L, \boldsymbol{U}_R, \boldsymbol{n})\boldsymbol{\Psi}_{L/R} + \boldsymbol{p}_{1/2}(\boldsymbol{U}_L, \boldsymbol{U}_R, \boldsymbol{n}) \tag{4.5}$$

Defining $q_n = \boldsymbol{u} \cdot \boldsymbol{n}$, which is the velocity projected on the direction normal to the cell interface, the convective flux is constituted by a common scalar mass flux term $\dot{m} = \rho q_n$ that takes into account the flow direction (therefore the upwinding nature of AUSM) and by a vector quantity $\boldsymbol{\Psi}$ which represents the problem variables (e.g. mass fractions, velocities, enthalpy) convected by the mass flux. Consequently, the pressure flux contains only the pressure term. Different choices for $\dot{m}_{1/2}$ and $\boldsymbol{p}_{1/2}$ originate the different AUSM family schemes. In particular, the latest AUSM+-Up is chosen for the present work and therefore it is briefly described below.

AUSM+-Up

The mass flux scalar term $\dot{m}_{1/2}$ is described as a function of interface Mach number $M_{1/2}$, and left/right neighboring cells densities ρ_L, ρ_R and interface sound speed $a_{1/2}$:

$$\dot{m}_{1/2} = M_{1/2} a_{1/2} \begin{cases} \rho_L & \text{if } M_{1/2} > 1 \\ \rho_R & \text{otherwise} \end{cases} \tag{4.6}$$

where $M_{1/2}$ is a polynomial function of left and right neighboring cell Mach numbers $\mathcal{M}_L$ and $\mathcal{M}_R$. The basic AUSM method uses:

$$M_{1/2}^{AUSM} = \mathcal{M}^+(M_L) + \mathcal{M}^-(M_R) \tag{4.7}$$

while AUSM+-Up adds a pressure diffusion term in equation (4.7):

$$M_{1/2} = M_{1/2}^{AUSM} + K_p \max(1 - \sigma \bar{M}^2, 0) \frac{p_R - p_L}{\rho_{1/2} a_{1/2}^2} \tag{4.8}$$

where $0 \leq K_p \leq 1$ and $\sigma \leq 1$. Interface density is:

$$\rho_{1/2} = \frac{\rho_L + \rho_R}{2} \tag{4.9}$$

while average Mach number is:

$$\bar{M} = \frac{q_{nL}^2 + q_{nR}^2}{2a_{1/2}^2} \tag{4.10}$$

Interface sound speed $a_{1/2} = a(\boldsymbol{U}_L, \boldsymbol{U}_R)$ can be expressed in different ways:

$$a_{1/2} = \sqrt{a_L a_R} \tag{4.11}$$

$$a_{1/2} = \frac{a_L + a_R}{2} \tag{4.12}$$

$$a_{1/2} = \min(\bar{a}_L, \bar{a}_R), \quad \bar{a} = \frac{a^{*2}}{\max a^*, |q_n|} \tag{4.13}$$

where the critical sound speed a^* can be defined in several ways, such as:

$$a^* = \sqrt{\frac{2(\gamma-1)}{\gamma+1} H} \tag{4.14}$$

In this work, interface sound speed according to equation (4.12) is used. The same idea about the use of polynomial functions as in equation (4.7) is applied to pressure term. For the standard AUSM method, this gives:

$$\boldsymbol{p}_{1/2} = \mathcal{P}^+(M_L) p_L \boldsymbol{n} + \mathcal{P}^-(M_R) p_R \boldsymbol{n} \tag{4.15}$$

AUSM+-Up modifies the pressure flux given by equation (4.15) as:

$$\boldsymbol{p}_{1/2} = \boldsymbol{p}_{1/2}^{AUSM} - K_u \mathcal{P}^+ \mathcal{P}^- (\rho_L - \rho_R)({}_a a_{1/2})(q_{nR} - q_{nL}) \tag{4.16}$$

where $0 \leq K_u \leq 1$. f_a is the so-called scaling factor:

$$f_a(M_0) = M_0(2 - M_0), \quad M_0^2 = \min(1, \max(\bar{M}^2, M_{co})) \tag{4.17}$$

M_{co} is the cut-off Mach number, which is user defined and has the same order of magnitude as M_∞. The split Mach number and pressure polynomials are the same for AUSM+ and AUSM+-Up methods. They are respectively:

$$\mathcal{M}^{\pm}(M) = \begin{cases} \frac{1}{2}(M \pm |M|), & \text{if } |M| \geq 1, \\ \pm\frac{1}{4}(M \pm 1)^2 (1 \mp 16\beta \frac{1}{4}(M \pm 1)^2), & \text{otherwise} \end{cases} \tag{4.18}$$

$$\mathcal{P}^{\pm}(M) = \begin{cases} \frac{1}{M}\frac{1}{2}(M \pm |M|), & \text{if } |M| \geq 1, \\ \pm\frac{1}{4}(M \pm 1)^2 \left[(\pm 2 - M) \mp 16\alpha M \mp \frac{1}{4}(M \mp 1)^2\right], & \text{otherwise} \end{cases} \tag{4.19}$$

Parameters α, β and σ in AUSM+-Up are:

$$\alpha = \frac{3}{16}\left(-4 + 5f_a^2\right) \in \left[-\frac{3}{4}, \frac{3}{16}\right], \quad \beta = \frac{1}{8}, \quad \sigma = 1 \tag{4.20}$$

Liou [90] suggests standard values for $K_p = 0.25$ and $K_u = 0.75$.

Diffusive Fluxes

Diffusive flux term can be discretized as follows:

$$\oint_{\Sigma} \boldsymbol{F}^d \cdot n \mathrm{d}\Sigma = \sum_{f=1}^{Nf} \boldsymbol{G}_f \Sigma_f \tag{4.21}$$

$\boldsymbol{G}_f$ is the diffusive numerical flux projected in direction normal to the interface. Diffusive fluxes are usually a function of primitive variables and their gradients $\boldsymbol{F}^d = \boldsymbol{F}^d(\boldsymbol{P}, \nabla \boldsymbol{P})$. These gradients must be determined in order to find diffusive numerical flux. In order to do this, a control volume Ω_v has to be chosen. As in [99], a good choice is a double-tetrahedral structure, forming a diamond shape. These two tetrahedra have a common base which is determined by the interface nodes. Left and right neighboring cell centroids are the vertex of the two tetrahedra. Figure 4.4 shows the diamond-shaped control volume: It is possible to apply Gauss theorem to determine these gradients:

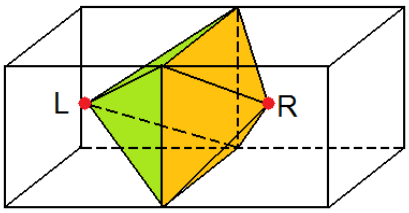

Figure 4.4: Double tetrahedra (or diamond) shaped control volume

$$\nabla \boldsymbol{P} = \frac{1}{\Omega_v} \int_{\Omega_v} \nabla \boldsymbol{P}' \mathrm{d}\Omega_v = \frac{1}{\Omega_v} \oint_{\Sigma_v} \boldsymbol{P} \cdot \boldsymbol{n} \mathrm{d}\Sigma_v \tag{4.22}$$

Equation (4.22) is then discretized using face-averaged values $\bar{\boldsymbol{P}}_f$ which are calculated from the values $\boldsymbol{P}_j^f$ in the vertices of diamond volume:

$$\nabla \boldsymbol{P} = \frac{1}{\Omega_v} \sum_{f=1}^{Nf} \bar{\boldsymbol{P}}_f \boldsymbol{n}_f \Sigma_{vf} \tag{4.23}$$

and:

$$\bar{\boldsymbol{P}}_f = \frac{1}{N_v^f} \sum_{j=1}^{N_v^f} \boldsymbol{P}_j^f \tag{4.24}$$

Nf represents the number of faces, N_v^f represents the number of vertices of each face of the diamond and it is therefore equal to the problem dimensions (2 for 2D and 3 for 3D). It is important to notice that $\boldsymbol{P}_j^f$ can contain cell centered values as well as vertex values. Because a cell-centered finite volume method is used, solution is computed at cell centers:

therefore a weighted extrapolation is in order to obtain vertex values. Vertex values $\boldsymbol{P}_v$ are defined as weighted sum of the values at the cell centers which surround the vertex:

$$\boldsymbol{P}_v = \frac{\sum_c \boldsymbol{P}_c \omega_c}{\sum_c \omega_c} \tag{4.25}$$

Several weighing techniques are possible and implemented in COOLFluiD, but the preferred one for its robustness is based on the inverse of the distance between vertex and center, giving:

$$\omega_c = \frac{1}{\|\boldsymbol{\Delta} x_c\|} \tag{4.26}$$

with $\boldsymbol{\Delta} x_c = x_c - x_v$.

Source Term

Source term are discretized using the i-th cell-centered value:

$$\int_\Omega \boldsymbol{S}(\boldsymbol{P}) \mathrm{d}\Omega \approx S(P_i)\Omega_i = \boldsymbol{S}_i \Omega_i \tag{4.27}$$

If the source term is dependant also on some derivatives, the Gauss-Green theorem is applied in analogy to equation (4.22). The chosen control volume in this case is not diamond-shaped, but it is the volume of the current cell. The discretization of source terms is then the same represented in equation (4.23).

4.3 Combustion Library for HRE Simulation

This sections describes in detail the structure of the library implemented for the modeling of combustion processes in HRE. Two libraries were created:

- *CombustionModelLibrary*, is the first approach, hard-coded version of the combustion module implemented in COOLFluiD framework;
- *CombustionModelLibrary2*, is the generic version of the combustion module.

The aerothermodynamics module ATDModelLibrary, designed for the simulation of hypersonic reacting flows, was used as reference module for inheritance. In fact as a first step, CombustionModelLibrary was created in order to achieve in the shortest time as possible the capability of testing and validating thermodynamic and transport property models. But of more importance, to enable the validation of chemical closure models. Hard-coded version however has a major drawback: it allows only the use of the three pre-determined chemical models. These are suitable for the simulation and analysis of traditional HRE fuel combustion, but it is important to give the code the capability to evolve with the developement of innovative fuel formulations. In order to overcome this problem and allow the combustion model to perform the calculations for virtually any oxidizer/fuel couple, a generic library is also implemented. The two libraries are described in detail in the next sections.

4.3.1 Combustion Model Library - Hard Coded

Mixtures and Species

First step in order to implement the previously described combustion model physics and parameters, is to define and prepare different folders, files and in-code IDs for the three different chemical models to be compared. Figure 4.5 shows this in detail. It is no-

	Chemical Model		
	Venkateswaran	Jones-Lindstedt 4	Jones-Lindstedt 6
_chemID	0	1	2
Chem Names for .CFCase File	venka2r	jones4r	jones6r
Number of Reactions	2	4	6
Mixture Files	/mixtures/comb/ Venka5s.cmix	/mixtures/comb/ Jones6s.cmix	/mixtures/comb/ Jones9s.cmix
Mixtue Names for .CFCase File	venka5s	jones6s	jones9s
Number of Species	5	6	9
Species Files	/species/venka/*.cspc	/species/jones4/*.cspc	/species/jones6/*.cspc

Figure 4.5: Mixture and species file description

ticeable that, with respect to the description present in chapter 3, an additional chemical model is added (Jones-Lindstedt 4) for testing purposes. This model is the same as Jones-Lindstedt six reaction model, but the last two chemical equation (dissociation of O_2 and of H_2O) are not present. Each *.cmix file contains the number of species for the corresponding model and a list of species. It is important to specify that C_4H_6, H_2O, O and H use specific models for certain properties, as described before, and therefore the order of species listed in *.cmix files is important, because a dependency on code cycles implementation exists, and it is based on array position triggers. Table 4.1 lists this specific order with explicit reference to referring chemical model: Each *.cspc file contains molar mass, formation enthalpy, and all the coefficients needed for the run-time calculation of species viscosity (eight in total, four per temperature range) and thermal conductivity (eight in total, four per temperature range, as for viscosity). As a default, Venkateswaran chemical model is used. Through .CFCase configuration file it is possible to override the default behevior and use all chemical models: chemical names and mixture names are to be considered as coupled and correspondence has to be applied in .CFCase file.

Species Order by Chemical Model		
Venkateswaran 2	Jones-Lindstedt 4	Jones-Lindstedt 6
C_4H_6	C_4H_6	C_4H_6
H_2O	H_2O	H_2O
O_2	O_2	H
CO	H_2	O
CO_2	CO	CO
-	CO_2	CO_2
-	-	OH
-	-	O_2
-	-	H_2

Table 4.1: Species order by chemical model

Specific Heat and Enthalpy Interpolation Coefficients			
$< 1000K$	$\geq 1000K$ 2	$< 1000K$	$\geq 1000K$
_a1cp1[_NS]	_a1cp2[_NS]	_a1h1[_NS]	_a1h2[_NS]
_a2cp1[_NS]	_a2cp2[_NS]	_a2h1[_NS]	_a2h2[_NS]
_a3cp1[_NS]	_a3cp2[_NS]	_a3h1[_NS]	_a3h2[_NS]
_a4cp1[_NS]	_a4cp2[_NS]	_a4h1[_NS]	_a4h2[_NS]
_a5cp1[_NS]	_a5cp2[_NS]	_a5h1[_NS]	_a5h2[_NS]
-	-	_a6h1[_NS]	_a6h2[_NS]

Table 4.2: Arrays for the interpolation of thermodynamic properties

Thermodynamic Properties

In order to maintain the structure of parent ATDModelLibrary module, specific heat and enthalpy for each species are calculated through implementation of polynomials, as in chapter 3. Polynomial coefficients are passed through a reading-from-file code instruction, stored in a corresponding array and then properties calculation is performed. One *.cthm for each chemical species is present, and the possibility to introduce further models for thermal properties is maintained through a switch based on _thermoID parameter. Currently for polynomial interpolation _thermoID is set as 0. Function **CpPoly()** is used to interpolate specific heat for each species with current run-time temperature value and it also calculates mixture specific heat as in equation (3.82). Function **EnthPoly()** computes species enthalpy given current temperature. Table 4.2 shows the variables introduced for thermodynamic properties interpolation. Each variable is represented by an array of length equal to the number of species _NS.

Viscosity and Thermal Conductivity Interpolation Coefficients			
$< 1000K$	$\geq 1000K$	$< 1000K$	$\geq 1000K$
_AsMu1[_NS]	_AsMu2[_NS]	_AsK1[_NS]	_AsK2[_NS]
_BsMu1[_NS]	_BsMu2[_NS]	_BsK1[_NS]	_BsK2[_NS]
_CsMu1[_NS]	_CsMu2[_NS]	_CsK1[_NS]	_CsK2[_NS]
_DsMu1[_NS]	_DsMu2[_NS]	_DsK1[_NS]	_DsK2[_NS]

Table 4.3: Arrays for the interpolation of transport properties

Transport Properties

Second step is to design specific functions for the calculation of transport properties for each species as well as for the complete mixture. Viscosity is calculated from eight interpolation coefficients, with function **eta()**: a switch exchanges between the three chemical models previously described in order to use the correct number of chemical species. Position $[0]$ of viscosity vector is reserved for C_4H_6. Position $[1]$ is always reserved for H_2O while positions $[2]$, $[3]$ are reserved for H and O respectively, but only in the Jones-Lindsted nine-species model. A weight function PHIs is then calculated and used to compute mixture viscosity. **LambdaNEQ()** function is used to calculate thermal conductivity of the mixture. The same calculation as in **eta()** function is performed because thermal conductivity is weighted over PHIs function of viscosity. For both viscosity and thermal conductivity the chosen method for C_4H_6 calculation is separately implemented and the value stored in the $[0]$ position of temporary viscosity and thermal conductivity arrays, which are shown in table 4.3: Mass diffusion coefficient D is implemented as described in chapter 3. This is achieved through **getRhoUdiff()** function. This function then calculates the product between density and mass diffusion for the use in governing equations.

Chemical Species Source Term

Source term from chemical reaction is calculated with **getMassProductionTerm()** function. Three-case switch is implemented in order to use each one of the three chemical models previously described, which correspond as before to 0, 1 and 2 values for _chemID parameter. Temporary array with length depending on number of chemical species, is used. For each chemical case, it is important to remember, as for transport properties, that the order from *.cmix files is important. This function then provides an array containing the chemistry source term for each chemical species.

4.3.2 Combustion Model Library - Generic

Generic combustion model library *CombustionModelLibrary2*, as previously indicated, is a modification of the hard-coded combustion model library implemented in order to obtain flexibility in the use of several user-defined chemical models and thermody-

namic/transport properties models. This is performed applying specific strategies:

- as a pre-processing phase, data tables for thermodynamic/transport properties are generated as text files using literature polynomial data with user-defined ΔT;
- chemical data are generated in terms of Arrhenius parameters (pre-exponential, activation energy, temperature and concentration exponents) and stoichiometric coefficients (with sign, where reactants are negative);
- suitable data structures are declared in the combustion library and allocated/filled during setup phase with required data;
- spline interpolation coefficients are generated during setup phase

In this way all required data are generated only once in setup phase, using one *.cmix file is used to describe the chemical mixture. All the previously described functions for the run-time calculations are re-written in order to call a generic spline interpolation function for each of the required properties.

Chapter 5

The Addressed Problem

5.1 Geometry

In this work, it has been chosen to represent the combustion chamber of the hybrid rocket as a 2D computational domain, with an axial inlet for the oxidizer and a transverse inlet for fuel. This geometry is coherent with the inner combustion liner from SPLab facilities at Politecnico di Milano [100]. A good compromise between accuracy, boundary layer resolution and computational time is granted by an 8000 cell mesh, with 80 cells in height and 100 cells in width. The domain is 6 mm high and 250 mm long: in order to reduce computational cost, reacting calculations are performe on half-mesh geometry, therefore 125 mm long. Two different meshes were realized, each one maintaining the same cell number:

- first studies (non-reacting case, laminar combustion case) were performed with a double-sided tapered mesh;
- following studies (turbulent combustion cases) were performed with a uniform mesh.

This choice is the result of specific results analysis that showed how the uniform mesh variant performed well both in the resolution of wall boundary layer (wall cells) and in the resolution of the mid-channel flame front. In fact uniform cell mesh are small enough to maintain a good resolution in the whole channel height, while tapered mesh showed a clipping effect in the mid-channel flame front area. Figure 5.1 shows the meshed test geometry. In order to improve mesh visibility, y axis was properly stretched. Oxidizer inlet extends for the full height of the domain, on the left side. Fuel inlet ranges from 25 to 75 mm in the x direction, corresponding to a 50 mm long fuel grain. Full extension of the domain right side constitutes combustion outlet.

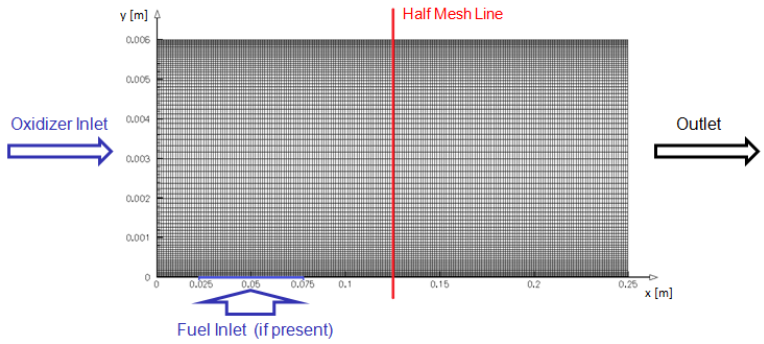

Figure 5.1: First test geometry, tapered mesh

Figure 5.2 shows the uniform meshed geometry, 125 mm long and stretched in y-direction for better mesh visibility:

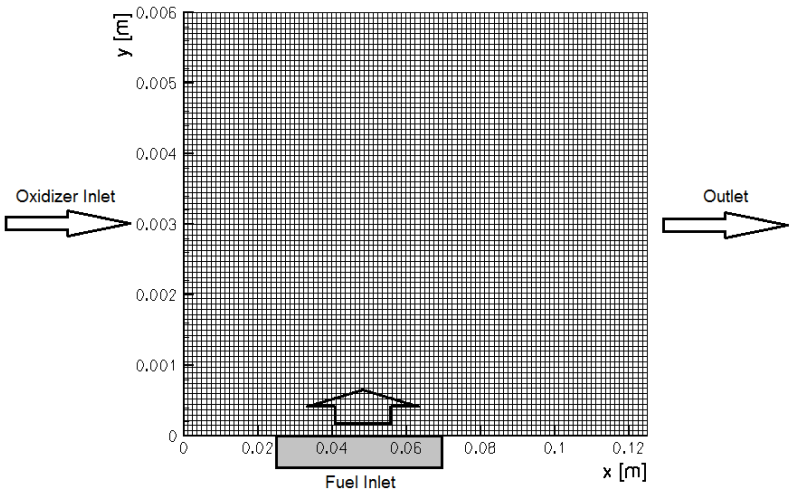

Figure 5.2: Second test geometry, uniform mesh

The double tapered mesh, with ratio 1.1, was used for initial testing in non-reacting condition and first tests in laminar reacting conditions with simplified chemical model. This mesh proved unsuitable in resolving the flame region, with, as said, a *clipping* effect noticeable in the post-processing software. This effect lead to an inadequate matching of physical quantities at the interface between adjacent cells, even if solution convergence was anyhow achieved. The non-tapered mesh proved suitable in both the resolution of the wall boundary layer and the flame region, therefore was applied throughout this study.

5.2 Initial and Boundary Conditions

Boundary conditions are summarized in table 5.1, with turbulence considered to be fully developed at the combustor inlets. Physical walls are reproduced by isothermal no-slip walls. As first approach, fuel inlet speed is constant and based on an experimental law of the type $r_b = aG_{Ox}^n$ ($a = 0.093$, $n = 0.50$) developed by SPLab [103]. Therefore fuel inlet speed is dependant on oxidizer mass flux, and then on oxidizer inlet speed: fuel is injected at HTPB pyrolisis temperature of 800 K. A more accurate version of fuel boundary condition, with the capability of fuel regression rate estimation and a fuel surface temperature which is calculated and not imposed, will be discussed in detail in the next sections. Both boundary conditions required specific implementation inside COOLFluiD code, because turbulent/multi-species reacting inlets were not present. Flow field initial conditions for the base testcase are summarized in table 5.2.

Table 5.1: Boundary conditions

Boundary	**u [m/s]**	**v [m/s]**	**T [K]**	**k** $[\mathbf{m^2/s^2}]$	$\boldsymbol{\omega}[\mathbf{s^{-1}}]$	**p [Pa]**
Oxidizer Inlet	6	0	300	1×10^{-4}	1.11×10^8	-
Fuel Inlet	0	0.26	800	1×10^{-4}	1.11×10^8	-
Upper Wall	0	0	300	0	wall law[a]	-
Lower Wall - Pre-Inlet	0	0	300	0	wall law[a]	-
Lower Wall - Post-Inlet	0	0	600	0	wall law[a]	-
Outlet	-	-	-	-	-	101325

[a] Wall law from Menter $k - \omega$ model [101]

Table 5.2: Initial conditions

Species	**u [m/s]**	**v [m/s]**	**T [K]**	**k** $[\mathbf{m^2/s^2}]$	$\boldsymbol{\omega}[\mathbf{s^{-1}}]$	**p [Pa]**
O_2	6	0	300	1×10^{-4}	1.11×10^8	-

It is important to underline that these are the base testcase boundary conditions. When parametric studies will be discussed in next chapters (e.g. oxidizer inlet speed increase), variations in boundary conditions will be described accordingly.

5.3 Interface Boundary Condition

Numerical modeling of turbulent reacting flows inside hybrid rocket combustion chambers requires specific and careful analysis of boundary conditions at the interface between the different phases of fuel and oxydizer. This chapter aims to discuss mathematical models that can be applied in order to obtain correct boundary treatment when regression rate is not estimated a-priori but it is required as a problem unknown. In order to introduce the problem, governing equations are recalled and converted from differential to integral form, as in [51]. Then a two-phase approach is applied, as in [102] in order

to obtain the final expression for the interface boundary condition, ready to be implemented.

5.4 Derivation of Boundary Condition

The continuity equation in vector form can be expressed as:

$$\frac{\partial \rho}{\partial t} + \nabla \cdot (\rho \boldsymbol{v}) = 0 \tag{5.1}$$

This equation can be integrated over a control volume:

$$\iiint_V \left[\frac{\partial \rho}{\partial t} + \nabla \cdot (\rho \boldsymbol{v}) \right] \mathrm{d}V = 0 \tag{5.2}$$

Using Reynolds' Transport Theorem and the divergence theorem, the integral becomes:

$$\frac{d}{dt} \left(\iiint_V \rho \mathrm{d}V \right) + \iint_S \rho \left(\boldsymbol{v} - \boldsymbol{v}_I \right) \cdot \boldsymbol{n} \mathrm{d}S = 0 \tag{5.3}$$

Where the first term represents the contribution due to integrand change over time and the second term represents the term due to the motion of the control surface S (which bounds the control volume V). The symbol $\boldsymbol{n}$ represents the normal in outward direction from the surface and $\boldsymbol{v_I}$ represents the velocity of the interface. The momentum equation can be expressed in vector form as:

$$\frac{\partial}{\partial t} (\rho \boldsymbol{v}) + \nabla \cdot (\rho \boldsymbol{v} \boldsymbol{v}) = \nabla \cdot \tilde{\boldsymbol{\sigma}} + \rho \sum_{i=1}^{NS} Y_i \boldsymbol{f}_i \tag{5.4}$$

where $\tilde{\boldsymbol{\sigma}} = \sigma_{ij} = \tau_{ij} - p\delta_{ij}$ is the total stress tensor. This equation can be integrated, giving:

$$\frac{d}{dt} \iiint_V \rho \boldsymbol{v} \mathrm{d}V + \iint_S \rho \boldsymbol{v} [(\boldsymbol{v} - \boldsymbol{v}_I) \cdot \boldsymbol{n}] \mathrm{d}S = \iint_S \tilde{\sigma} \cdot \boldsymbol{n} \mathrm{d}S + \iiint_V \rho \sum_{i=1}^{NS} Y_i \boldsymbol{f}_i \mathrm{d}V \tag{5.5}$$

The vector form of the chemical species conservation equation is:

$$\frac{\partial}{\partial t} (\rho Y_i) + \nabla \cdot [\rho Y_i (\boldsymbol{v} - \boldsymbol{V}_i)] = \dot{\omega}_i \tag{5.6}$$

Integrating equation (5.6), gives:

$$\frac{d}{dt} \left(\iiint_V \rho Y_i \mathrm{d}V \right) + \iint_S \rho Y_i (\boldsymbol{v} + \boldsymbol{V}_i - \boldsymbol{v}_I) \cdot \boldsymbol{n} \mathrm{d}S = \iiint_V \dot{\omega}_i \mathrm{d}V \tag{5.7}$$

Starting from complete energy conservation equation expressed in terms of total energy e_t:

$$\frac{\partial}{\partial t} (\rho e_t) + \nabla \cdot (\rho e_t \boldsymbol{v}) = -\nabla \cdot \boldsymbol{q} + \dot{Q} + \nabla \cdot (\tilde{\boldsymbol{\sigma}} \cdot \boldsymbol{v}) + \rho \sum_{i=1}^{NS} Y_i \boldsymbol{f}_i (\boldsymbol{v} + \boldsymbol{V}_i) \tag{5.8}$$

It is possible to integrate energy conservation equation (5.8) over a control volume V:

$$\frac{\mathrm{d}}{\mathrm{dt}}\iiint_V \rho e_t \mathrm{d}V + \iint_S \rho e_t \left[(\boldsymbol{v}-\boldsymbol{v}_I)\cdot\boldsymbol{n}\right]\mathrm{d}S = \\ = \iiint_V \dot{Q}\mathrm{d}V - \iint_S \boldsymbol{q}\cdot\boldsymbol{n}\mathrm{d}S + \iint_S \boldsymbol{v}\cdot\tilde{\boldsymbol{\sigma}}\boldsymbol{n}\mathrm{d}S + \iiint_V \rho\sum_{i=1}^{N} Y_i \boldsymbol{f}_i\left(\boldsymbol{v}+\boldsymbol{V}_i\right)\mathrm{d}V \quad (5.9)$$

In the approach from Kuo [51] the thickness of the control volume V is taken as approaching to zero with a limit operation, with volume integrals replaced by surface integrals, in order to recognize the balance at the wall interface. Having clear both the differential and the integral form of the governing equations, allows to apply an easier strategy to obtain an accurate formulation for the fuel inlet boundary treatment. In the next section an approach similar to the one discussed by [102] is described.

5.5 Gas-Solid Interface

In the case of pyrolisis in hybrid rocket engines using traditional fuel formulations, the boundary condition can be expressed as follows. First it is necessary to identify the different phases involved. Subscript g indicates the gaseous phase, subscript s indicates the solid phase (fuel) while subscript I indicates the interface, that in this case coincides with the fuel surface. Considering the species conservation, it is possible to write:

$$\rho_g Y_{i,g}(\boldsymbol{v}_g-\boldsymbol{v}_I)\cdot\boldsymbol{n}_g + \boldsymbol{J}_{i,g}\cdot\boldsymbol{n}_g - \rho_s Y_{i,s}(\boldsymbol{v}_s-\boldsymbol{v}_I)\cdot\boldsymbol{n}_g - \boldsymbol{J}_{i,s}\cdot\boldsymbol{n}_g = \dot{\omega}_i \quad (5.10)$$

this can be re-written as:

$$\rho_g Y_{i,g}(\boldsymbol{v}_g-\boldsymbol{v}_I)\cdot\boldsymbol{n}_g + \boldsymbol{J}_{i,g}\cdot\boldsymbol{n}_g = \rho_s Y_{i,s}(\boldsymbol{v}_s-\boldsymbol{v}_I)\cdot\boldsymbol{n}_g + \boldsymbol{J}_{i,s}\cdot\boldsymbol{n}_g + \dot{\omega}_i \quad (5.11)$$

Three hypothesis are valid in the considered case:

- no diffusion inside the solid, so that $\boldsymbol{J}_{i,s}=0$;
- the solid fuel is not moving, so that $\boldsymbol{v}_s=0$;
- no surface chemical reactions are present, so that $\dot{\omega}_i=0$.

This gives:

$$\rho_g Y_{i,g}(\boldsymbol{v}_g-\boldsymbol{v}_I)\cdot\boldsymbol{n}_g + \boldsymbol{J}_{i,g}\cdot\boldsymbol{n}_g = -\rho_s Y_{i,s}\boldsymbol{v}_I\cdot\boldsymbol{n}_g \quad (5.12)$$

Summing the species together, this gives:

$$\rho_g(\boldsymbol{v}_g-\boldsymbol{v}_I)\cdot\boldsymbol{n}_g = -\rho_s\boldsymbol{v}_I\cdot\boldsymbol{n}_g \quad (5.13)$$

Therefore:

$$\boldsymbol{v}_g\cdot\boldsymbol{n}_g = \frac{\rho_g-\rho_s}{\rho_g}\boldsymbol{v}_I\cdot\boldsymbol{n}_g \quad (5.14)$$

Backsubstituting equation (5.14) in equation (5.12), gives:

$$-Y_{i,g}\rho_s\boldsymbol{v}_I\cdot\boldsymbol{n}_g + \boldsymbol{J}_{i,g}\cdot\boldsymbol{n}_g = -Y_{i,s}\rho_s\boldsymbol{v}_I\cdot\boldsymbol{n}_g \quad (5.15)$$

and:

$$\boldsymbol{J}_{i,g} \cdot \boldsymbol{n}_g + (Y_{i,s} - Y_{i,g})\rho_s \boldsymbol{v}_I \cdot \boldsymbol{n}_g = 0 \tag{5.16}$$

Now considering the energy equation in the inernal energi form, it is possible to write:

$$\rho_g e_g(\boldsymbol{v}_g - \boldsymbol{v}_I) \cdot \boldsymbol{n}_g + p_g \boldsymbol{n}_g \cdot \boldsymbol{v}_g + \boldsymbol{q}_g \cdot \boldsymbol{n}_g = \rho_s e_s(\boldsymbol{v}_s - \boldsymbol{v}_I) \cdot \boldsymbol{n}_g + p_s \boldsymbol{n}_g \cdot \boldsymbol{v}_s + \boldsymbol{q}_s \cdot \boldsymbol{n}_g \tag{5.17}$$

Interest in the present work is to discuss energy equation in terms of enthalpy. Therefore, it is possible to add and subtract to left members of equation (5.17) a term $p_g \boldsymbol{n}_g \cdot \boldsymbol{v}_I$ and to the right member of the same equation a term $p_s \boldsymbol{n}_g \cdot \boldsymbol{v}_I$. It is then possible to gather the pressure terms $p_g \boldsymbol{n}_g \cdot (\boldsymbol{v}_g - \boldsymbol{v}_I)$ and $p_s \boldsymbol{n}_g \cdot (\boldsymbol{v}_s - \boldsymbol{v}_I)$ with the internal energy term to obtain enthalpy, which is defined as the sum of internal energy and pressure contributions. A pressure term will however survive:

$$\rho_g h_{st,g}(\boldsymbol{v}_g - \boldsymbol{v}_I) \cdot \boldsymbol{n}_g + p_g \boldsymbol{n}_g \cdot \boldsymbol{v}_I + \boldsymbol{q}_g \cdot \boldsymbol{n}_g = \rho_s h_{st,s}(\boldsymbol{v}_s - \boldsymbol{v}_I) \cdot \boldsymbol{n}_g + p_s \boldsymbol{n}_g \cdot \boldsymbol{v}_I + \boldsymbol{q}_s \cdot \boldsymbol{n}_g \tag{5.18}$$

If boundary layer is not separated, it does not present shock waves, work of viscous stresses is negligible, no surface tension is present and the geometry is plane it is reasonable to assume that the pressure difference across the interface is zero and the surviving pressure terms are negligible. This obviously because the left and right hand terms become equal and can be eliminated. This is a common technique, as in [93], and it is applied in the present work. Figure 5.3 summarizes the contributions to the energy balance at the interface.

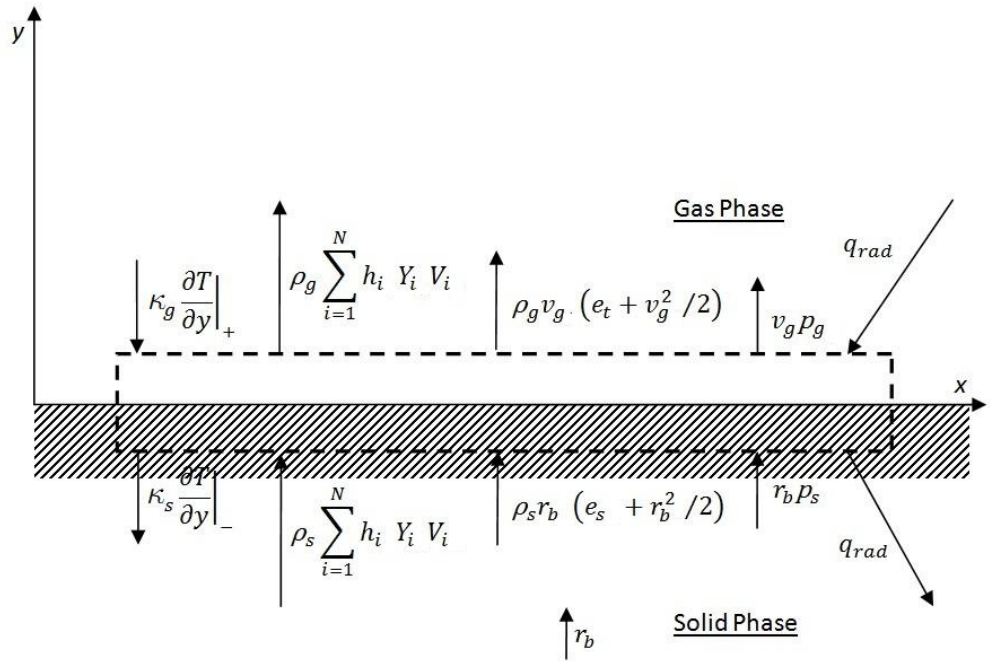

Figure 5.3: Gas-Solid interface scheme. In this figure, $r_b = \boldsymbol{v}_i \cdot \boldsymbol{n}_g$ while subscripts s and g indicate respectively the solid and the gas phase.

Being $h_{st,g}$ the static absolute enthalpy, in the previous equation (5.18) several contributions are neglected, such as:

- work of viscous stresses;
- radiation;
- kinetic energy
- Dufour effect

The work of viscous stresses, the kinetic energy and Dufour effect are negligible for combustion flow conditions because their contribution is much smaller than reaction enthalpy. The radiation effect should be considered with care: its contribution is of mandatory importance for fuel formulations where the presence of metals is significant. Otherwise, such as in this case, it can be neglected in first approximation. In the gas phase, the heat flux is:

$$\boldsymbol{q}_g = -\kappa_g \nabla T_g + \sum_{i=1}^{NS} h_i \boldsymbol{J}_{i,g} \tag{5.19}$$

In the solid phase, the heat flux is:

$$\boldsymbol{q}_s = -\kappa_s \nabla T_s \tag{5.20}$$

Therefore, substituting equations (5.19) and (5.20) in equation (5.18) gives:

$$\rho_g h_{st,g}(\boldsymbol{v}_g - \boldsymbol{v}_I) \cdot \boldsymbol{n}_g - \kappa_g \nabla T_g + \sum_{i=1}^{NS} h_i \boldsymbol{J}_{i,g} \cdot \boldsymbol{n}_g = -\rho_s h_{st,s} \boldsymbol{v}_I \cdot \boldsymbol{n}_g - \kappa_s \nabla T_s \cdot \boldsymbol{n}_g \tag{5.21}$$

Substituting equation (5.14) in equation (5.21) gives:

$$-\rho_s h_{st,g} \boldsymbol{v}_I \cdot \boldsymbol{n}_g - \kappa_g \nabla T_g + \sum_{i=1}^{NS} h_i \boldsymbol{J}_{i,g} \cdot \boldsymbol{n}_g = -\rho_s h_s \boldsymbol{v}_I \cdot \boldsymbol{n}_g - \kappa_s \nabla T_s \cdot \boldsymbol{n}_g \tag{5.22}$$

Under the hypothesis that the fuel is made only of one species and this species transforms from solid state to gaseous state by pyrolisis (which is analogous and coherent to the hypothesis that gaseous 1,3-butadiene is the only pyrolisis product for HTPB fuels), it is possible to write:

$$h_{st,s} = h_{st,g} - \Delta h_{pf} \tag{5.23}$$

where h_{gf} is the absoulte enthalpy of fuel in the gaseous state and Δh_{pf} is the enthalpy of pyrolisis for the fuel. The final form is:

$$-\rho_s h_{st,g} \boldsymbol{v}_I \cdot \boldsymbol{n}_g - \kappa_g \nabla T_g + \sum_{i=1}^{NS} h_i \boldsymbol{J}_{i,g} \cdot \boldsymbol{n}_g = -\rho_s (h_{gf} - \Delta h_{pf}) \boldsymbol{v}_I \cdot \boldsymbol{n}_g - \kappa_s \nabla T_s \cdot \boldsymbol{n}_g \tag{5.24}$$

5.5.1 Regression BC Implementation

It is possible to use equation (5.24) expliciting the terms as needed for the numerical implementation. In order to do this, it is necessary to define the interface velocity as a function of fuel regression rate r_b, such as:

$$\boldsymbol{v}_I \cdot \boldsymbol{n}_g = -r_b \tag{5.25}$$

This gives:

$$\rho_s h_g r_b - \kappa_g \nabla T_g^w \cdot \boldsymbol{n}_g + \sum_{i=1}^{NS} \boldsymbol{J}_{i,g} \cdot \boldsymbol{n}_g h_{g,i} = -\kappa_s \nabla T_s^w \cdot \boldsymbol{n}_g + \rho_s r_b (h_{gf} - \Delta h_{pf}) \tag{5.26}$$

Previous relation (5.26) gives energy, therefore temperature balance at wall. In order to fully characterize the boundary condition, it is necessary to determine also mass fractions and velocity components. Mass fraction balance at wall can be written, from equation (5.16) and taking into account that $Y_{i,s} = 0$ when $i \neq$ fuel, as:

$$\boldsymbol{J}_{i,g} \cdot \boldsymbol{n}_g = \begin{cases} (Y_{i,s} - Y_{i,g})\bar{\omega} & \text{if i = fuel} \\ -Y_{i,g}\bar{\omega} & \text{else} \end{cases} \tag{5.27}$$

By the use of conservation of mass equation at wall, velocity components are obtained as:

$$\boldsymbol{v}_g \cdot \boldsymbol{n} = \frac{\rho_s - \rho_g}{\rho_g} r_b = \frac{\rho_s - \rho_g}{\rho_g \rho_s} \bar{\omega} \tag{5.28}$$

Noticeably equations (5.26), (5.27) and (5.28) constitute a non-linear system with respect to mass fractions, temperature and velocity components $\boldsymbol{v}_g \cdot \boldsymbol{n}$, where the unknowns are wall variables: in fact diffusion flux is defined as the gradient of mass fractions even under the simplest Fickian diffusion hypothesis. Therefore an iterative solution procedure for this system has to be applied. Initial guesses are given for both wall mass fractions and wall temperature. Then a quasi-Newton iteration with numerical jacobian is performed for mass fraction equation. The output mass fraction array is then used inside a *false position* iteration [104] in order to obtain wall temperature: this method combines features from both bisection method and secant method. The difference between secant and false position methods relies in the fact that the latter retains the last two points that bracketed a root instead of the last two computed points (whether they bracket or not the root). Several other methods such as classic bisection method, secant method, Brent [105] method and Ridders [106] method were tested. Anyhow the false position method proved itself as a good compromise between robustness in bracketing the root and computational cost. The closure of this non-linear problem requires also a model for the fuel pyrolisis law. This is obtained applying an Arrhenius-type law from [107]:

$$r_b = A \exp\left(-\frac{E_a}{R_u T_s}\right) \begin{cases} A = 11.04 \text{ mm/s}, & E_a = 4.91 \text{ kcal/mol} \quad \text{if } T \geq 722K \\ A = 3965 \text{ mm/s}, & E_a = 13.35 \text{ kcal/mol} \quad \text{if } T < 722K \end{cases} \tag{5.29}$$

Solid fuel data		
Property	**Symbol**	**Value**
Fuel density	ρ_f	960 kg/m^3
Specific heat	c_f	2860 J/kgK
Enthalpy	h_{pf}	1100000 J
Thermal conductivity	κ_s	0.217 W/mK
Fuel temperature, far from surface	T_0	300 K

Table 5.3: Solid fuel data used in this work

This pyrolisis law was obtained experimentally by Chiaverini et al. [107] through rapid heating of HTPB-based hybrid rocket fuel using thermogravimetric analysis (TGA) and differential thermal analysis (DTA) techiques. Solid fuel data such as density and enthalpy are also needed to fully close the boundary problem. These are shown in table 5.3 and are collected from SPLab work [103], where a comprehensive study of traditional butadiene-based and innovative paraffin-based fuels is described. In addition, in order to obtain the gradient of solid fuel temperature, the well-known [108] equation for one dimensional heat conduction is applied as in the recent works of Cai et al. [120]:

$$T(y) = T_0 + (T_s - T_0)exp\left(-\frac{\rho_f c_f r_b y}{\kappa_f}\right) \tag{5.30}$$

At fuel surface, where $y = 0$, the temperature gradient is:

$$-\kappa_s \nabla T_s^w = \rho_f c_f r_b (T_s - T_0) \tag{5.31}$$

Chapter 6

Results and Discussion

This chapter presents and describes the main results from the numerical simulations performed during doctoral thesis work. It starts from the basic tests for non-reacting flows (laminar and turbulent) and develops the discussion into more complex reacting conditions (laminar and turbulent, for different chemical models) with increasing industrial and academic relevance. Part of this chapter was presented by the author at 5th European Conference for Aeronautics and Space Sciences held from 1 to 5 July 2013 in Munich, [109].

6.1 General Code Validation

COOLFLuiD code was successfully applied in several numerical simulation tasks from different fields, such as: aerodynamics, aerothermodynamics, magnetohydrodynamics, electrochemistry, structural analysis, aeroelasticity, aeroacustics and heat transfer. A general validation of code accuracy and capability of correctly capture the physics of various problems, is already available. For this reason, a general view of code results and validation can be found in [87], [88] and [89]. Starting from this point, a complete validation of the code was deemed as not necessary. Anyhow some simplified testcases are implemented in order to assess the correct behaviour of numerical simulation results in comparison with problem physics. This in particular to validate the turbulence model, the combustion model and their coupling, being the two the addition to COOLFluiD code due to this doctoral work.

6.2 Considerations on Convergence and CFL condition

COOLFluiD code embeds the possibility to monitor the norm of the residual, and its history, for each one of the problem variables. In the present case the variables used are the partial densities ρ_i, the velocity components u (along the channel axis) and v (perpendicular to the channel axis), temperature T and the turbulence quantities k and ω. As a default parameter, convergence is reached for a residual norm below 10^{-4}. The present work did not address a numerical analysis in terms of residual convergence, being focused on the correspondence of simulation results with real problem physics. Nevertheless all results in the following sections are presented at the steady state, with solution results stable in time: no variation in the solution is noticeable with subsequent iterations. Some important considerations, however, can be done in terms of CFL value used for the simulations, with particular attention to the different phases of combustion. As a general trend, the ignition phase is more delicate in terms of convergence: for the initial part of the simulation, when ignition occurs, CFL value must be kept lower than the one to be used in the following parts of the simulations. This effect becomes even more important with increasing pressure: higher pressure results in the necessity for a smaller CFL value in the beginning phase of the simulation. Furthermore, at higher pressures, a lower CFL value is needed to reach convergence throughout all the simulation.

6.3 Non-reacting Case

6.3.1 Laminar vs. Turbulent Case

First tests aimed at the validation of non-reacting flow inside the combustion chamber for both laminar and turblent conditions in non-reacting environment. Only one chemical species is present, $O2$. Inlet speed is 60 m/s and turbulence (when present) si considered to be fully developed. The main objective is therefore to demonstrate the ability of the code to solve laminar and turbulent boundary layers with results which are coherent with problem physics. Significant results are shown in figures 6.1 and 6.2, the former depicting the numerical results and the latter depicting experimental results from [110].

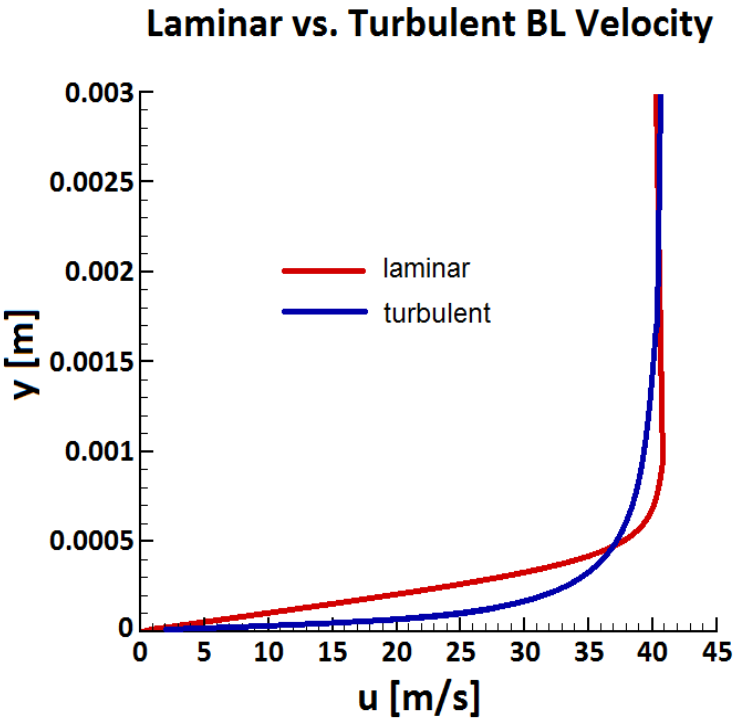

Figure 6.1: Laminar vs. turbulent boundary layer velocity numerical results, from COOLFluiD

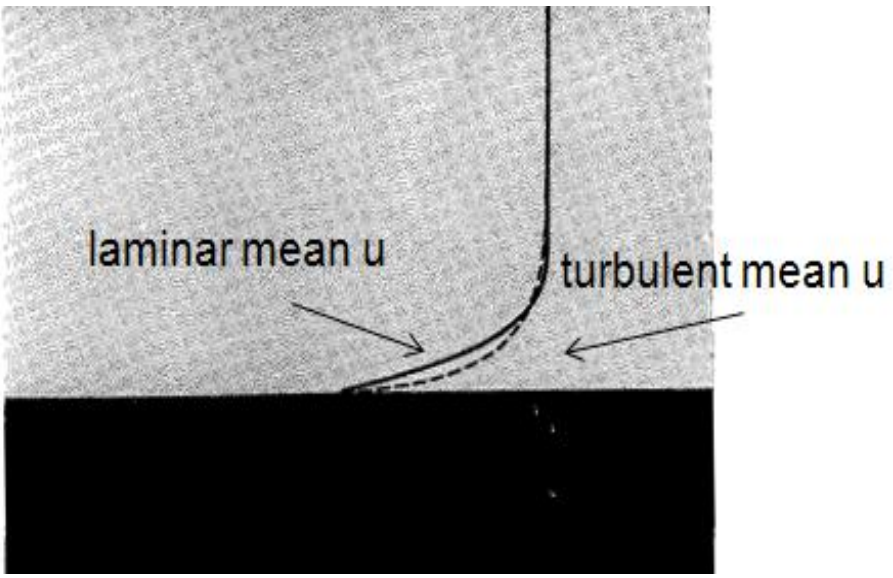

Figure 6.2: Laminar vs. turbulent boundary layer velocity experimental results, from [110]

The trends of velocity profiles at wall from previous figures show a very good accord between the numerical and the experimental results. In addition some comparisons were performed with the COSMIC code [111], showing good accord between the results.

Therefore COOLFluiD code can be considered able to solve correctly laminar and turbulent boundary layers.

6.4 Reacting Case - Laminar Flow

Once obtained the demonstration for the code to correctly solve non-reacting turbulent condition with good accord to problem physics, test were performed in order to validate combustion models.

6.4.1 Test Model Venkateswaran-2 - PSR

First reacting test is performed in laminar conditions, with the Venkateswaran [3] two-chemical reactions and five-chemical species model previously described and with boundary conditions as in chapter 5. For this case only first-approach calculations with imposed fuel temperature and fuel inlet speed are performed. Chemical source terms are treated, as first approach, under quasi-laminar hypothesis (Perfectly Stirred Reactor). Results are presented in terms of:

- temperature, axial velocity, reactants (C_4H_6, O_2) and products (H_2O, CO and CO_2) flow fields;

- temperature, axial velocity, reactants (C_4H_6, O_2) and products (H_2O, CO and CO_2) profiles at three different combustion chamber sections ($x = 75$ mm, 100 mm and 120 mm).

Results are shown in figures from 6.3 to 6.8:

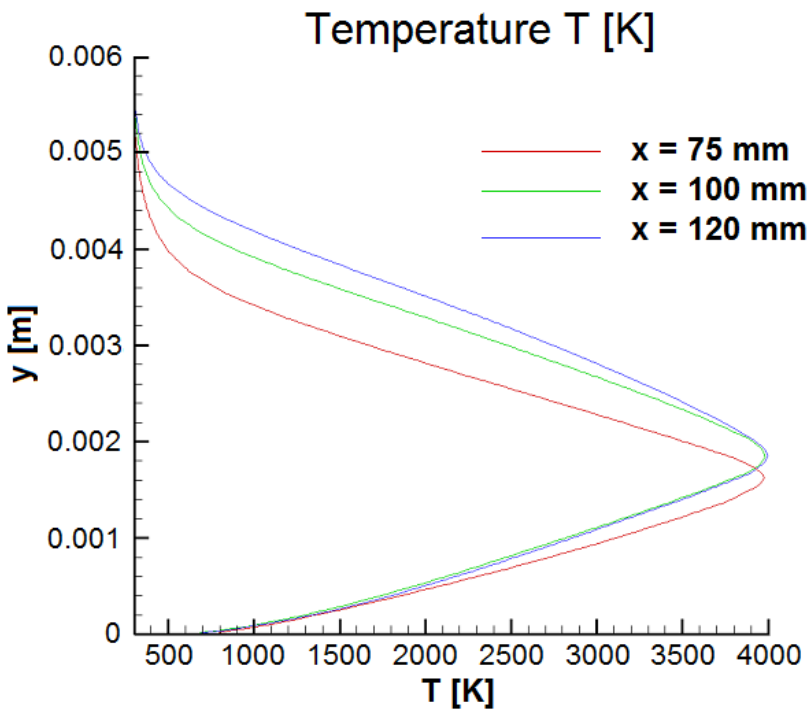

Figure 6.3: Section profiles of temperature. Reacting case, laminar combustion.

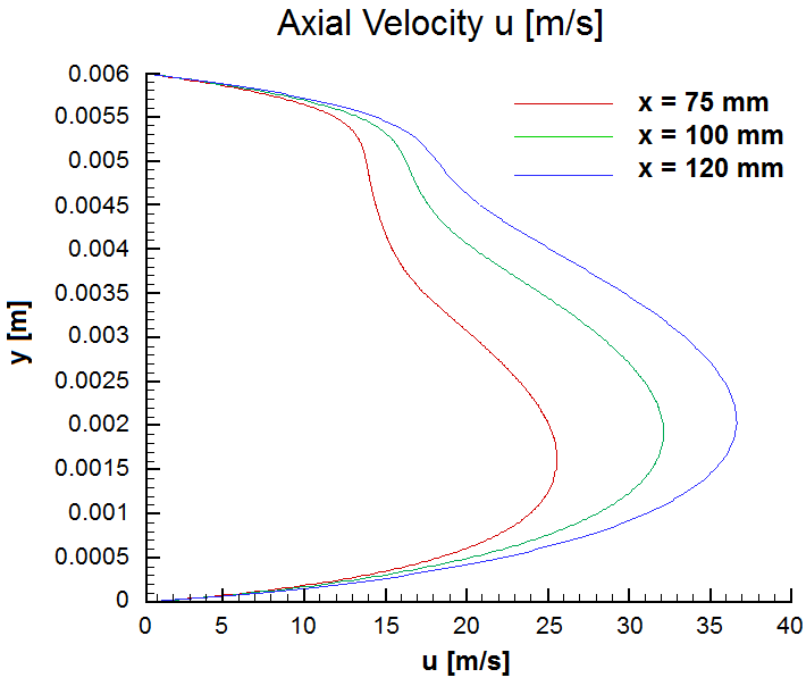

Figure 6.4: Section profiles of axial velocity component u. Reacting case, laminar combustion.

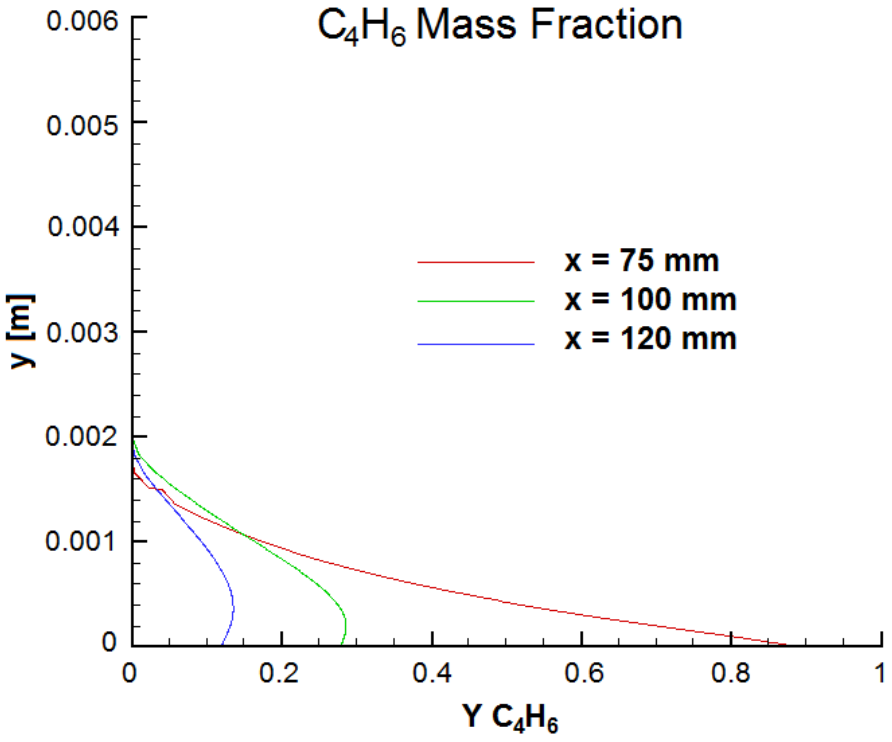

Figure 6.5: Section profiles C_4H_6 mass fraction. Reacting case, laminar combustion.

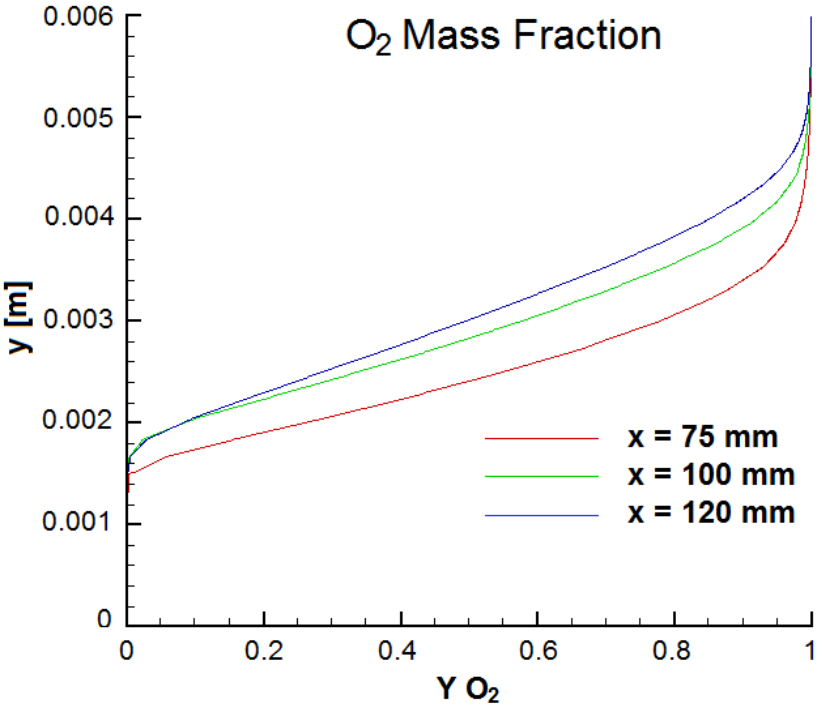

Figure 6.6: Section profiles O_2 mass fraction. Reacting case, laminar combustion.

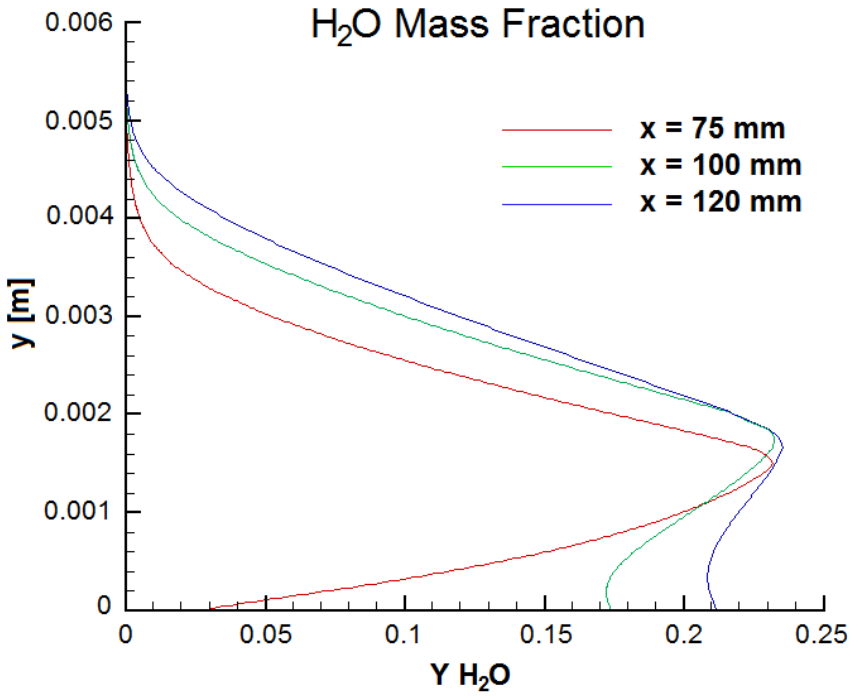

Figure 6.7: Section profiles H_2O mass fraction. Reacting case, laminar combustion.

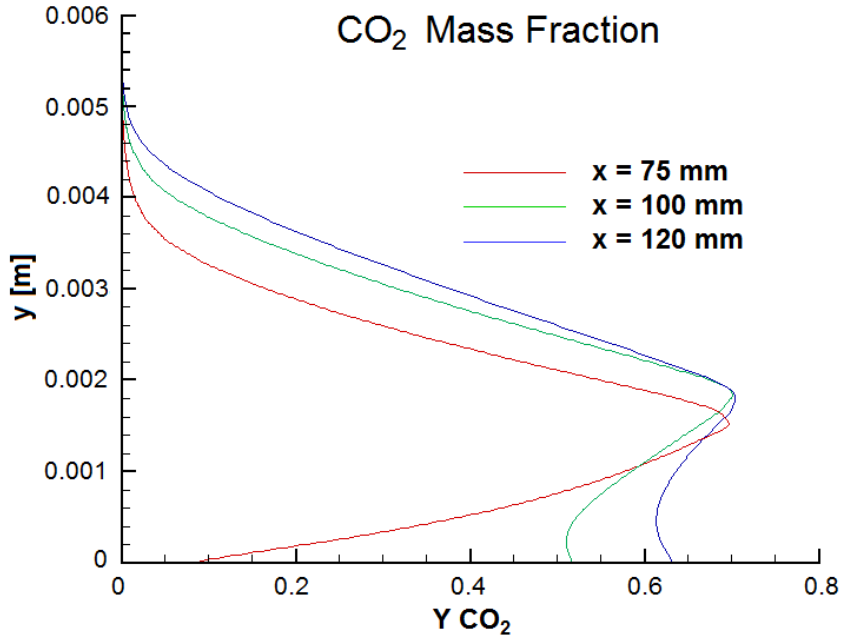

Figure 6.8: Section profiles CO_2 mass fraction. Reacting case, laminar combustion.

Flame structure corresponds to expected problem physics, with a relatively narrow peak region in the mid-lower section of the channel, starting from the fuel inlet, as noticeable from figure 6.3. The peak temperature is near 4000 K, which is higher than expected. This issue will be discussed in the next section, where Venkateswaran model will

be tested in turbulent conditions. Due to mass conservation, flow is accelerated and an axial velocity peak is found, as shown in figure 6.4, with a value near 35 m/s. Reactant distribution is coherent with inlet positioning:

- fuel remains in the lower region, then it is progressively burnt along the combustion chamber as shown in figure 6.5;

- oxidizer remains in the top region and reacts in the flame region, as shown in figure 6.6.

Products distribution is coherent with peak temperature region, were chemical reactions are more intense. In accord with problem physics, product species are able to diffuse and reactions to complete along the combustion chamber, as shown in figures 6.7 and 6.8. Next step is to test reacting conditions coupled with turbulence model.

6.5 Reacting Case - Turbulent Flow

6.5.1 Test Model Venkateswaran-2 - PSR

Once successfully tested in laminar conditions, a turbulent test for the reacting Venkateswaran model is in order. Now the flow field is treated with the $k-\omega$ model described in chapter 3. Chemical source term is still treated under quasi-laminar hypothesis (PSR). Results are presented in terms of:

- temperature, axial velocity, reactants (C_4H_6, O_2) and products (H_2O, CO and CO_2) flow fields;

- temperature, axial velocity, reactants (C_4H_6, O_2) and products (H_2O, CO and CO_2) profiles at three different combustion chamber sections ($x = 75$ mm, 100 mm and 120 mm).

Results are shown in figures from 6.9 to 6.14:

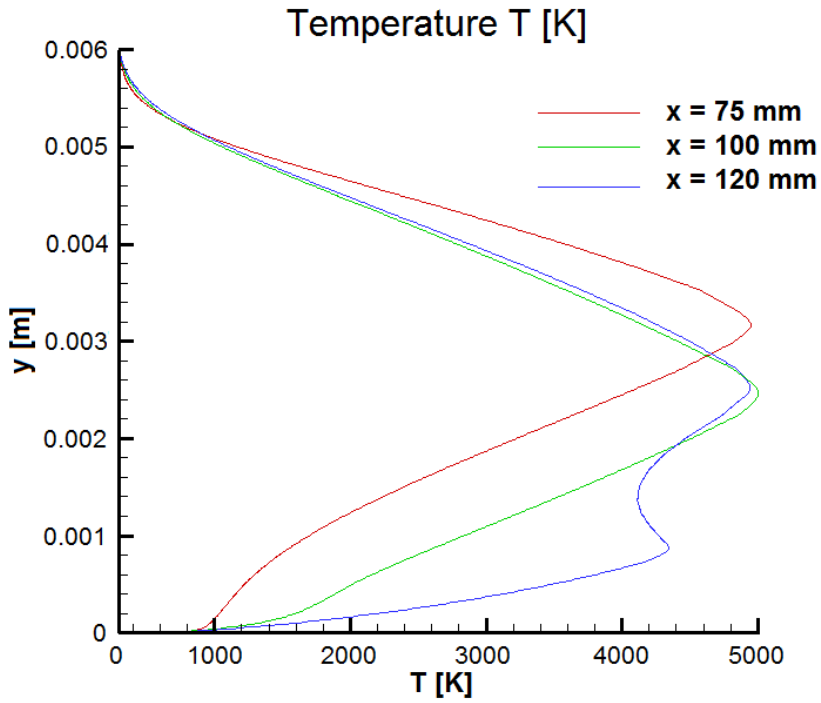

Figure 6.9: Section profiles of temperature. Reacting case, turbulent combustion. Test Model Venka2.

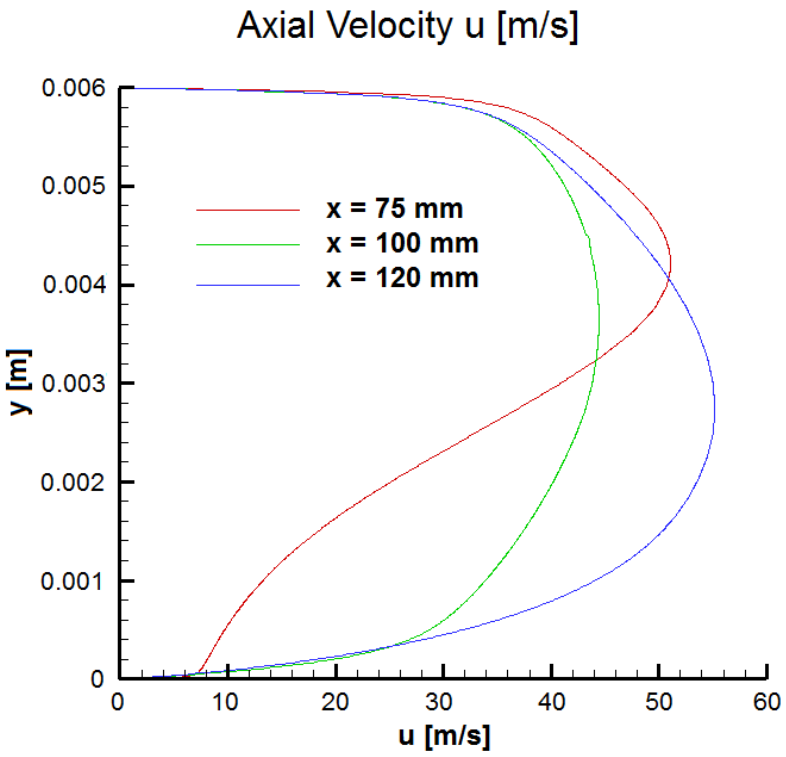

Figure 6.10: Section profiles of axial velocity component u. Reacting case, turbulent combustion. Test Model Venka2.

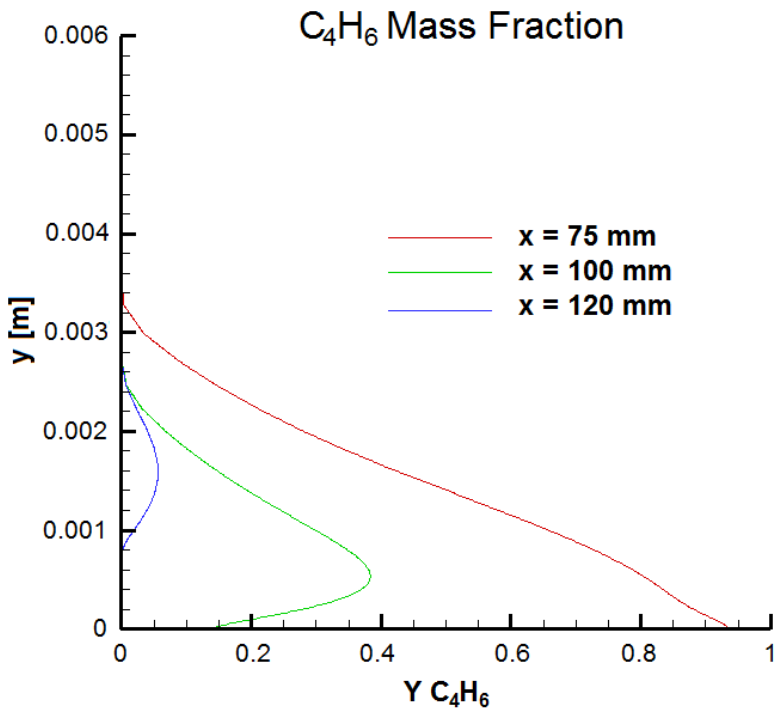

Figure 6.11: Section profiles C_4H_6 mass fraction. Reacting case, turbulent combustion. Test Model Venka2.

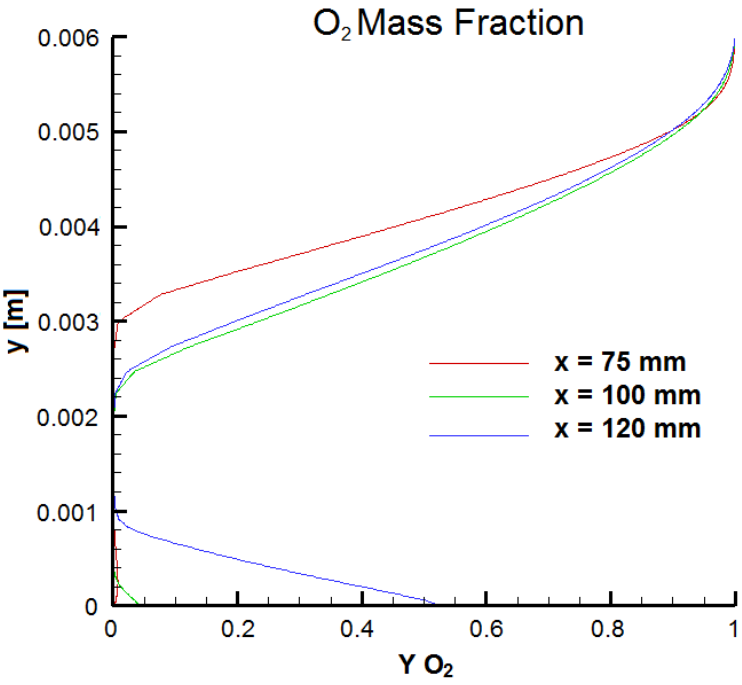

Figure 6.12: Section profiles O_2 mass fraction. Reacting case, turbulent combustion. Test Model Venka2.

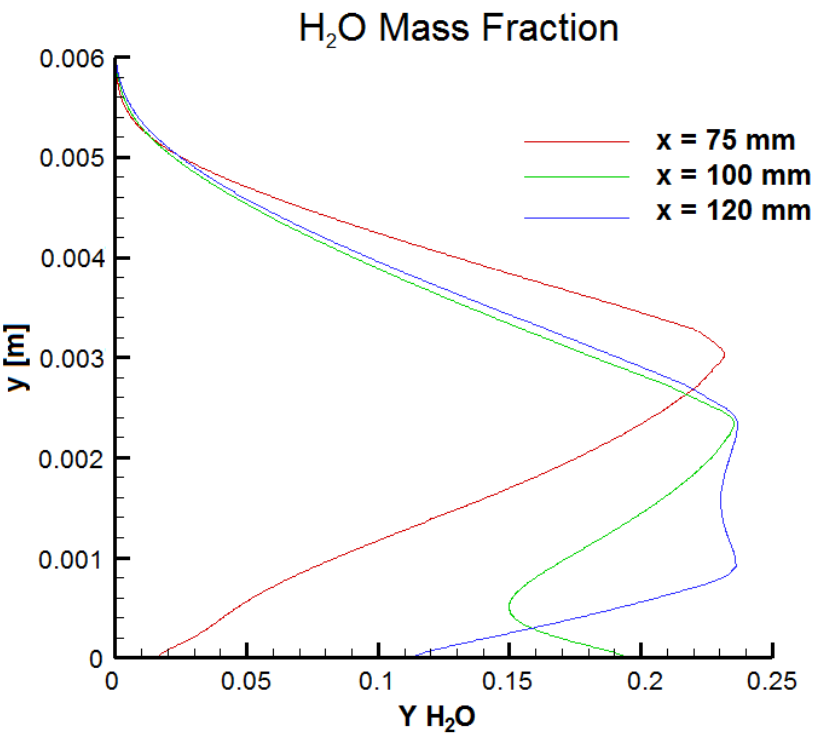

Figure 6.13: Section profiles H_2O mass fraction. Reacting case, turbulent combustion. Test Model Venka2.

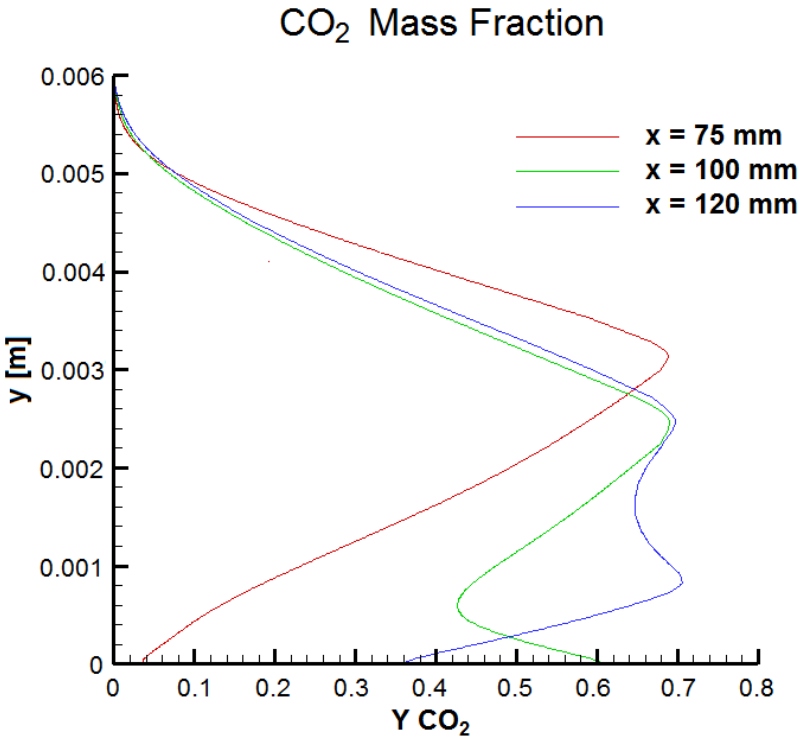

Figure 6.14: Section profiles CO_2 mass fraction. Reacting case, turbulent combustion. Test Model Venka2.

Flame structure once again shows good correspondence with expected problem physics, with a temperature peak near the mid-height of the channel and starting from the fuel inlet, as noticeable from figure 6.9. The peak temperature is over 4500 K, which is even higher than the overshoot found for the same chemical model in laminar condition. Even if not mentioned in the original work of [3], this issue is confirmed by the results from [44]. Mass conservation is respected and flow accelerates with an axial velocity peak of approximatively 55 m/s, as shown in figure 6.10. Reactant distribution is again coherent with inlet positioning and with peak temperature region:

- fuel remains in the lower region and it progressively reacts along the combustion chamber as shown in figure 6.11;
- oxidizer is mostly present in the top region, but it is also present in significant percentage near combustor end, as shown in figure 6.12.

Products distribution is coherent with oxidizer/fuel distibution and peak temperature. Because non-negligible fuel and oxidizer fractions are found near the lower wall at the combustor end, in accord with problem physics, product species are able to diffuse and reactions to complete along the combustion chamber, in this area a secondary peak is found for tempearature and products mass fractions, as shown in figures 6.9, 6.13 and 6.14. From these results arises the need for the investigation of a more detailed chemcal

model, able to accurately capture the flame peak temperature without unphysical overshooting. In the author opinion, in fact, such a simplified model as the two-reaction/five-species proves itself inadequately accurate for a correct and quantitative study of combustion processes in hybrid rocket engine. Also the Jones-Lindstedt four-reaction, six-species model does not seem a suitable candidate: lacking any strong energy-absorbing chemical processes, therefore posing itself in the same condition as the Venkateswaran two-reaction model. Therefore the six-reaction, nine-species model from Jones and Lindstedt [61] is considered as the best candidate for next tests, which are discussed in the followng section.

6.5.2 Test Model Jones-Lindstedt 6 - PSR Model Results

A first set of results is presented in figures from 6.15 to 6.27. This set refers to boundary conditions from table 5.1 in turbulent, reacting and pseudo-laminar chemistry (PSR) conditions. Figures 6.16 and 6.18 show the field of velocity component u and its section profiles at several locations along the channel. A significant increase in speed is noticeable, with a peak near to 56 m/s, due to expansion of hot gases. The peak temperature, near 3500 K, and the flame geometry are in line with literature results, as in Venkateswaran and Merkle [3], Cheng et al. [4] and Cai et al. [112]. Although conditions are fully turbulent and an accurate model for turbulent transport of energy is used, as shown in equation 3.43, structure and geometry of the flame remain very similar to the laminar flame, as in Law [113]. This indicates that even if the model is fully turbulent, PSR approach maintains a laminar flame structure. Figures 6.19 to 6.27 show the distribution of species mass fractions in the domain. It is noticeable how the peak of reaction products follows the temperature peak, as expected from the problem physics. In the highest temperature region H_2O dissociates into O and OH and O_2 dissociates in O. CO_2, which appears in the chemical model only as reaction product, is generated homogeneously along the flame. As also expected by problem physics, being H_2O a reactant in the production of CO_2, it is possible to notice a separation between the regions where mass fractions of these two species are present. The same phenomena involves also H_2 mass fraction with respect to H_2O mass fraction, being the first a reaction antagonist of the latter in all the chemical reactions involving both of them.

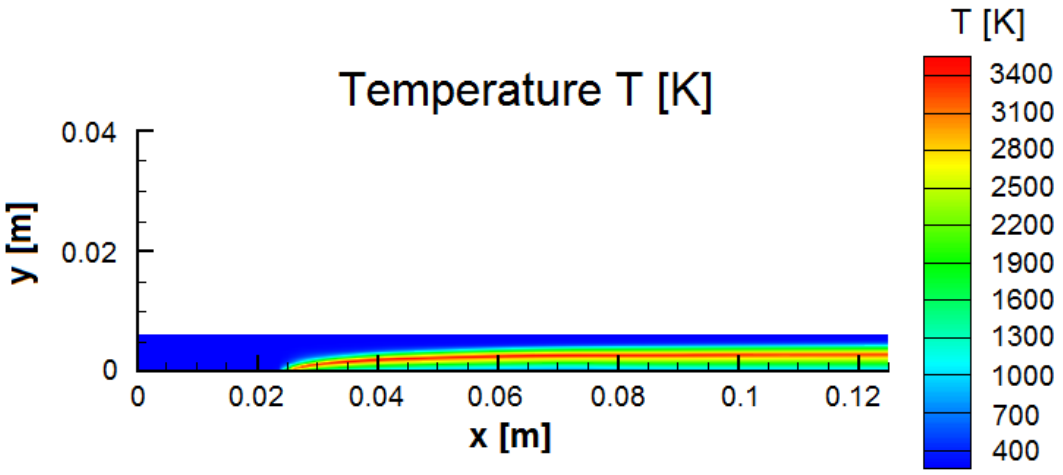

Figure 6.15: Field of temperature T - PSR. Reacting case, turbulent combustion. Test Model Jones6.

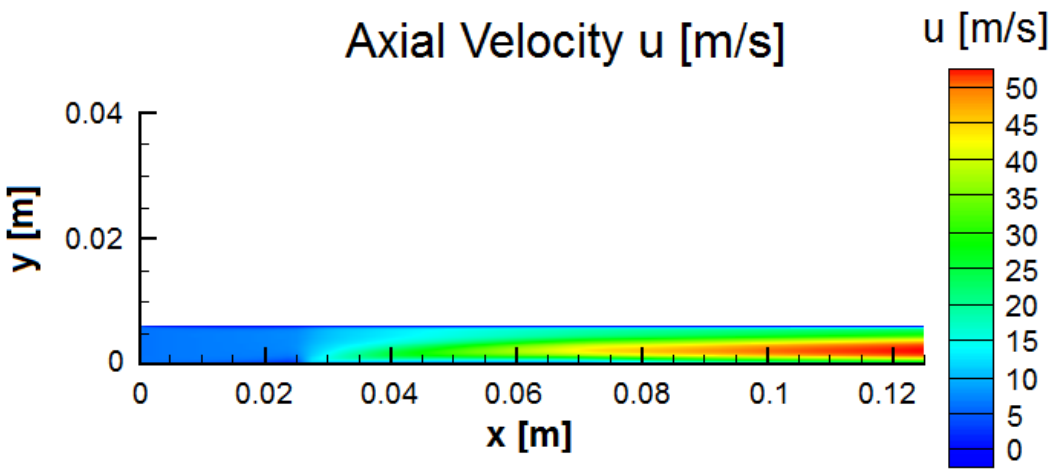

Figure 6.16: Field of axial velocity component u - PSR. Reacting case, turbulent combustion. Test Model Jones6.

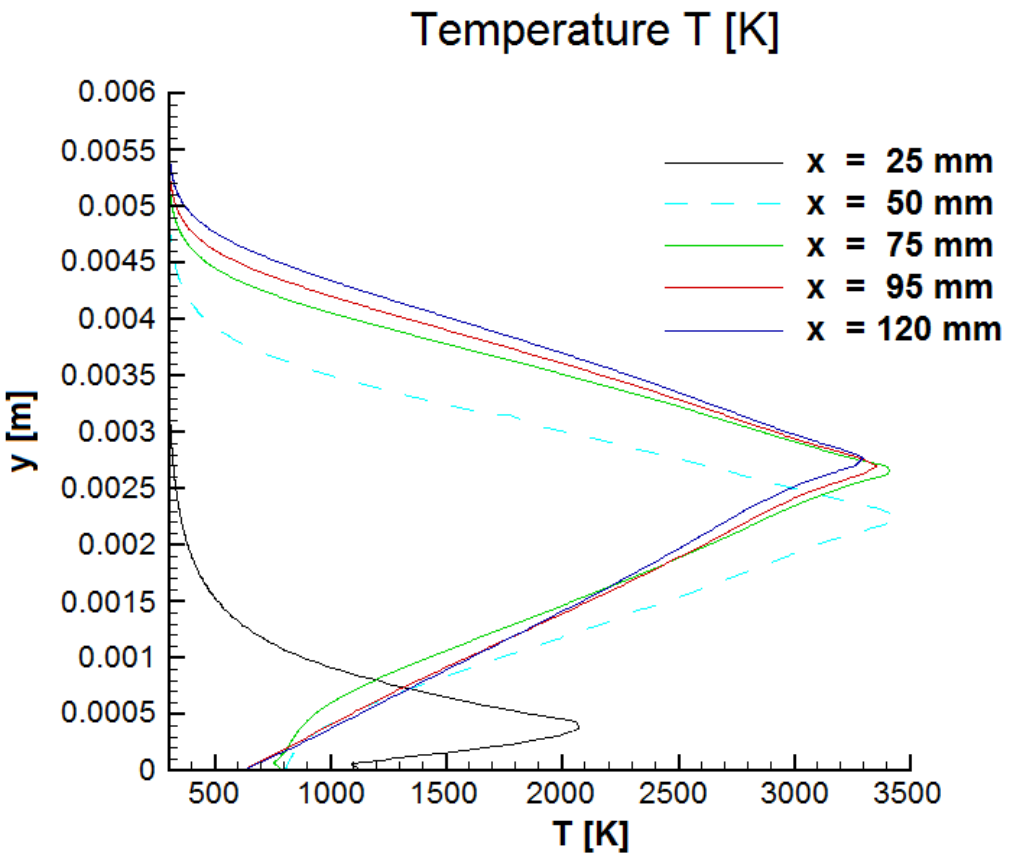

Figure 6.17: Section profiles of temperature T - PSR. Reacting case, turbulent combustion. Test Model Jones6.

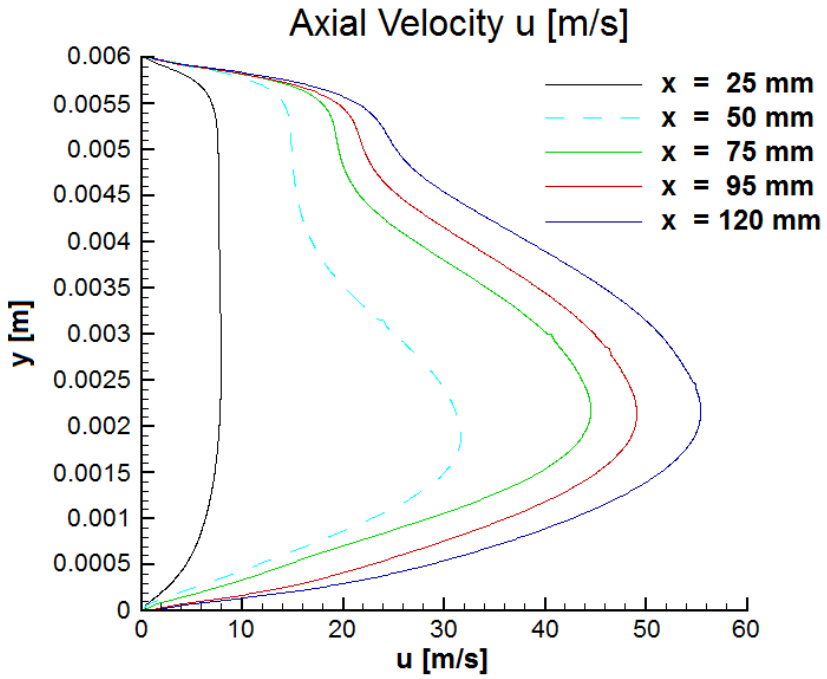

Figure 6.18: Section profiles of axial velocity component u - PSR. Reacting case, turbulent combustion. Test Model Jones6.

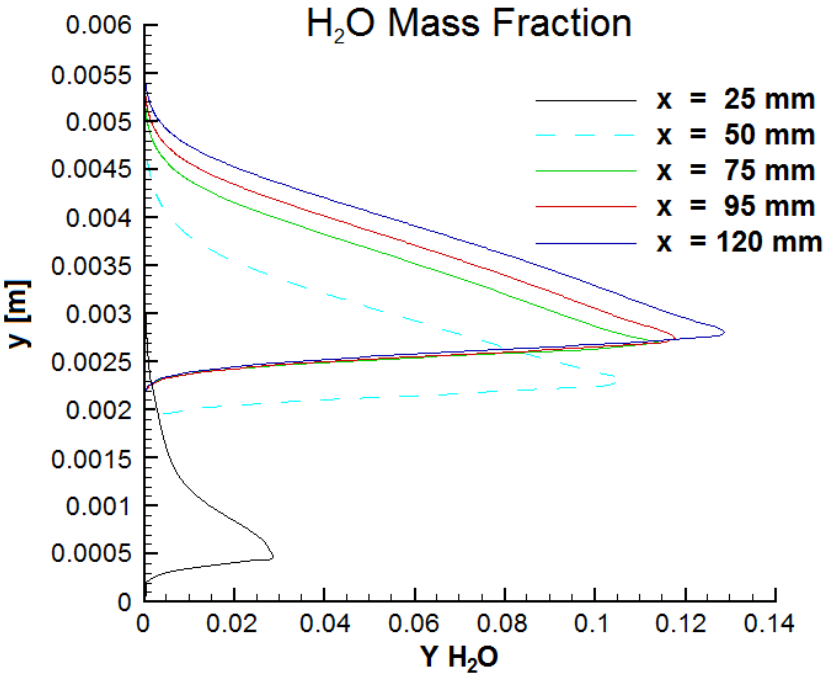

Figure 6.19: Section profiles of H_2O mass fraction - PSR. Reacting case, turbulent combustion. Test Model Jones6.

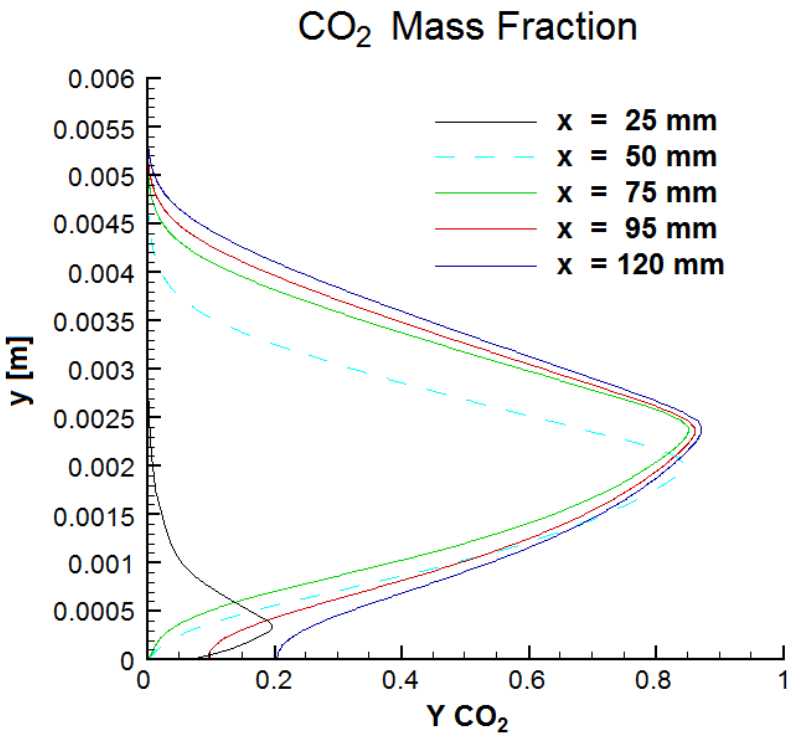

Figure 6.20: Section profiles of CO_2 mass fraction - PSR. Reacting case, turbulent combustion. Test Model Jones6.

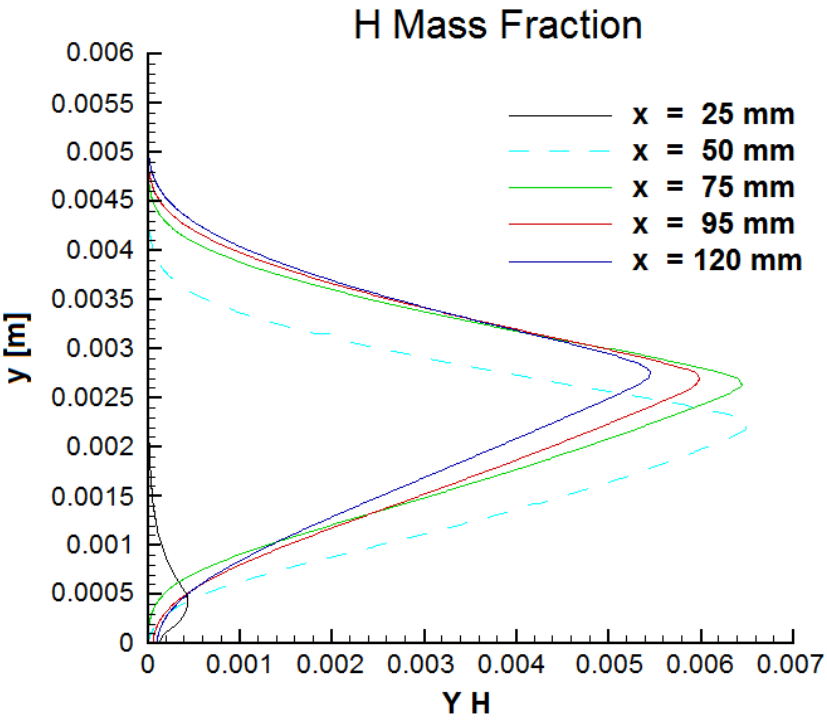

Figure 6.21: Section profiles of H mass fraction - PSR. Reacting case, turbulent combustion. Test Model Jones6.

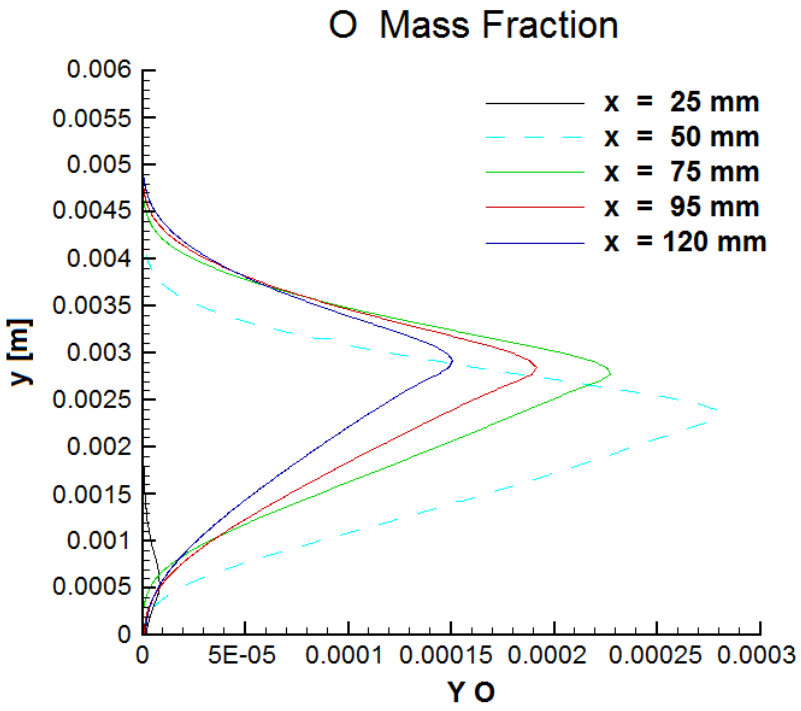

Figure 6.22: Section profiles of O mass fraction - PSR. Reacting case, turbulent combustion. Test Model Jones6.

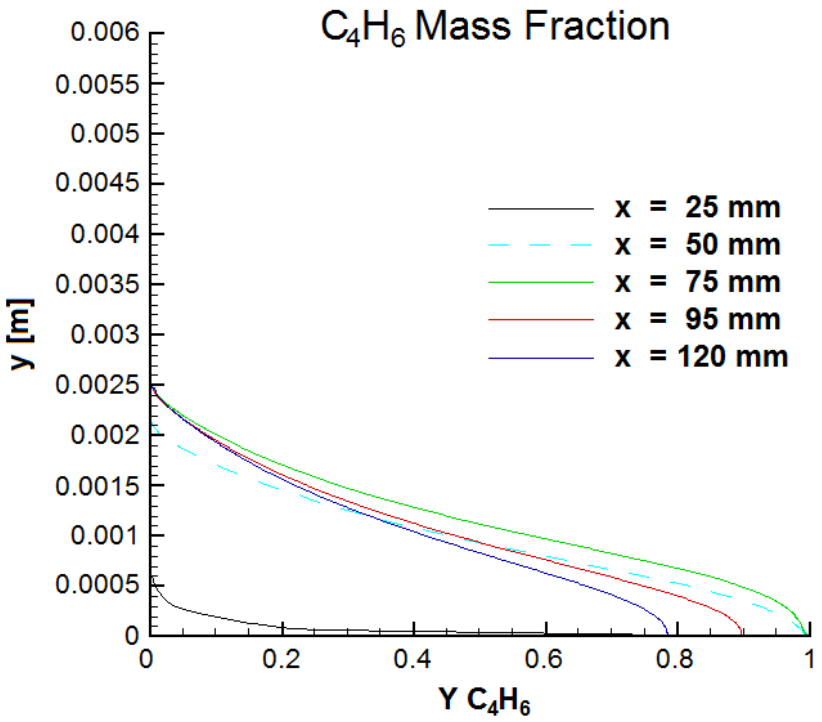

Figure 6.23: Section profiles of C_4H_6 mass fraction - PSR. Reacting case, turbulent combustion. Test Model Jones6.

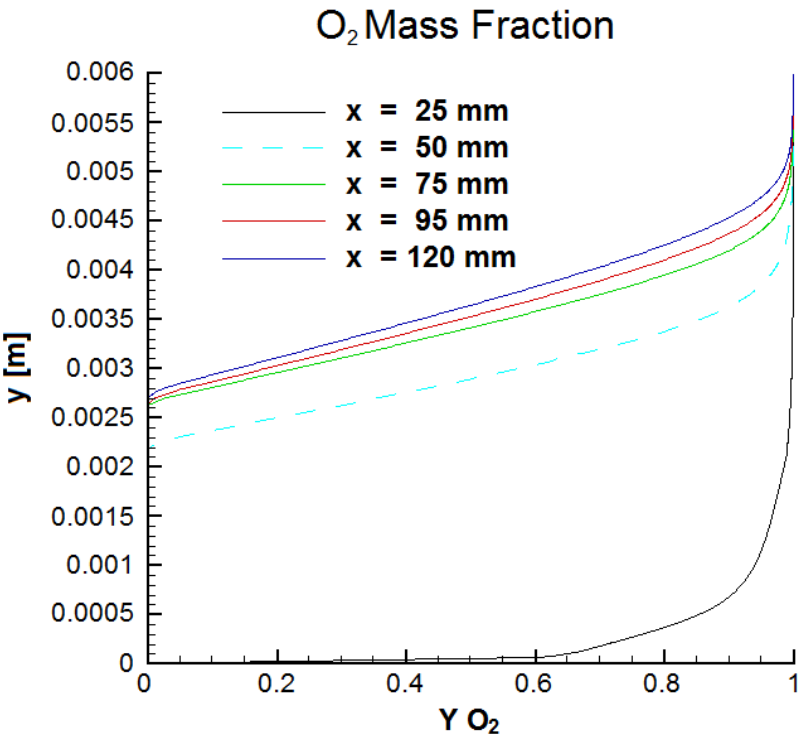

Figure 6.24: Section profiles of O_2 mass fraction - PSR. Reacting case, turbulent combustion. Test Model Jones6.

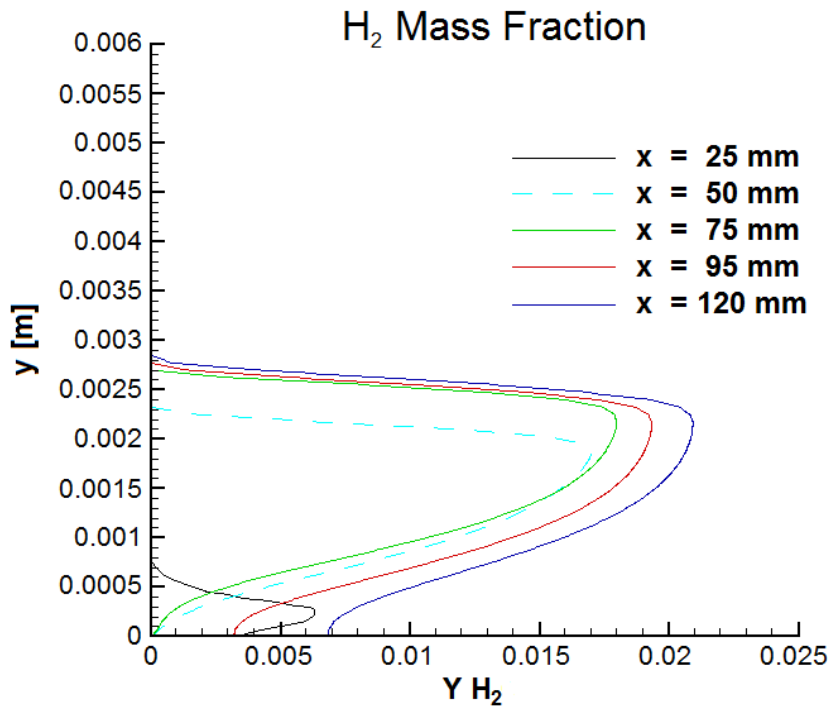

Figure 6.25: Section profiles of H_2 mass fraction - PSR. Reacting case, turbulent combustion. Test Model Jones6.

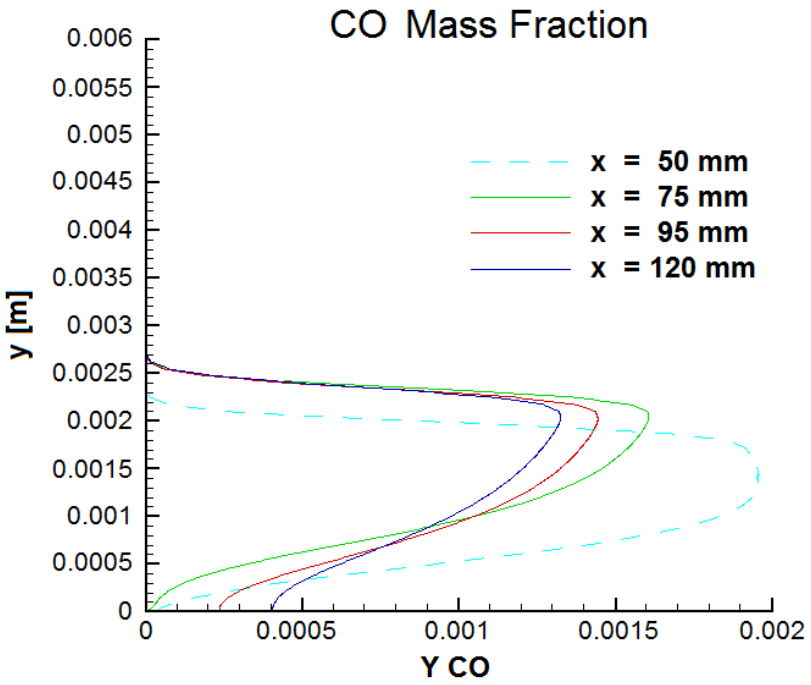

Figure 6.26: Section profiles of CO mass fraction - PSR. Reacting case, turbulent combustion. Test Model Jones6.

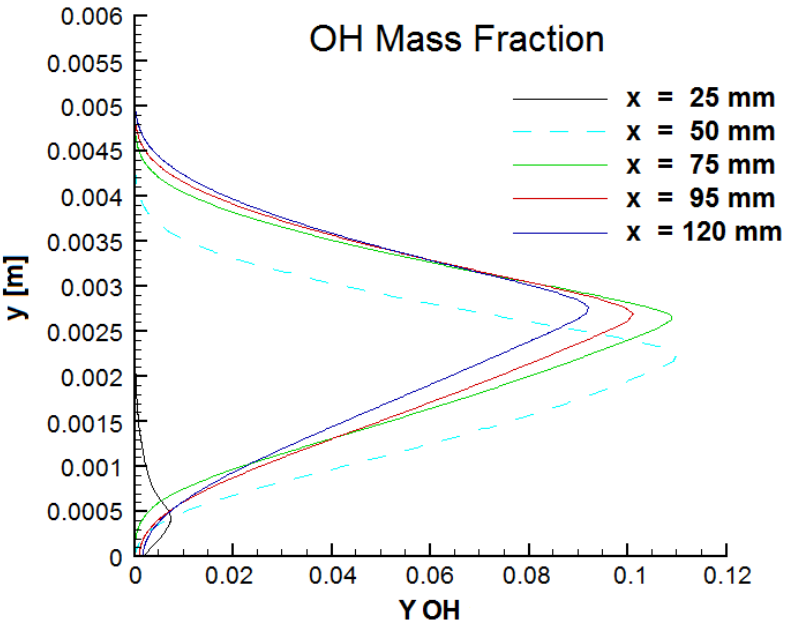

Figure 6.27: Section profiles of OH mass fraction - PSR. Reacting case, turbulent combustion. Test Model Jones6.

Influence of Inlet Velocity

Results are also presented for varying inlet speed conditions. From the starting case with 6 m/s oxidizer inlet speed, cases for 10 m/s, 15 m/s and 20 m/s are studied. For these cases fuel inlet velocity is increased accordingly to the increment in oxidizer mass flux. Therefore the values of v_{fuel} are 0.43 m/s, 0.65 m/s and 0.87 m/s corresponding respectively to inlet velocities of 10 m/s, 15 m/s and 20 m/s. Results are introduced in figure 6.28 as temperature profiles and in figure 6.29 as velocity profiles at x = 120 mm location (near combustor end). Increased inlet velocity results in increased temperature peak (from 3300 K at 6 m/s inlet speed to 3617 K at 20 m/s inlet speed, at the considered section). A significant increase in the maximum value for axial velocity is also noticeable. The peak velocity for the considered section (near combustor end) increases from 56 m/s for the minimum inlet speed tested to 128 m/s for the maximum speed considered.

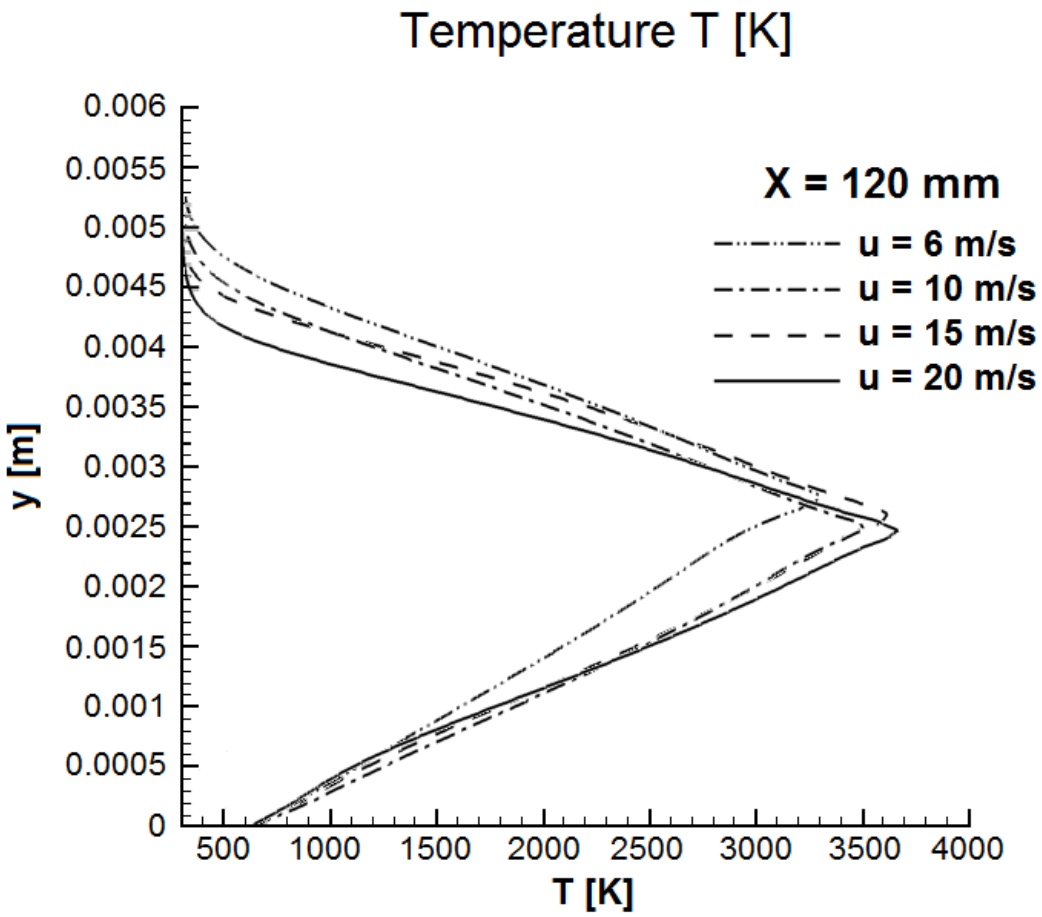

Figure 6.28: Section profiles of temperature with increasing inlet speed - PSR. Reacting case, turbulent combustion. Test Model Jones6.

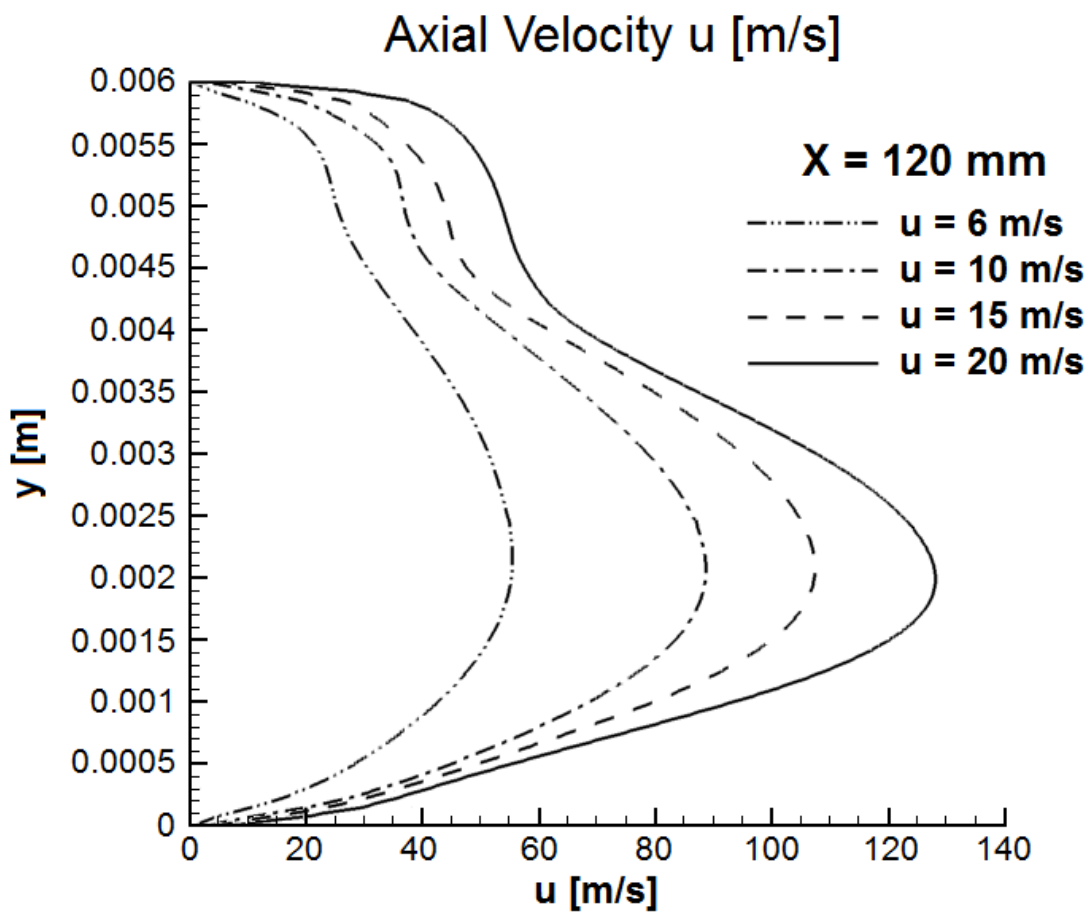

Figure 6.29: Section profiles of axial velocity component u with increasing inlet speed - PSR. Reacting case, turbulent combustion. Test Model Jones6.

6.5.3 Test Model Jones-Lindstedt 6 - PaSR Model Results, Single Slab

In this section results for a simulation comprehensive of PaSR approach is introduced. Boundary and initial conditions are once again the ones presented in tables 5.1 and 5.2. From figures 6.31 and 6.33 it can be noticed that a significant increase in axial speed, with respect to previous PSR case, is reached, with a peak of approximatively 87 m/s. As shown in figures 6.30 and 6.32, the peak temperature obtained with PaSR technique is lower with respect to pseudo-laminar flame, nearly 3350 K. The flame thickness, however, is significantly wider. In fact, with a PaSR approach, only part of each computational cell takes part in the combustion process. Therefore oxidizer and fuel species do not react in the same limited area as with PSR approach, because for each cell part of them reacts and part of them is transported farther by diffusion and turbulence. This process creates a wider zone where O/F is still adequate for combustion itself. In fact considering the region where $y < 0.003$ m, an excess of fuel is present. Conversely, for the region where $y > 0.003$ m, an excess of oxidizer is present. PaSR approach allows these mass fractions to diffuse farther to the flame before burning, therefore widening the flame area. In or-

der to show and better understand this phenomenon, figure 6.34 is presented. At the same location along the combustor x = 75 mm (fuel inlet end), section profiles for fuel and oxidizer species in PSR and PaSR cases are compared. For better understanding, an approximate flame zone is displayed. Considering oxidizer mass fraction, it is possible to notice that same mass fraction values are obtained farther from the peak temperature region, in y direction, for PaSR approach with respect to PSR. The same behavior is identified considering fuel mass fraction. In fact also in this case the same mass fraction value is obtained farther from the peak temperature zone with PaSR approach. Another approach to explain this is to consider mass fraction values again in figure 6.34, but at the same y level. If the same y is considered for PSR and PaSR comparison, lower values for both fuel and oxidizer mass fractions are noticeable for PaSR. This because PaSR flame is wider and therefore burns fuel and oxidizer at a greater distance from the peak temperature region. A larger higher temperature zone can also explain the increase of axial velocity switching from PSR to PaSR approach. In fact a wider area with lower density is present in PaSR simulation: in order to respect mass conservation, the flux of hot gases accelerates more than with PSR. Figures from 6.37 to 6.43 show the profiles of the main combustion products. As the problem physics would suggest, also with PaSR approach the composition of products tends to follow the temperature distribution, with a peak of products where temperature is higher. Due to the thicker flame, also reaction products show a wider curve along y coordinate. In accord with chemical model, also with PaSR approach a separation between the regions where H_2O and CO_2 species are present is noticeable. The same conclusion can be extended to H_2 and H_2O species. As PSR, also PaSR model reflects problem physics, with a clear separation of these two species in the combustor. A noticeable difference in the chemical composition of combustion products present in PaSR approach with respect to PSR is recognizable. A wider flame zone for PaSR gives an increased amount of the dissociated products H, O and OH. Moreover a significant increase in H_2O mass fraction and decrease in CO_2 mass fraction is noticeable for PaSR. A possible explanation for this phenomena can be given considering again figure 6.34. At the same height y, for y > 0.003 m, PSR has an excess of O_2 with respect to PaSR. The difference in O_2 mass fraction, thanks to the wider flame of PaSR, has reacted (when PaSR is active) to produce additional H_2O as in reaction 4) from table 3.2. The produced H_2O cannot diffuse below y = 0.003 m, because it encounters the region with maximum temperature and then dissociates into H, O and OH. Because of conservation of chemical species mass, an excess of H_2O corresponds in a decrease of CO_2.

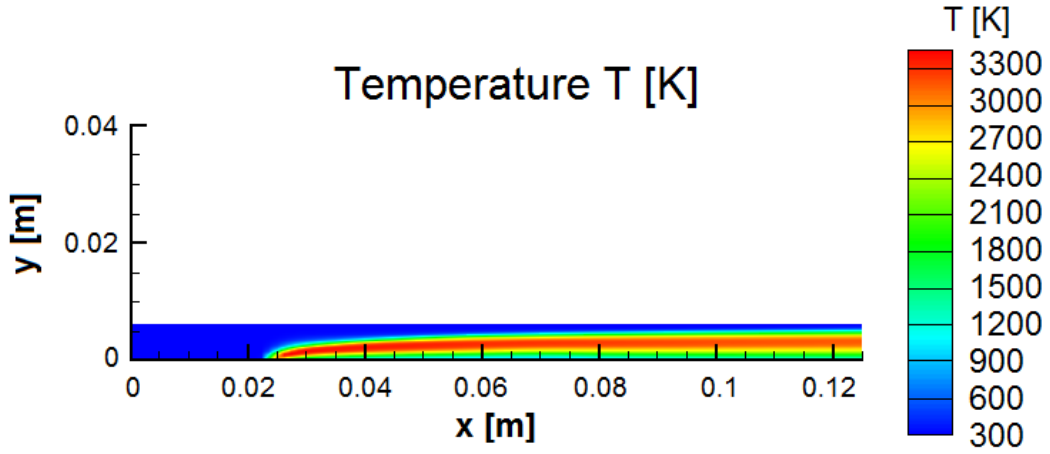

Figure 6.30: Field of temperature T - PaSR. Reacting case, turbulent combustion. Test Model Jones6.

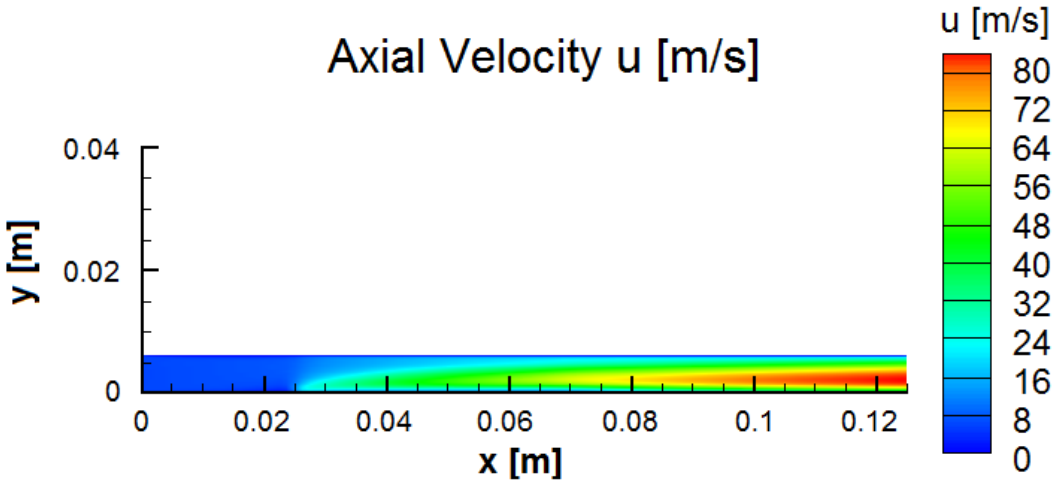

Figure 6.31: Field of axial velocity component u - PaSR. Reacting case, turbulent combustion. Test Model Jones6.

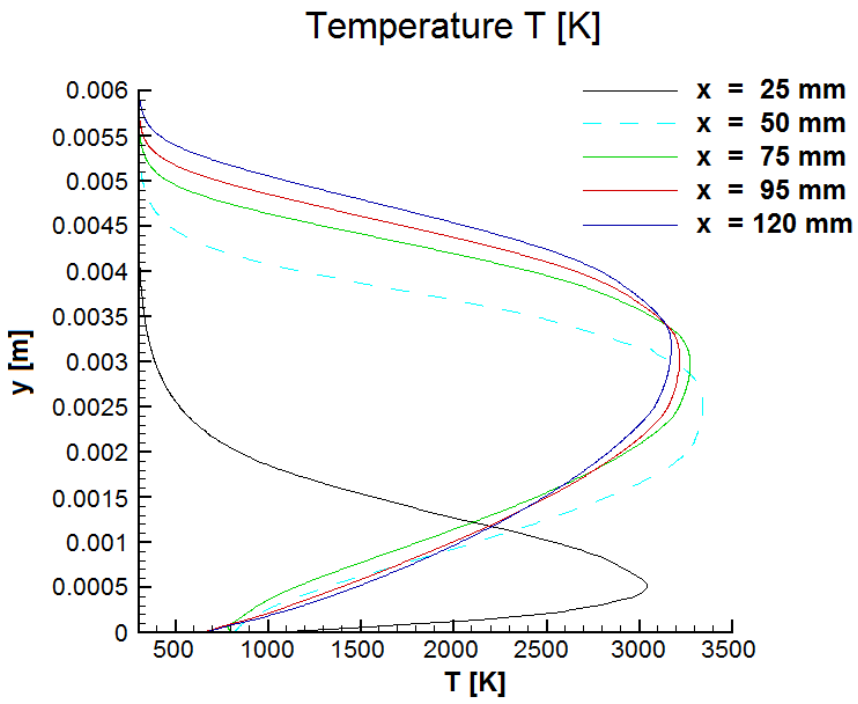

Figure 6.32: Section profiles of temperature T - PaSR. Reacting case, turbulent combustion. Test Model Jones6.

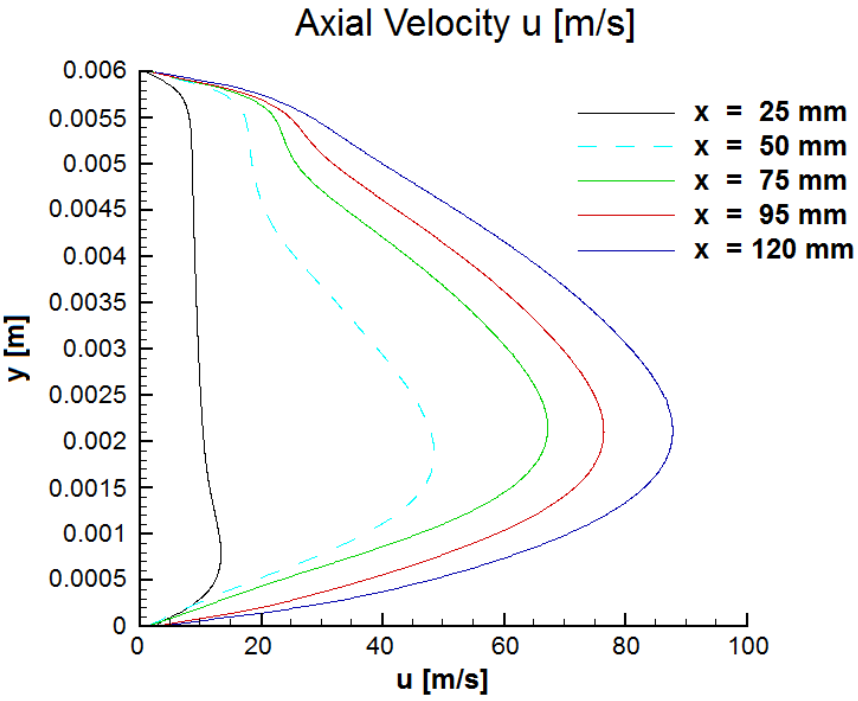

Figure 6.33: Section profiles of axial velocity component u - PaSR. Reacting case, turbulent combustion. Test Model Jones6.

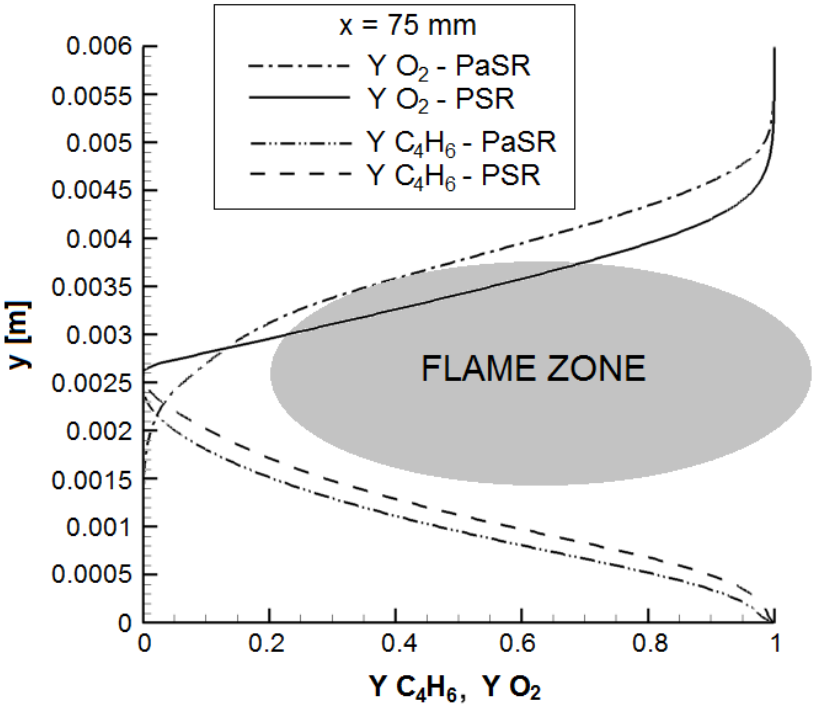

Figure 6.34: Section profiles for O_2 and C_4H_6 mass fractions at x = 75 mm - PSR vs. PaSR comparison. Reacting case, turbulent combustion. Test Model Jones6.

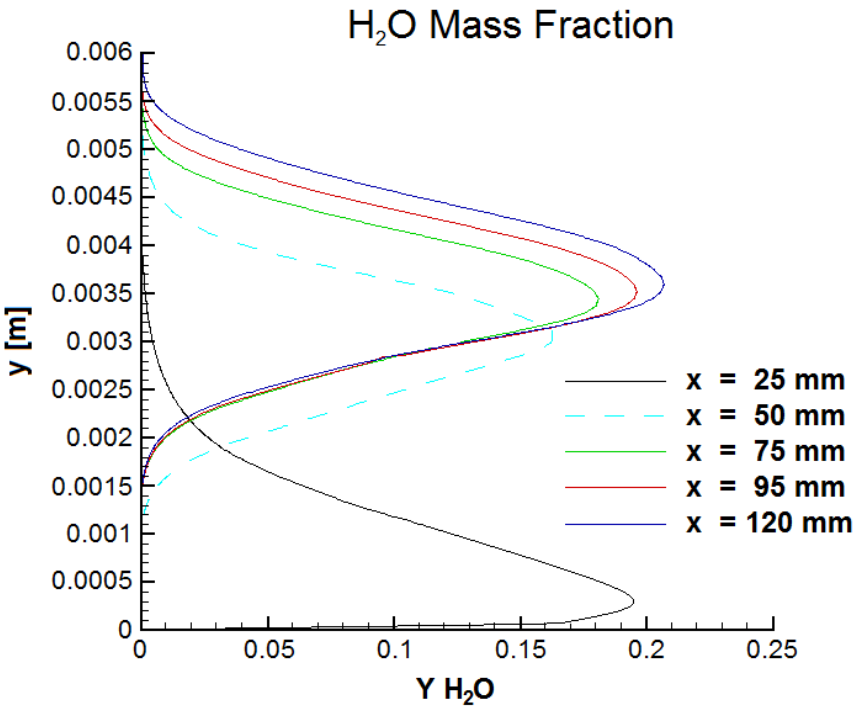

Figure 6.35: Section profiles of H_2O mass fraction - PaSR. Reacting case, turbulent combustion. Test Model Jones6.

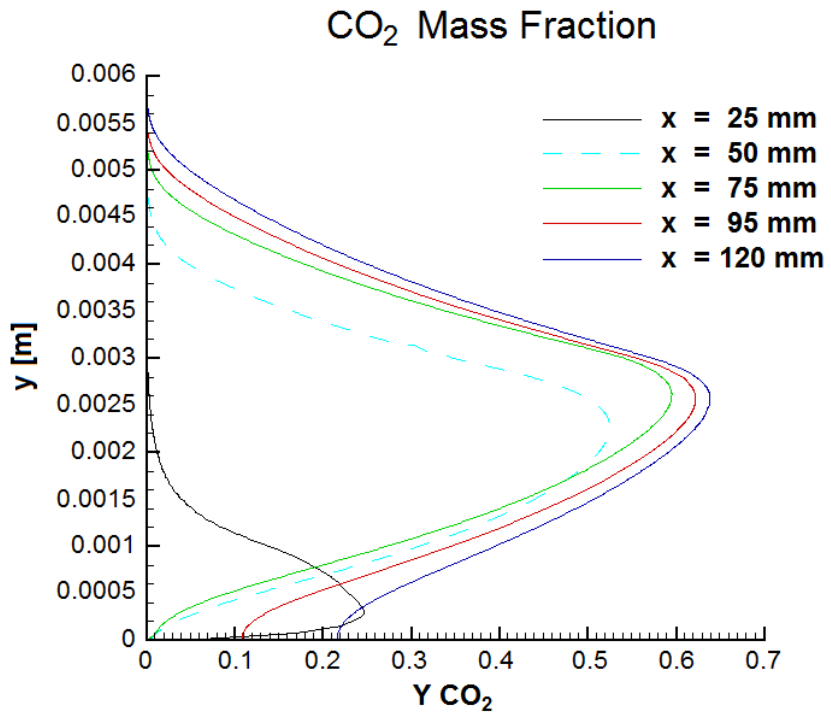

Figure 6.36: Section profiles of CO_2 mass fraction - PaSR. Reacting case, turbulent combustion. Test Model Jones6.

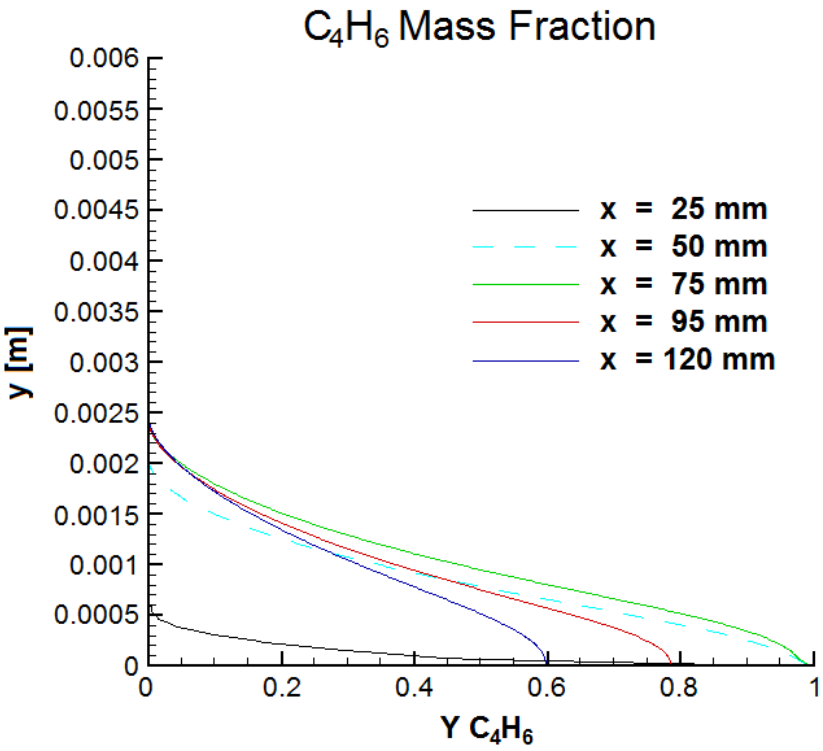

Figure 6.37: Section profiles of C_4H_6 mass fraction - PaSR. Reacting case, turbulent combustion. Test Model Jones6.

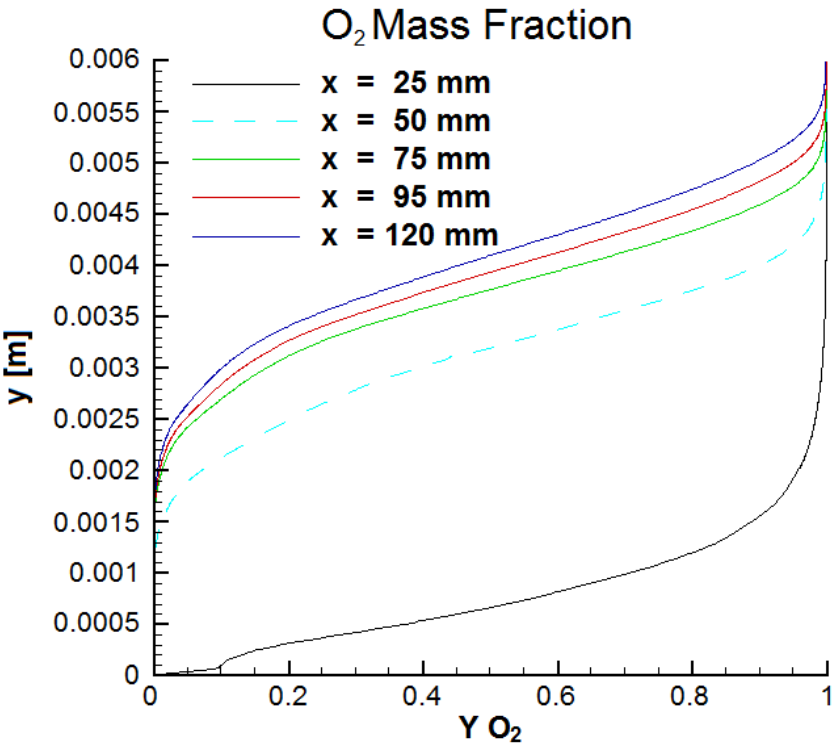

Figure 6.38: Section profiles of O_2 mass fraction - PaSR. Reacting case, turbulent combustion. Test Model Jones6.

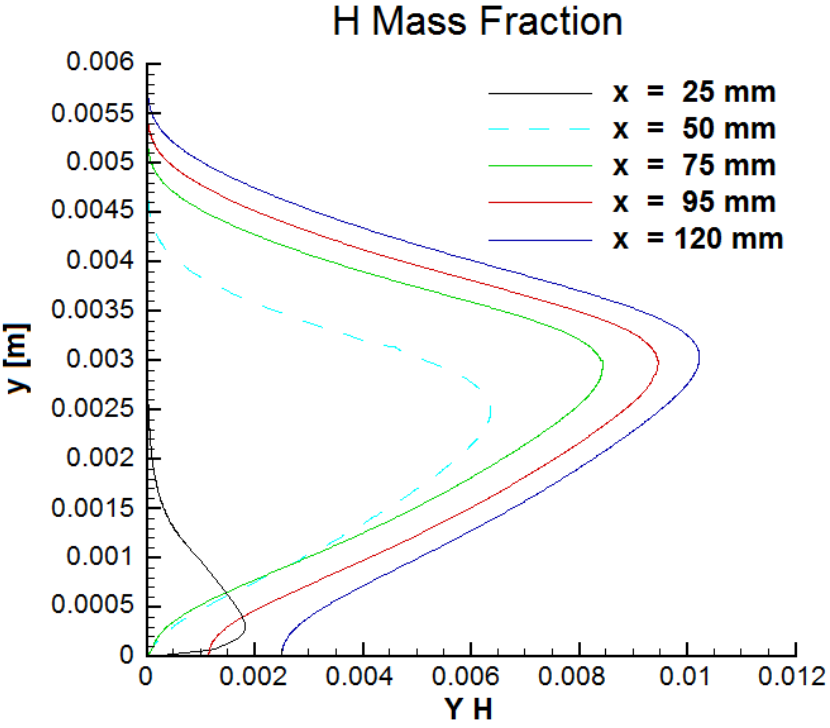

Figure 6.39: Section profiles of H mass fraction - PaSR. Reacting case, turbulent combustion. Test Model Jones6.

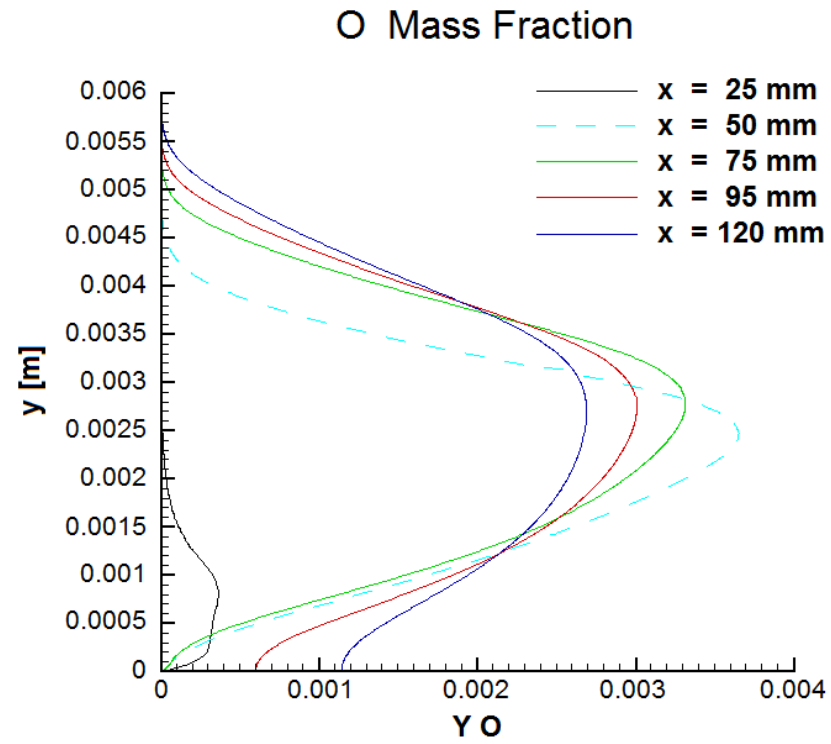

Figure 6.40: Section profiles of O mass fraction - PaSR. Reacting case, turbulent combustion. Test Model Jones6.

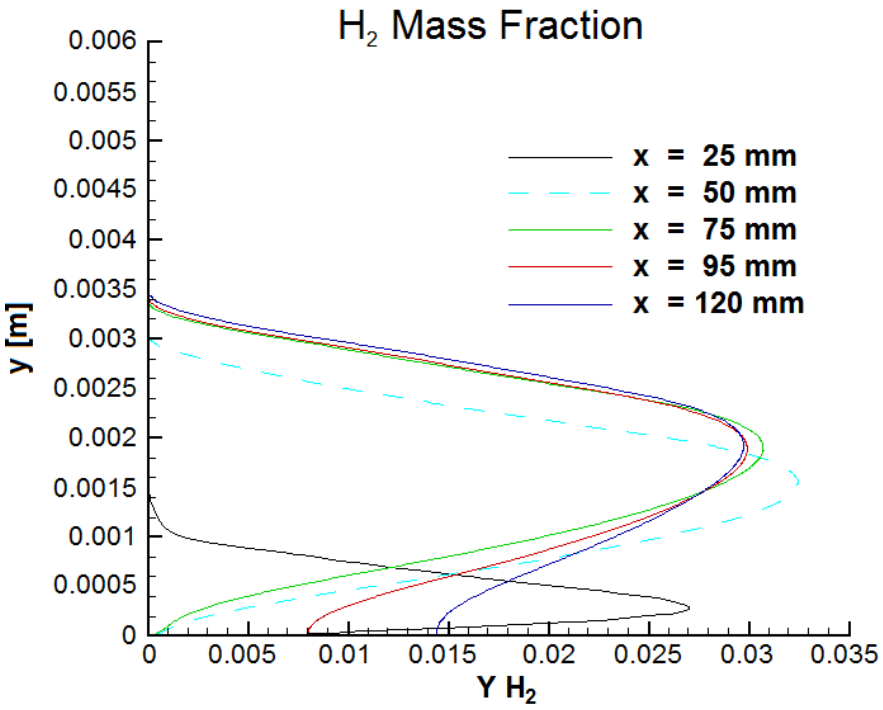

Figure 6.41: Section profiles of H_2 mass fraction - PaSR. Reacting case, turbulent combustion. Test Model Jones6.

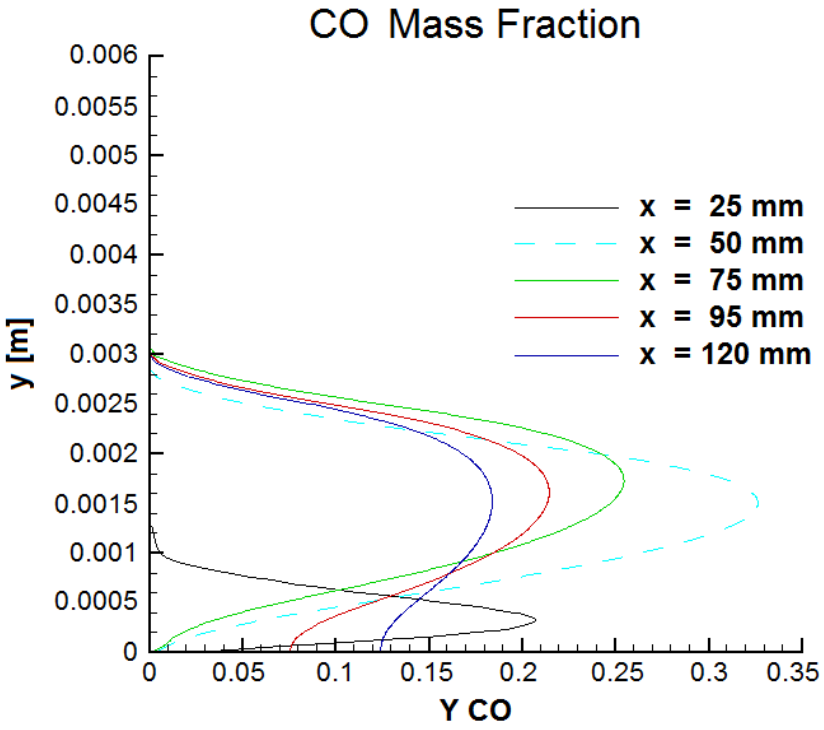

Figure 6.42: Section profiles of CO mass fraction - PaSR. Reacting case, turbulent combustion. Test Model Jones6.

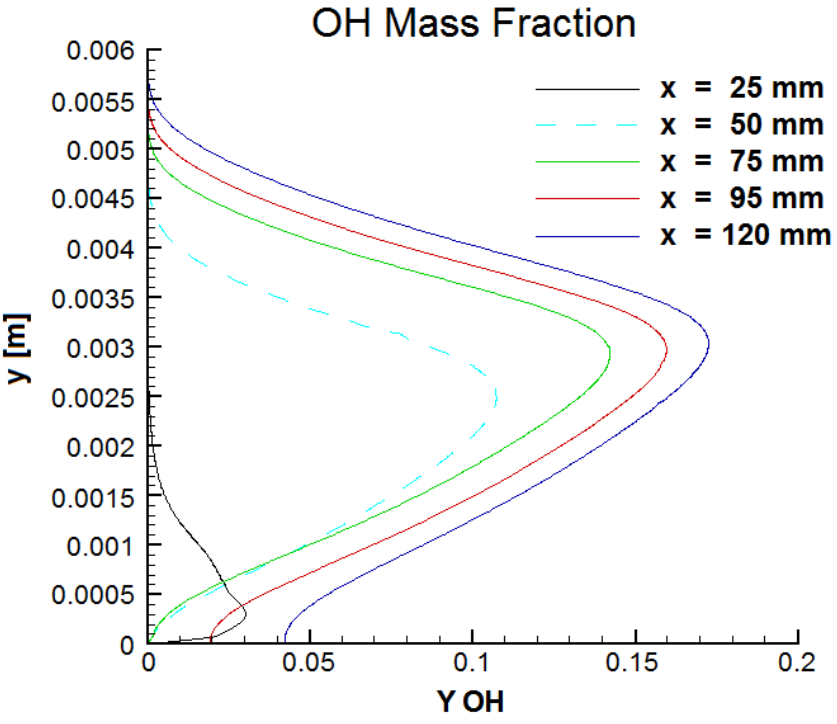

Figure 6.43: Section profiles of OH mass fraction - PaSR. Reacting case, turbulent combustion. Test Model Jones6.

Influence of Inlet Velocity

A parametric study for increasing oxidizer inlet velocity is performed also when PaSR model is used. As for PSR, from the starting speed of 6 m/s for the oxidizer inlet, cases for 10 m/s, 15 m/s and 20 m/s are studied. For these cases fuel inlet velocity is increased accordingly to the increas in oxidizer inlet mass flux. Therefore the values of v_{fuel} are 0.43 m/s, 0.65 m/s and 0.87 m/s corresponding respectively to inlet velocities of 10 m/s, 15 m/s and 20 m/s. Results are introduced in figures 6.44 and 6.45 as temperature and velocity sections at x = 120 mm location (near combustor end). Increased inlet velocity results in increased temperature peak (from 3175 K at 6 m/s inlet speed to 3346 K at 20 m/s inlet speed, at the considered section). A significant increase in the maximum value for axial velocity is also noticeable. The peak velocity for the considered section (near combustor end) increases from 87 m/s for the minimum inlet speed tested to 172 m/s for the maximum speed considered.

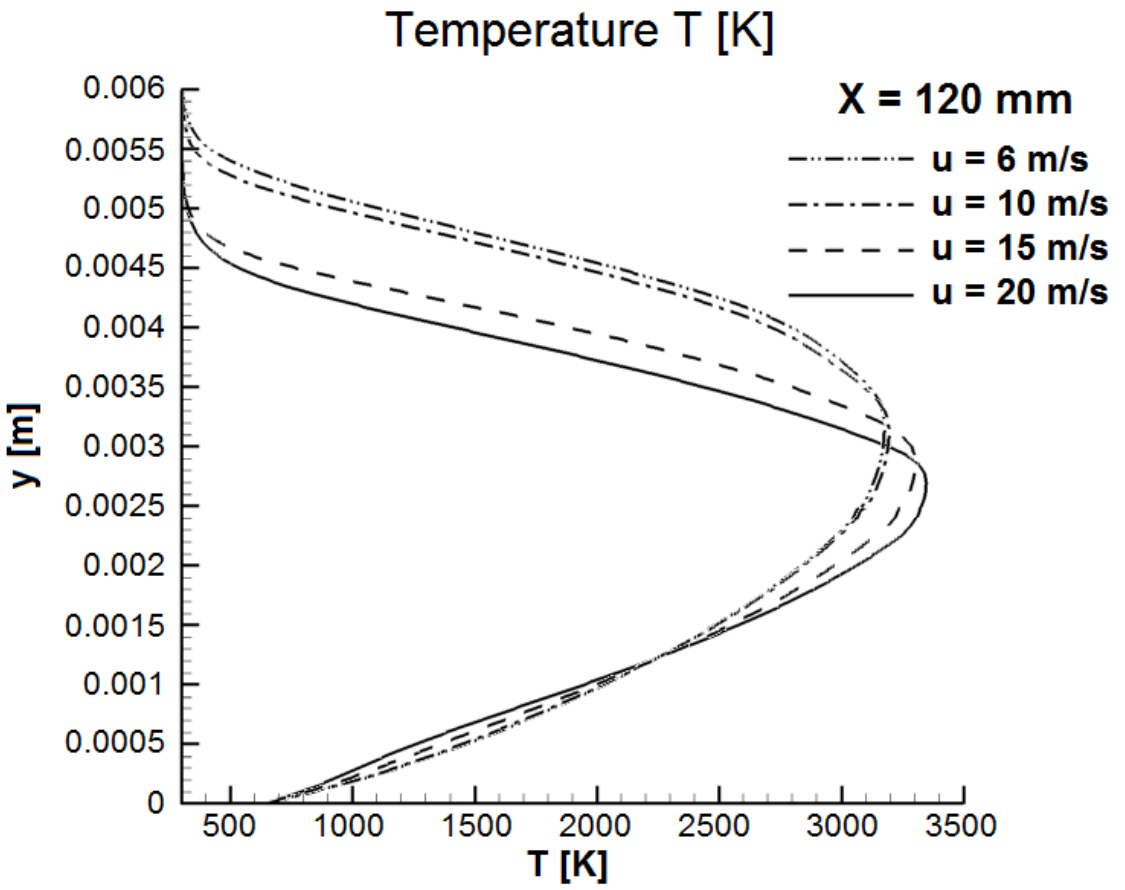

Figure 6.44: Section profiles of temperature with increasing inlet speed - PaSR. Reacting case, turbulent combustion. Test Model Jones6.

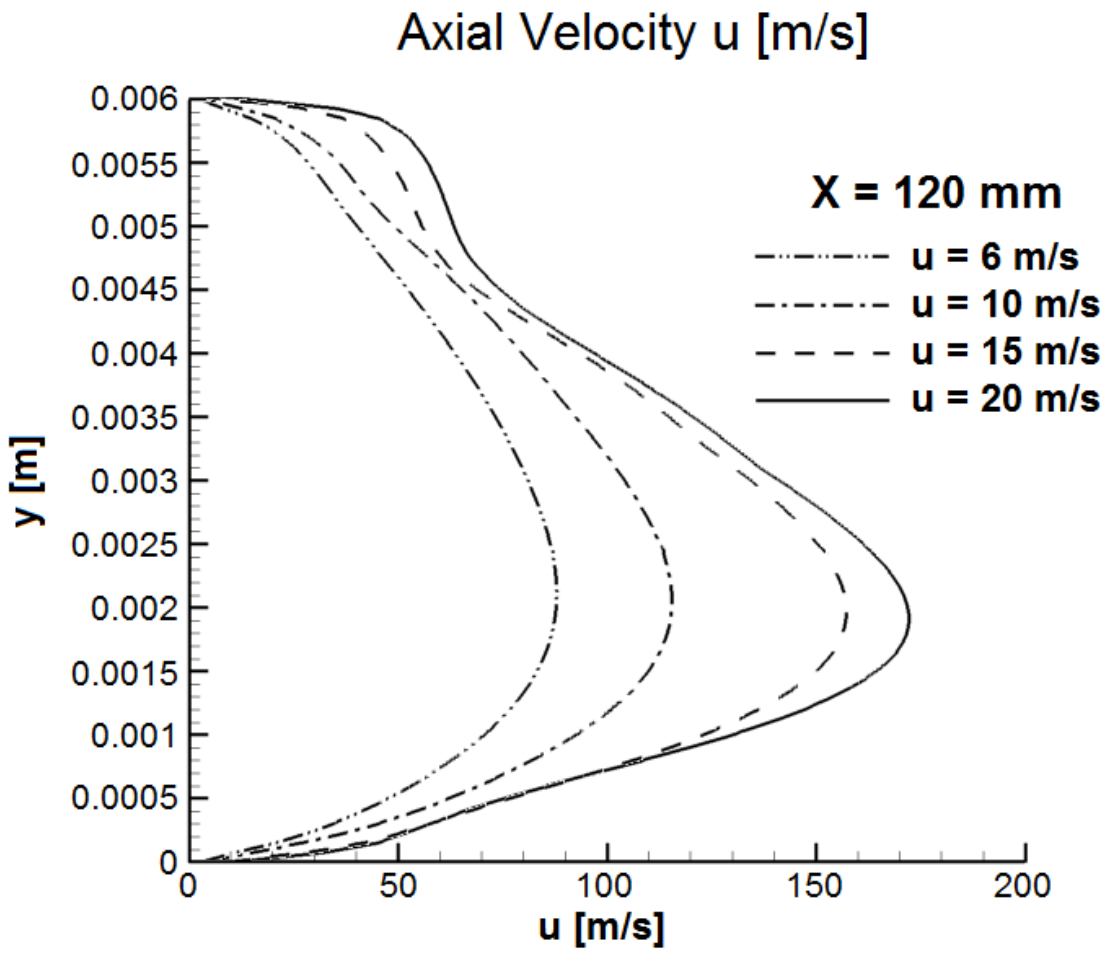

Figure 6.45: Section profiles of axial velocity component u with increasing inlet speed - PaSR. Reacting case, turbulent combustion. Test Model Jones6.

6.5.4 Test Model Jones-Lindstedt 6 - PaSR Model Results, Double Slab

Further studies are performed in a double-slab configuration, in order to compare results from present work and from the work of Merotto [48]. Double-slab cases are significant because this set-up leads to a significant increase in performances on lab-scale tests, as in [100]. Double-slab configuration uses the same geometry as previous testcases but with two symmetric fuel inlet present: one on the lower combustion chamber wall and the other one on the upper wall. For the present case and for comparison with the work [48], fuel inlet speed is imposed as well as fuel inlet temperature, with a value of 1500 K. Figures 6.46 and 6.48 show temperature field and temperature profiles respectively. Being two peak temperature regions instead of one, these are individually narrower than the single peak temperature region present in the single-slab case. The peak temperature is slightly over 3500 K, which is higher than the 3350 K obtained by the single-slab counterpart of this testcase. Therefore, as expected from problem physics, it is possible to say that the interaction of the two flame fronts has a positive effect, enhancing the

combustion process. In fact, looking at figures 6.47 and 6.49, which depict axial velocity field and profile, it is possible to notice a significant increase of speed with respect to the single-slab case. For the same oxidizer inlet speed of 6 m/s, single-slab case shows a peak velocity of 80 m/s, while double slab-case has a peak velocity over 130 m/s. In order to obtain a peak velocity of 130 m/s in a single-slab configuration, as shown in the previous section about the influence of inlet speed, the required inlet speed is between 10 m/s and 15 m/s. Therefore this numerical results are coherent with the performance enhancing capabilities of double-slab configurations. Figures from 6.50 to 6.58 show the profiles of reactants and products mass fractions. Noticeably chemical species distribution is coherent with peak temperature regions. The presence of two peak temperature regions is reflected in the chemical species distribution, which show this same behavior. The difference in products mass fraction with respect to single-slab case can be ascribed to the difference in the area of the peak temperature reagion and in the peak temperature value.

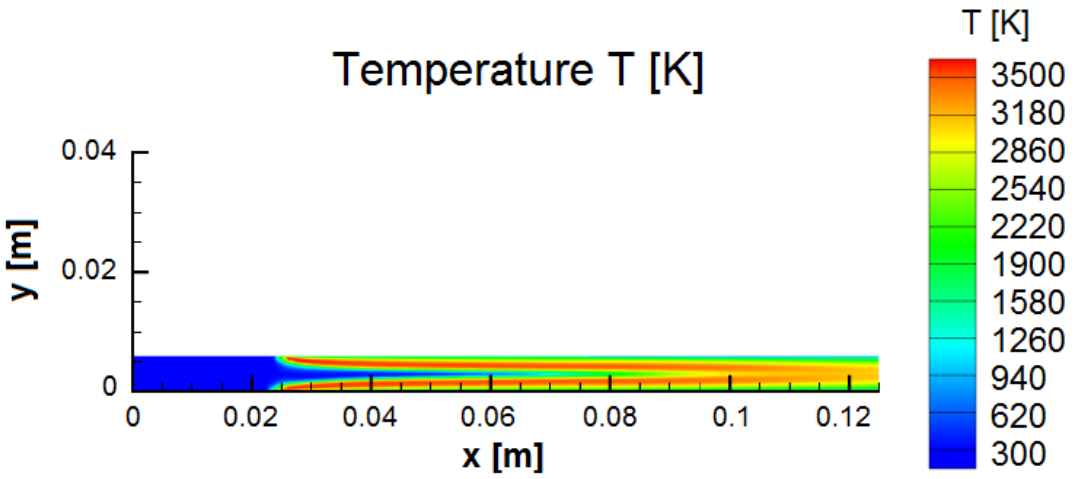

Figure 6.46: Field of temperature T - PaSR. Reacting case, turbulent combustion. Test Model Jones6. Double slab.

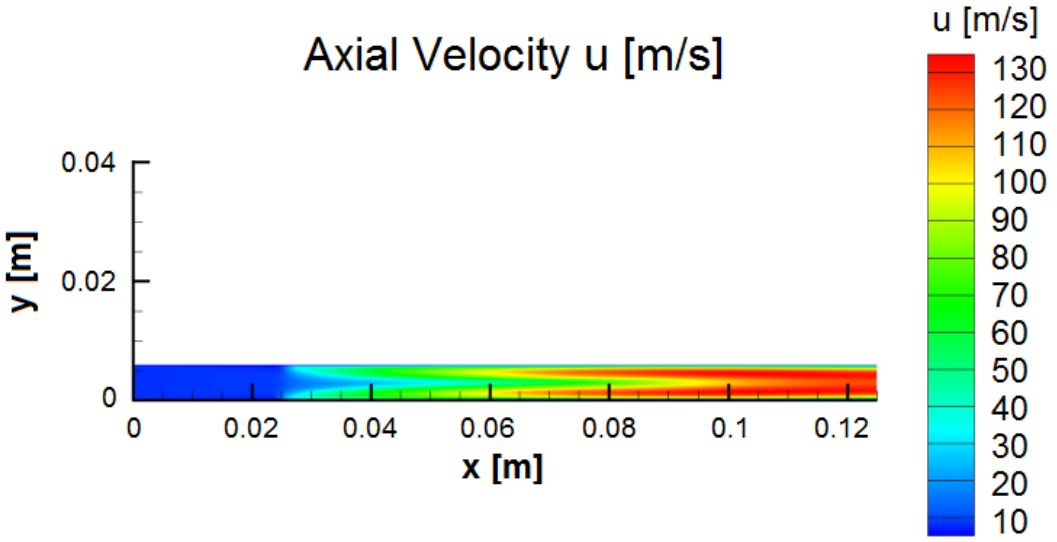

Figure 6.47: Field of axial velocity component u - PaSR. Reacting case, turbulent combustion. Test Model Jones6. Double slab.

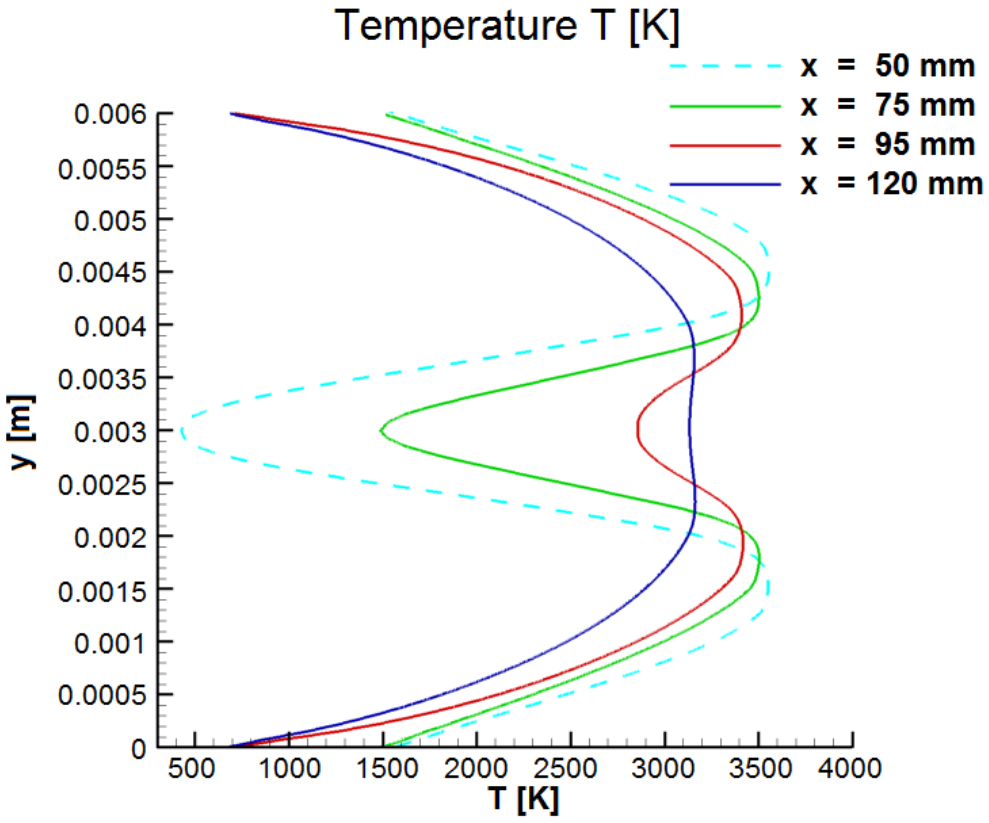

Figure 6.48: Section profiles of temperature T - PaSR. Reacting case, turbulent combustion. Test Model Jones6. Double slab.

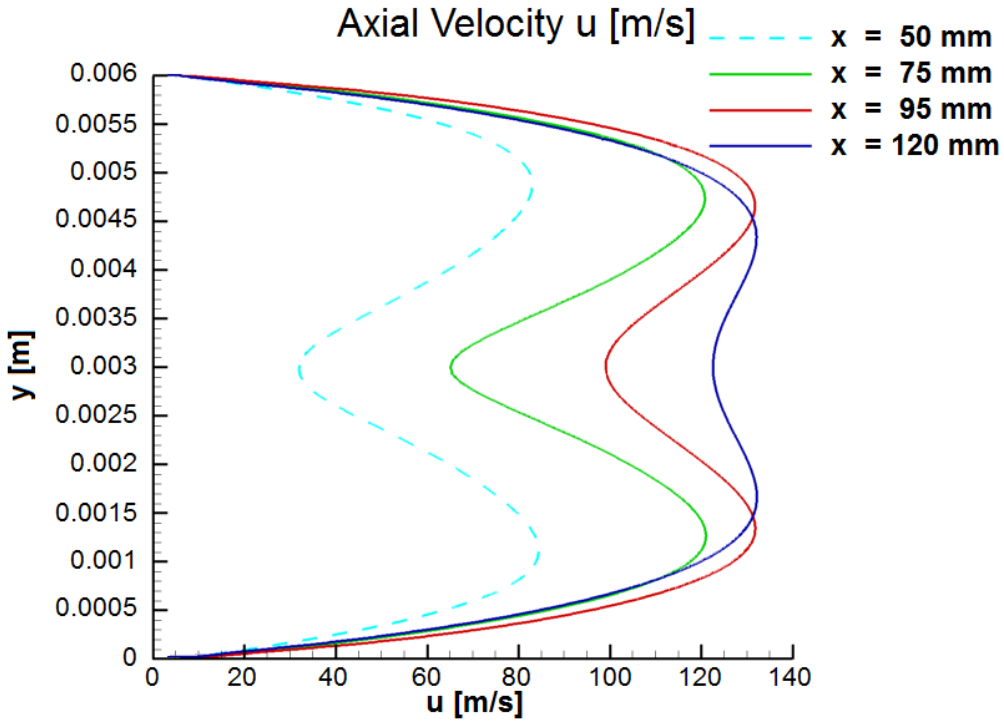

Figure 6.49: Section profiles of axial velocity component u - PaSR. Reacting case, turbulent combustion. Test Model Jones6. Double slab.

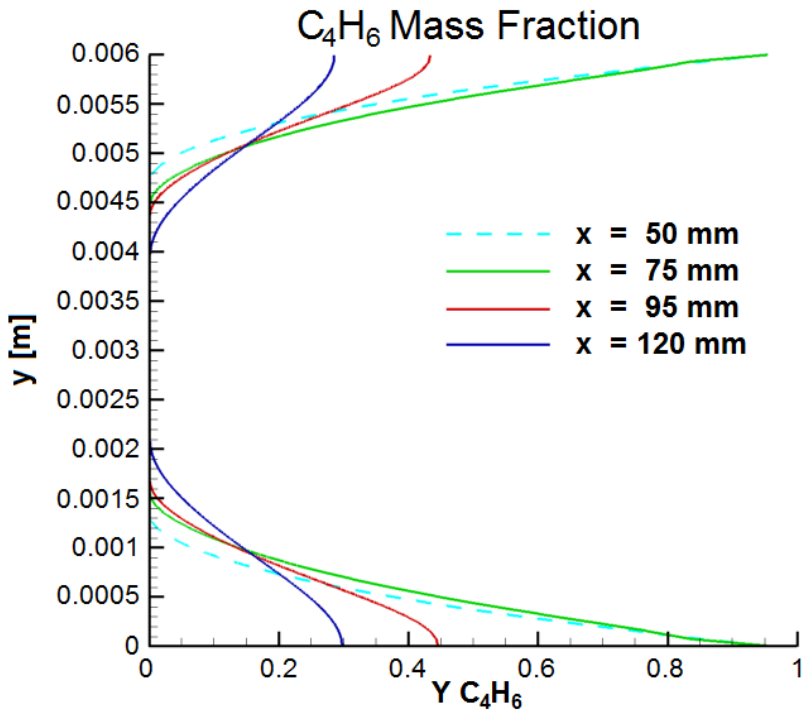

Figure 6.50: Section profiles of C_4H_6 mass fraction - PaSR. Reacting case, turbulent combustion. Test Model Jones6. Double slab.

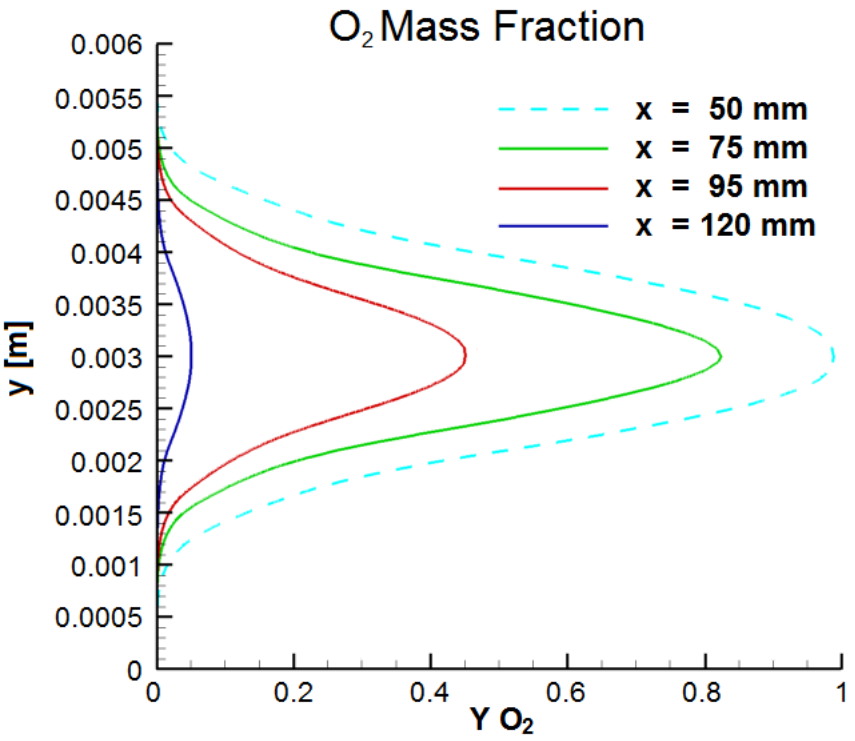

Figure 6.51: Section profiles of O_2 mass fraction - PaSR. Reacting case, turbulent combustion. Test Model Jones6. Double slab.

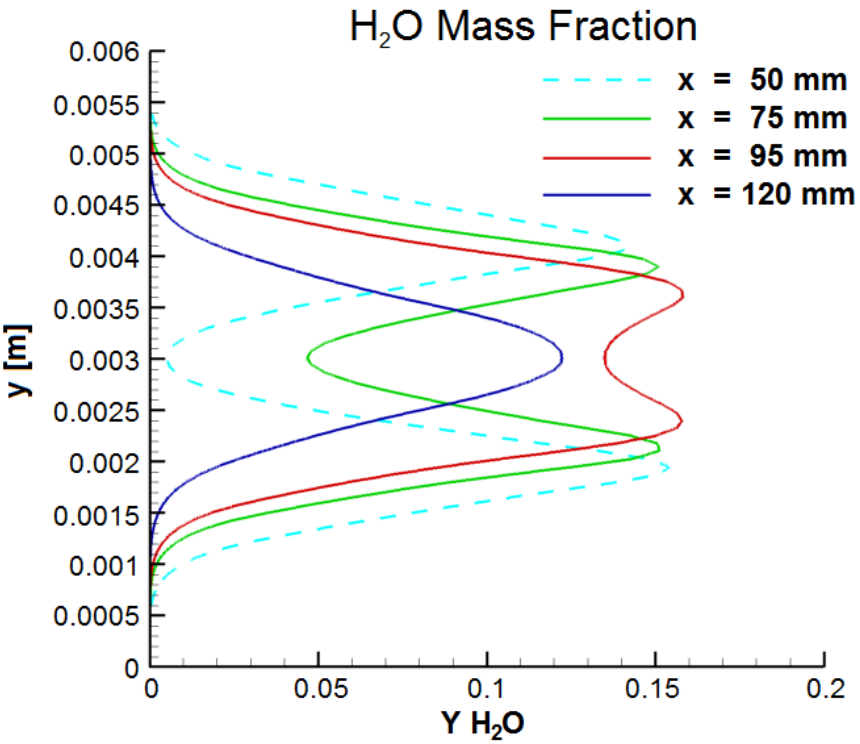

Figure 6.52: Section profiles of H_2O mass fraction - PaSR. Reacting case, turbulent combustion. Test Model Jones6. Double slab.

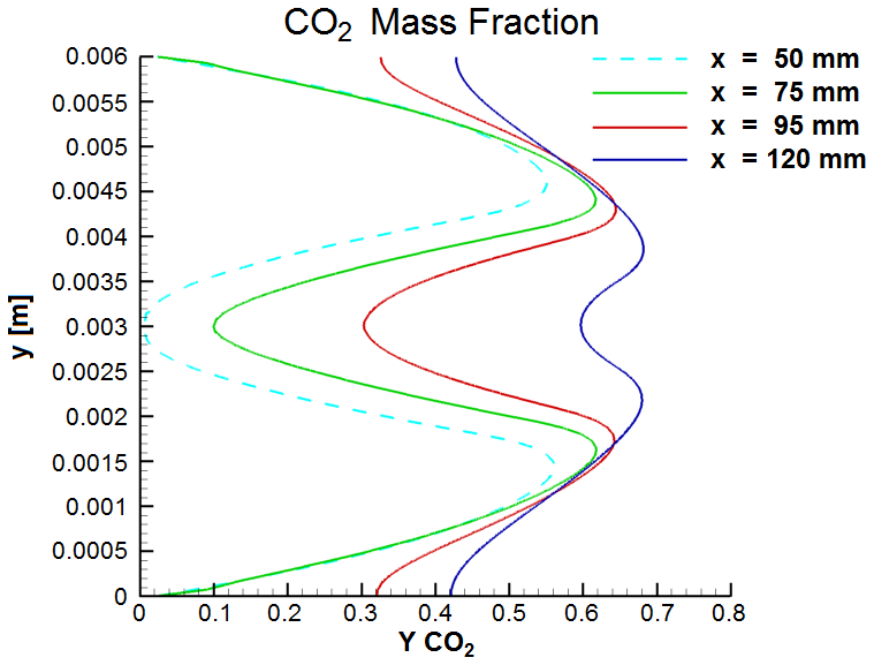

Figure 6.53: Section profiles of CO_2 mass fraction - PaSR. Reacting case, turbulent combustion. Test Model Jones6. Double slab.

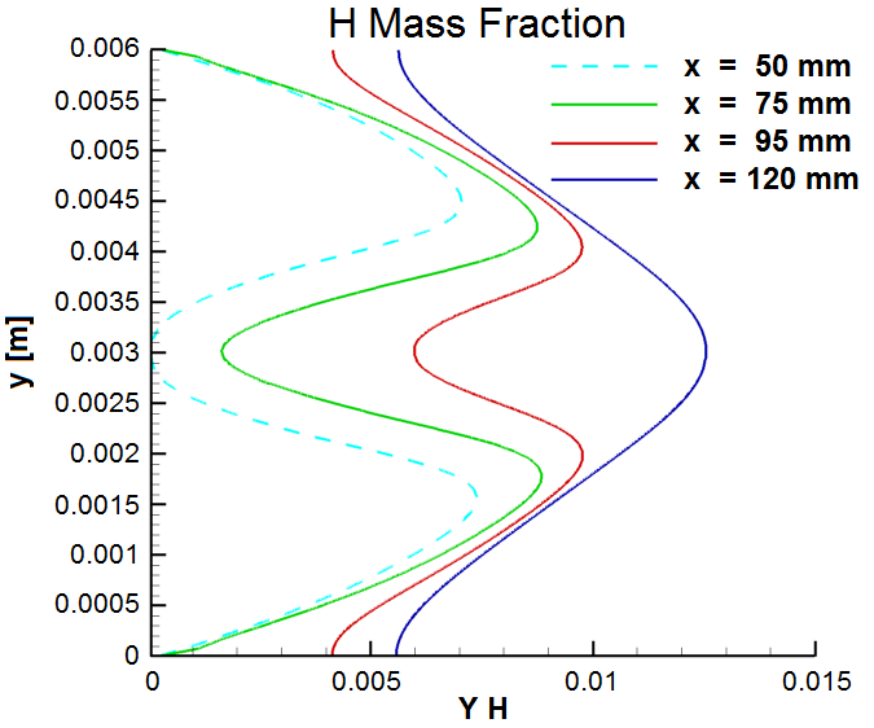

Figure 6.54: Section profiles of H mass fraction - PaSR. Reacting case, turbulent combustion. Test Model Jones6. Double slab.

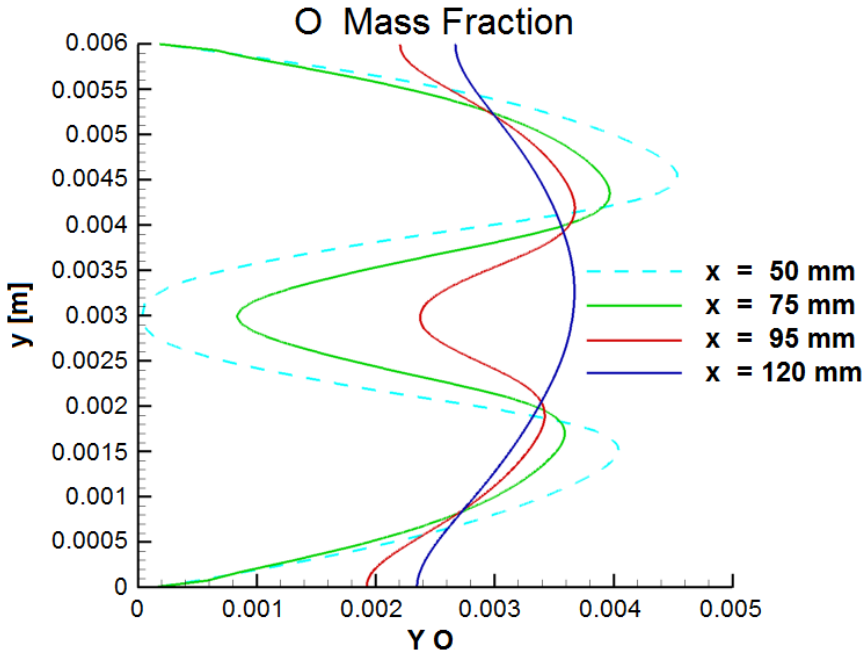

Figure 6.55: Section profiles of O mass fraction - PaSR. Reacting case, turbulent combustion. Test Model Jones6. Double slab.

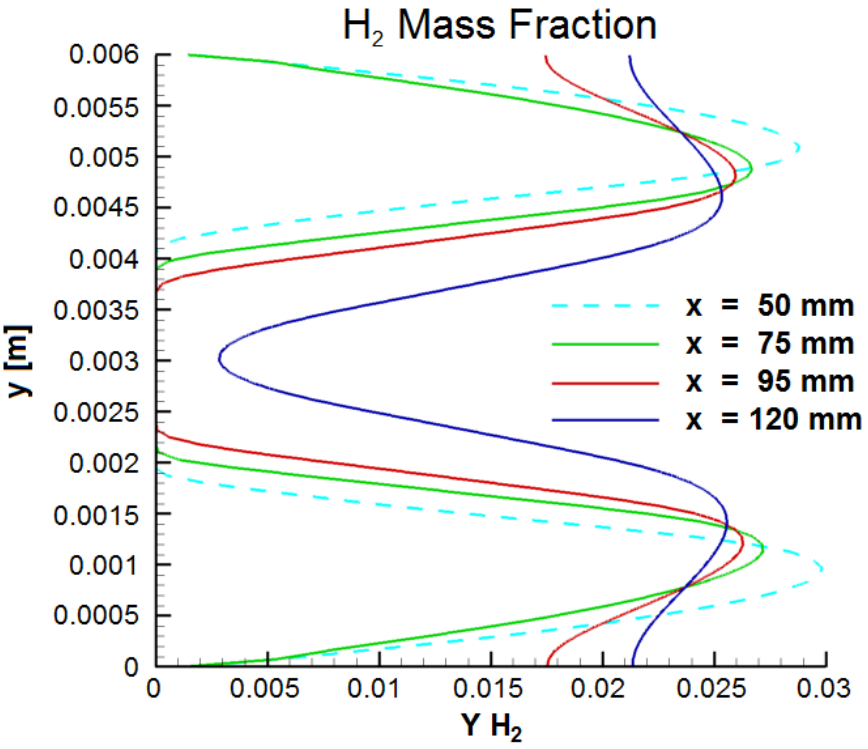

Figure 6.56: Section profiles of H_2 mass fraction - PaSR. Reacting case, turbulent combustion. Test Model Jones6. Double slab.

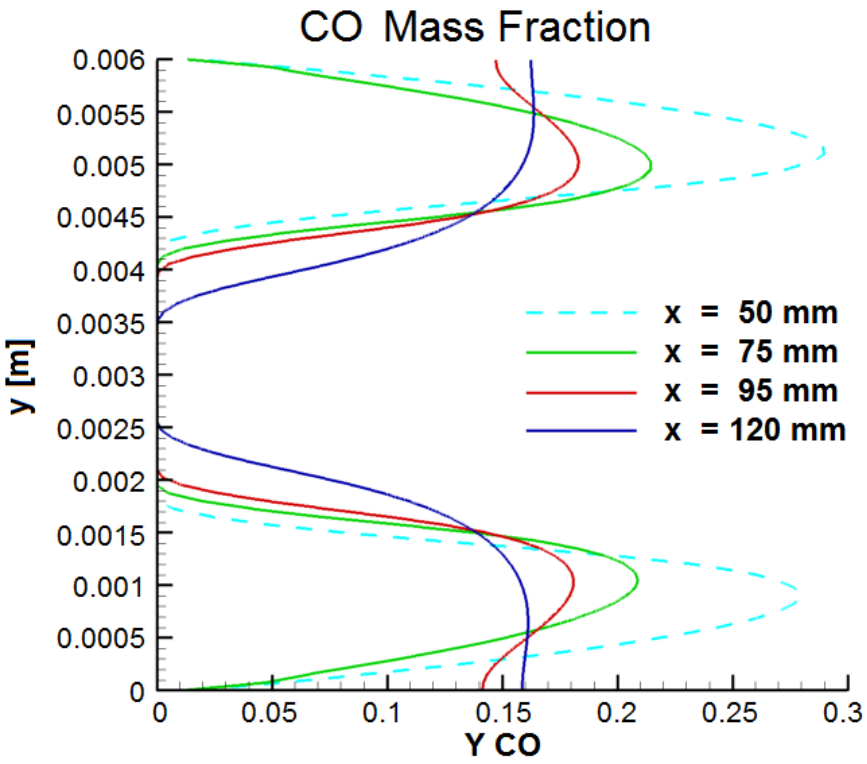

Figure 6.57: Section profiles of CO mass fraction - PaSR. Reacting case, turbulent combustion. Test Model Jones6. Double slab.

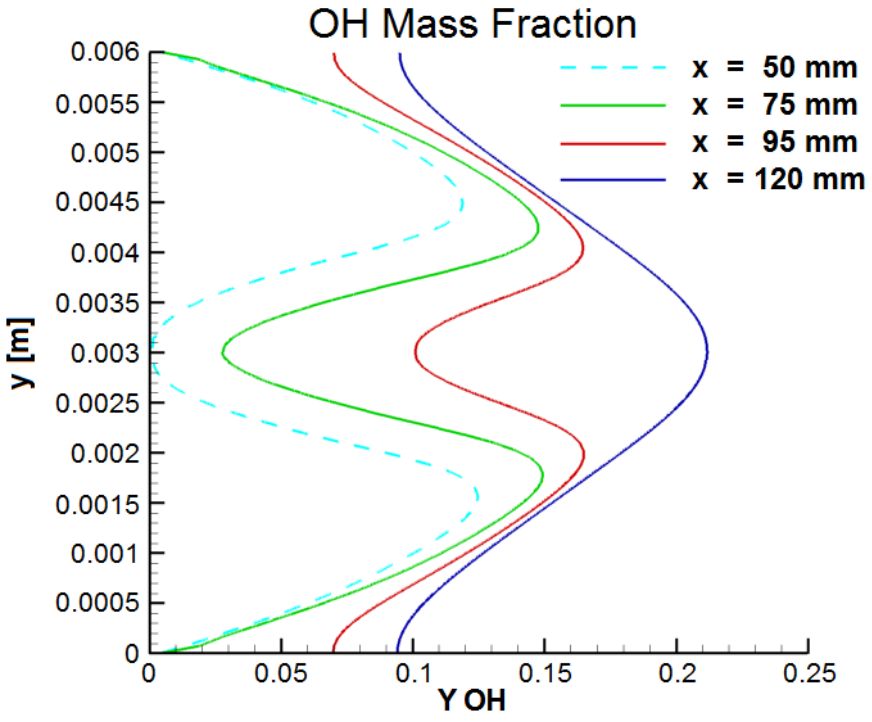

Figure 6.58: Section profiles of OH mass fraction - PaSR. Reacting case, turbulent combustion. Test Model Jones6. Double slab.

6.6 Influence of Pressure

The purpose of the present section is to address the effects of pressure over both the flow field and the regression rate of hybrid rockets. It is imporant to understand that the determination of an overall behavior of the combustion in hybrid rockets under the effects of different pressure conditions is still an open question in the research community. Of particular importance is the trend of regression rate at different pressure conditions. In general, for standard operating conditions of hybrid rockets, regression rate is considered to be little or not affected by pressure, as stated by Karabeyoglu during the last EUCASS conference [24]. On the other side, fundamental work from Smoot and Price [115] describes a complex behavior of regression rate based on three different oxidizer mass flux conditions (low, intermediate and high) and three pressure regimes (low, medium and high). The work from Smoot and Price shows that the pressure effect on regression rate is negligible at low oxidizer mass flux and it is increasingly stronger with increasing oxidizer mass flux. For high mass fluxes the regression rate should increase with pressure, as shown in figure 6.59. More recent works from Yash et al. [116] also show an increase in regression rate with pressure. On the other hand likewise fundamental work of Risha, Kuo et al. [117] shows a decrease in regression rate with increasing operating pressure.

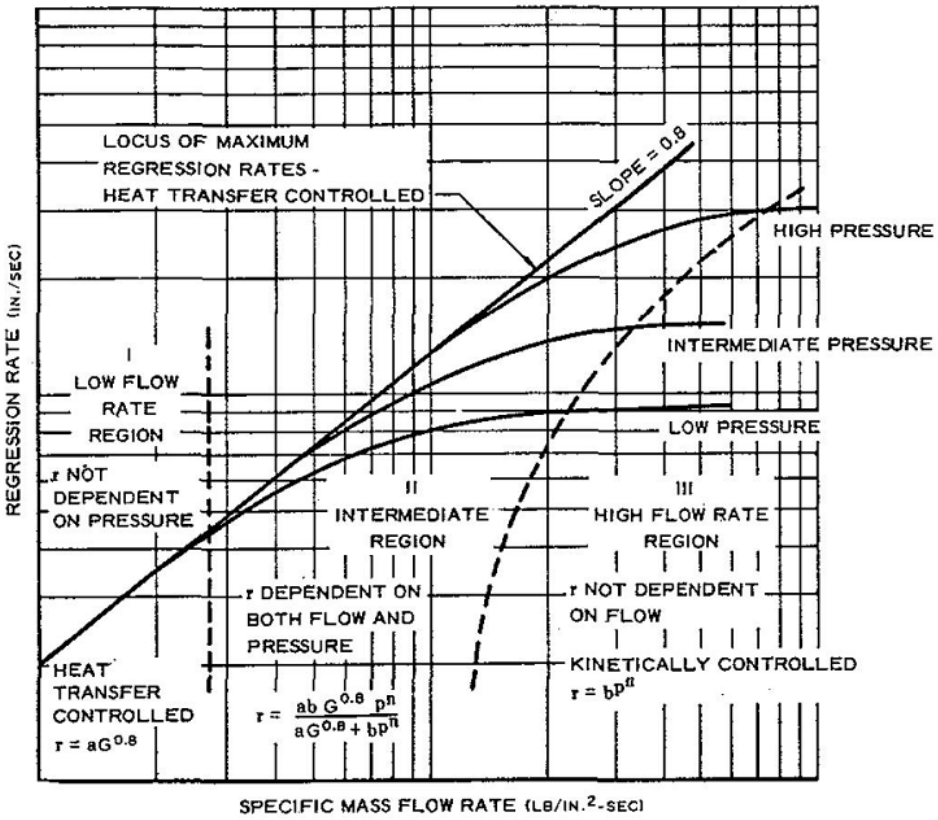

Figure 6.59: Effects of oxidizer mass flux and pressure on regression rate, by [115].

Of course the effects of pressure on regression rate are also strictly correlated to the

effects of pressure on the flow field. Therefore in this section some comparison results are shown in order to assess the variations on temperature, axial velocity and mass fractions due to increasing pressure. Table 6.60 summarizes the numerical testcases performed:

Pressure [bar]	1			2,5	5	10
Source Term	PSR*	PaSR	PaSR	PaSR	PaSR	PaSR
Diffusion of Enthalpy at Fuel Surface	No	No	Yes	Yes	Yes	Yes
Oxidizer Inlet Velocity [m/s] / Oxidizer Mass Flux [kg/m²s]	6 / 7,8	6 / 7,8	6 / 7,8	6 / 19.5	3 / 19.5	3 / 39
	10 / 13	10 / 13	10 / 13	12 / 39	6 / 39	6 / 78
	15 / 19.5	15 / 19.5	15 / 19.5	16 / 52	10 / 65	10 / 130
	20 / 26	20 / 26	20 / 26	20 / 65	15 / 97.5	15 / 195
	-	25 / 32,5	25 / 32,5	-	-	-
	-	30 / 39	30 / 39	-	-	-
	-	35 / 45,5	35 / 45,5	-	-	-
	-	40 / 52	40 / 52	-	-	-

* PSR test is considered as code functionality test

Figure 6.60: Testcases for varying oxidizer inlet speed/mass flux and pressure conditions.

In the present and in the next section, the most significant results obtained are presented. As shown in table 6.60, first tests are made in the simplest possible conditions (PSR approach and negligible diffusion of enthalpy at fuel surface): this test in particular is considered to be a code-functionality test, being overcome by more accurate tests with a fully turbulent source term. An important preliminary consideration has to be done about the role of wall heat flux contribution from the species enthalpy transported by diffusion. Two approaches are found in literature:

- wall heat flux contribution from diffusion of species enthalpy as described in equation (5.24) with the term $\sum_{i=1}^{NS} h_i \boldsymbol{J}_{i,g} \cdot \boldsymbol{n}_g$ is considered negligible, such as in [120];
- wall heat flux contribution from diffusion of species enthalpy is considered not negligible, such as in [44];

The choice for present work is to implement both conditions in order to verify the contribution of this enthalpy diffusion term at wall, especially on mean regression rate, which

are shown in the next section. It is important to consider, however, that the presence of enthalpy transported by diffusion is an accurate model of the physical phenomena involved on fuel pyrolisis. Therefore the results of the effect of pressure on fluid field quantities presented in this section consider both the PaSR approach and the diffusion of enthalpy at fuel surface. Figures 6.61 to 6.71 show a significant comparison at near combustor end section for an oxidizer mass flux of $39\,kg/m^2s$, which correspond to a Reynolds number $Re_h = 11700$, where $h = 6\,mm$ is the height of the slab channel. Figure 6.61 shows the comparison of temperature section profiles. Noticeably the peak temperature decreases significantly with pressure at the considered section: moving from 1 bar to 2.5 bar reduces the peak temperature of nearly 200 K, from 3400 K to 3200 K. Again, increasing the pressure from 2.5 bar to 5 bar decreases the peak tempearature of another 200 K, from 3200 K to nearly 3000 K. Another increase in pressure, from 5 bar to 10 bar, reduces the peak temperature once again of 200 K, from 3000 K to nearly 2800 K. It is possible to notice that increasing the pressure shows a general trend in reducing the size of the hot gases zone. It is important to remember that all the results are obtained under the ideal gas hypothesis $p = \rho R_{mix} T$ (which correlates pressure, density, temperature and gas composition) in turbulent reacting conditions. This means that pressure has an effect on density, but density is related to reaction rates through the species concentrations: higher densities correspond to higher concentrations and therefore, in general, to a faster chemistry. In addition the density and the properties of the gas mixture are obviously dependant on its composition. These results suggest that doubling the pressure reduces the peak temperature of nearly 6%–7%. This could be explained by this effect of pressure on concentrations and therefore on the chemical reactions. In fact, looking at the products composition, it is noticeable an increase in H_2O and in H_2 species, a decrease in O and an increase in OH dissociated products. This could be explain considering the six reaction scheme shown in table 3.2: reactions 1) and 2) are unbalanced toward their products by an increase in pressure; this produces an increase in availabilità of reactants for equation 4), therefore the increase in H_2O; an increased presence of H_2O increases the kinetics of reaction 6), reaction which absorbs a significant amount of heat. These considerations, previously than any quantitative consideration about regression rate, are in the direction of a reduction of regression rate with increasing pressure for the considered combustor section. Figure 6.62 shows the trend in axial velocity in the combustion chamber with increasing pressure at the considered section, oxidizer mass flux and Reynolds number. It is possible to notice that the absolute valute of peak axial velocity is greatly reduced by the increasing pressure. Peak values are near $228\,m/s$ for 1 bar, $95\,m/s$ for 2.5 bar, $38\,m/s$ for 5 bar and $22\,m/s$ for 10 bar. Oxidizer mass flux and therefore Reynolds number are the same in all the cases, but it is important to notice that oxidizer inlet axial velocity is very different: as shown in figure 6.60, it is $30\,m/s$ for 1 bar, $12\,m/s$ for 2.5 bar, $6\,m/s$ for 5 bar and $3\,m/s$ for 10 bar. However considering the ratio between oxidizer inlet velocity and peak velocity at considered section, it is possible to notice that the increase in axial speed is in the range 7.1 ± 0.8 times, which makes the velocity increase of each case in

good accord with the others. The shape of the curves is also in good accord with the problem physics, where hot gases are accelerated by the presence of a flame in the mid-lower region of the channel. Figures 6.63 and 6.64 show the section profiles respectively of fuel and oxidizer species: C_4H_6 and O_2. The general trend of the curves is similar in both cases and in accord with problem physics. As a general trend, the behavior of 1, 5 and 10 bar cases is closer for both oxidizer and fuel species, with a variation of mass fraction for the same channel height approximatively of 2% for fuel and oxidizer (the latter in the lower half of the channel for the 10 bar case). The 2.5 bar case shows a larger distance from the other cases, with a fuel mass fraction which is lower of a nearly 5–7%. Noticeably, the 10 bar case shows a behavior which is closer to the 2.5 bar case for regions which are farther than the flame. Figure 6.65 shows the section profile for H_2O mass fraction. The peak fraction of this species increases with pressure, therefore higher pressure seems to increase the prodution of H_2O. Figure 6.66 shows the mass fraction of carbon dioxide CO_2. This species shows a little variation in its mass fraction with pressure, with a peak at 1 bar. Figures 6.67 and 6.68 show the mass fractions of the dissociation products O and O. Higher pressures seems to increase the formation of atomic hydrogen H, while on the contrary, the formation of atomic oxygen is greatly enhanced at lower pressures: at 1 bar the peak mass fraction of O is nearly 2.5 times the peak mass fraction at the other investigated pressures. Molecular hydrogen H_2 mass fraction sections are shown in figure 6.69. In this case the pressure seems to affect positively the formation of this species, with a minimum at 1 bar and a maximum which is very close for all the 2.5, 5 and 10 bar cases. A similar behaviour is noticeable for OH dissociated species, depicted in figure 6.70, but the peaks are more evenly spaced with increasing pressure. The last figure 6.70 shows the carbon monoxide CO mass fraction section profile. In this case there is a reduced dependance on pressure, with a non-linear behavior for the peak. The minimum value is found for 2.5 and 10 bar, which is nearly 13%. Then the mass fraction peak increases for 1 bar and has a top value for 5 bar. All these peaks are very close and in the interval 13%–15%. As described in previous section, also in the presence of a pressure increase, the results are coherent with the chemical model and the problem physics. Not only reaction antagonists (such as H_2O and CO_2) are (especially the mass fraction distributions) are present in separate regions of the combustion chamber, but also it is possible to recognize two main regions where different reactions are dominant. Above the channel half-height (0.003 m), reactions 1, 3 and 4 from table 3.2 are more important. On the other hand, in the lower part of the cannel (below 0.003 m), an increased H_2 mass fraction suggest that reactions 1, 2 and 3 from 3.2 are more important.

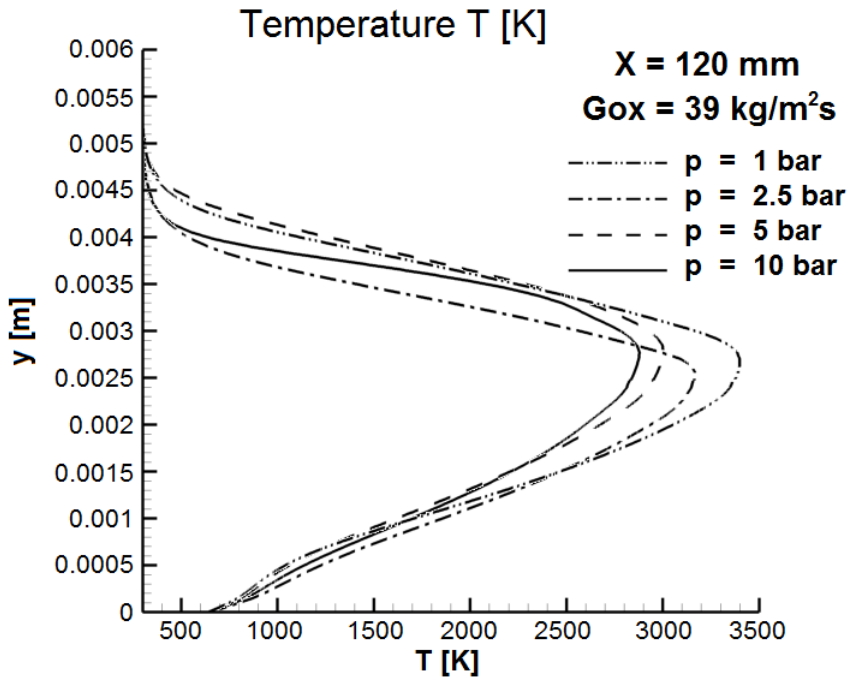

Figure 6.61: Section profiles of T temperature - PaSR, with diffusion of enthalpy; $x = 120mm$, $G_{Ox} = 39kg/m^2s$, $Re_h = 11700$. Single slab.

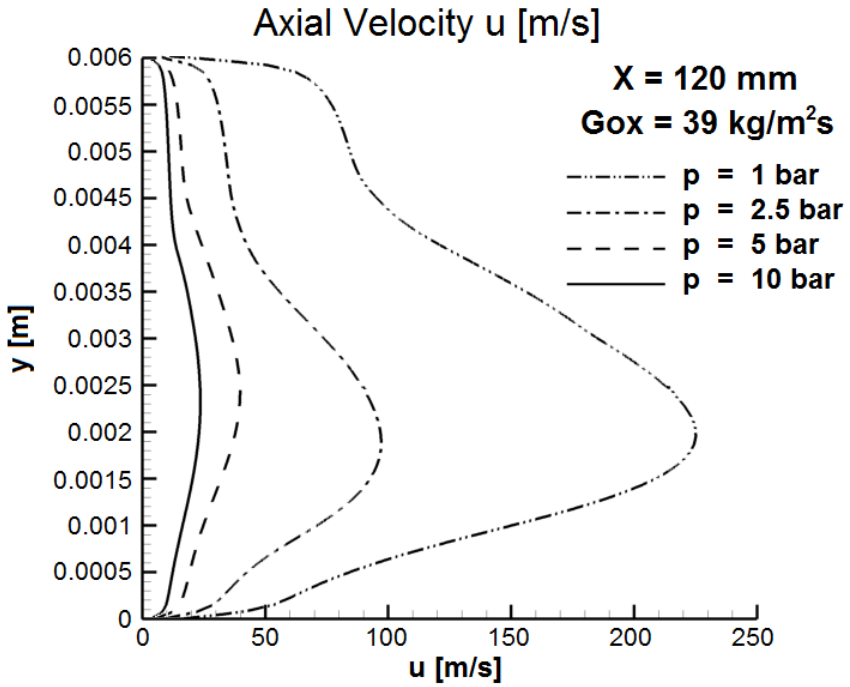

Figure 6.62: Section profiles of U axial velocity - PaSR, with diffusion of enthalpy; $x = 120mm$, $G_{Ox} = 39kg/m^2s$, $Re_h = 11700$. Single slab.

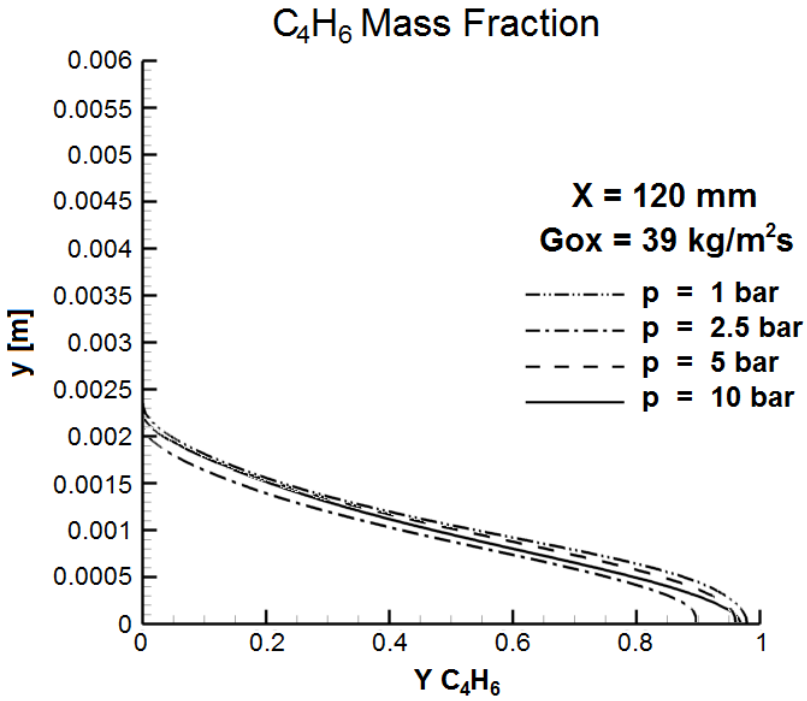

Figure 6.63: Section profiles of C_4H_6 mass fraction - PaSR, with diffusion of enthalpy; $x = 120mm$, $G_{Ox} = 39kg/m^2s$, $Re_h = 11700$. Single slab.

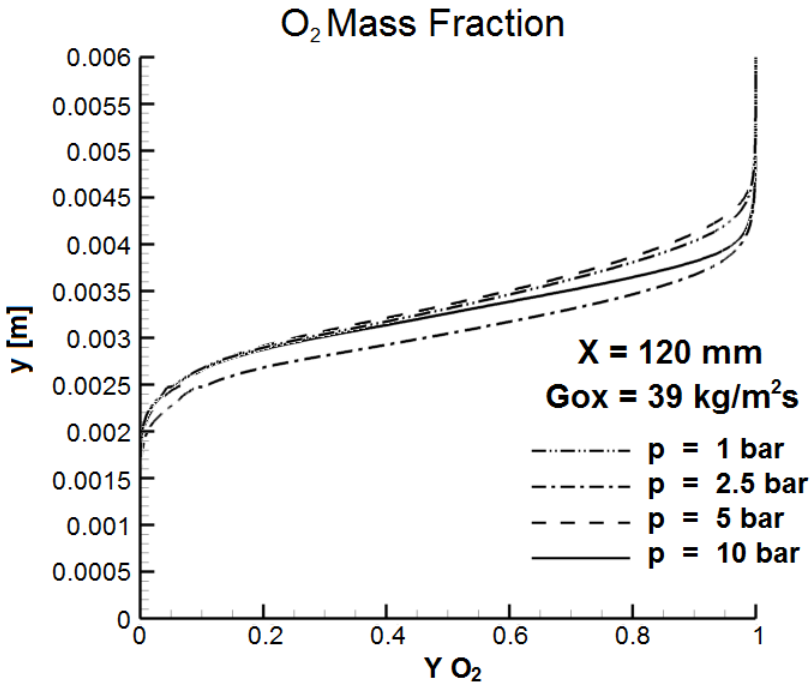

Figure 6.64: Section profiles of O_2 mass fraction - PaSR, with diffusion of enthalpy; $x = 120mm$, $G_{Ox} = 39kg/m^2s$, $Re_h = 11700$. Single slab.

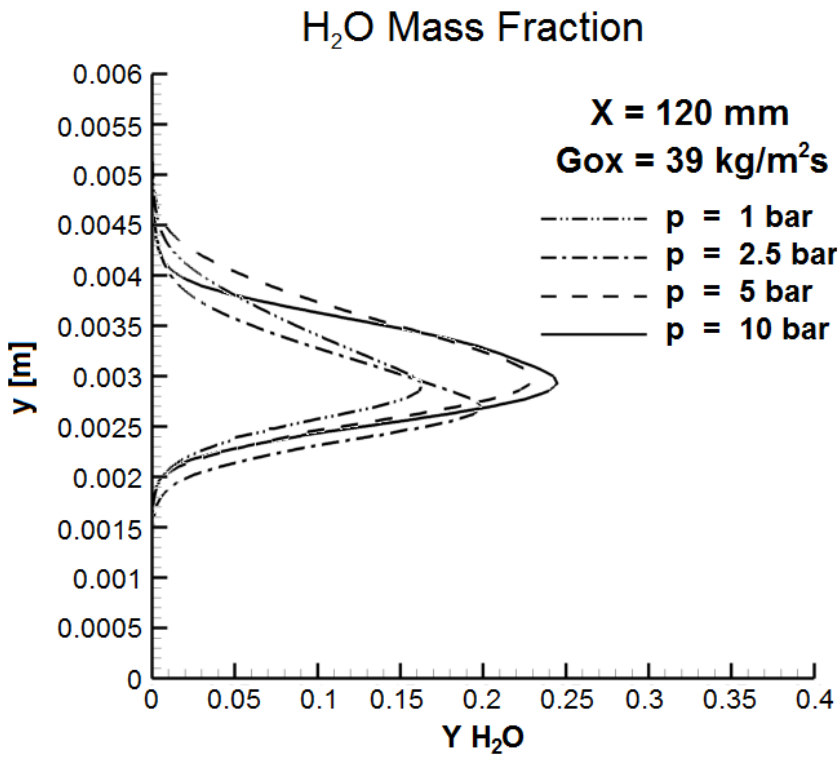

Figure 6.65: Section profiles of H_2O mass fraction - PaSR, with diffusion of enthalpy; $x = 120mm$, $G_{Ox} = 39kg/m^2s$, $Re_h = 11700$. Single slab.

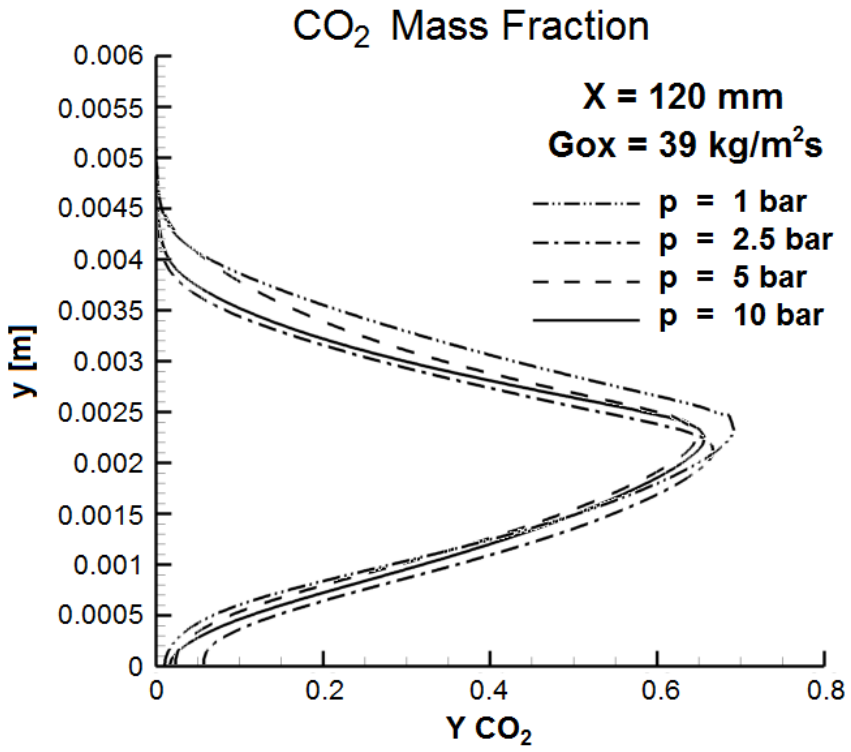

Figure 6.66: Section profiles of CO_2 mass fraction - PaSR, with diffusion of enthalpy; $x = 120mm$, $G_{Ox} = 39kg/m^2s$, $Re_h = 11700$. Single slab.

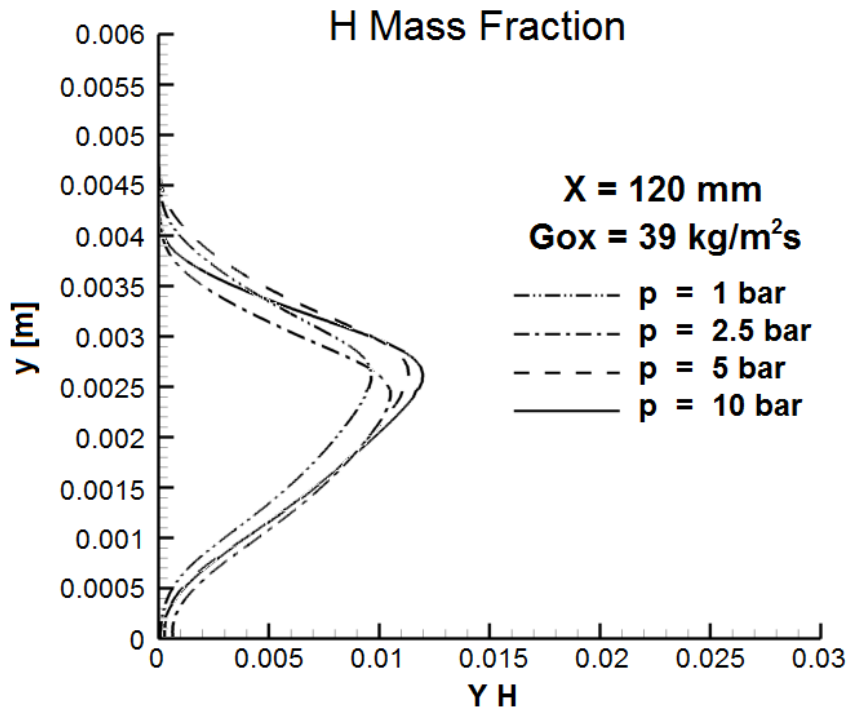

Figure 6.67: Section profiles of H mass fraction - PaSR, with diffusion of enthalpy; $x = 120mm$, $G_{Ox} = 39kg/m^2s$, $Re_h = 11700$. Single slab.

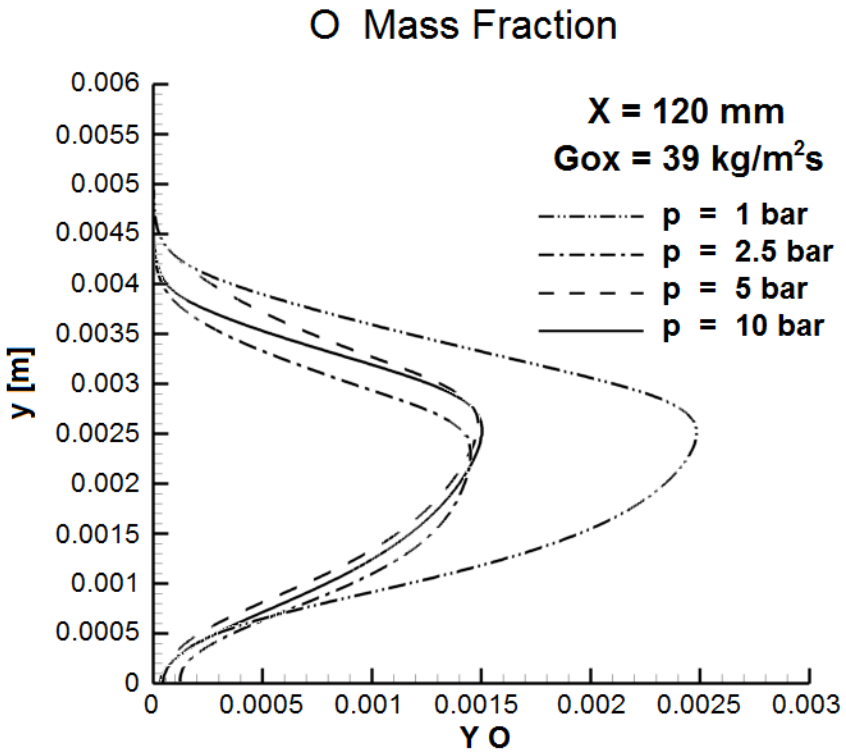

Figure 6.68: Section profiles of O mass fraction - PaSR, with diffusion of enthalpy; $x = 120mm$, $G_{Ox} = 39kg/m^2s$, $Re_h = 11700$. Single slab.

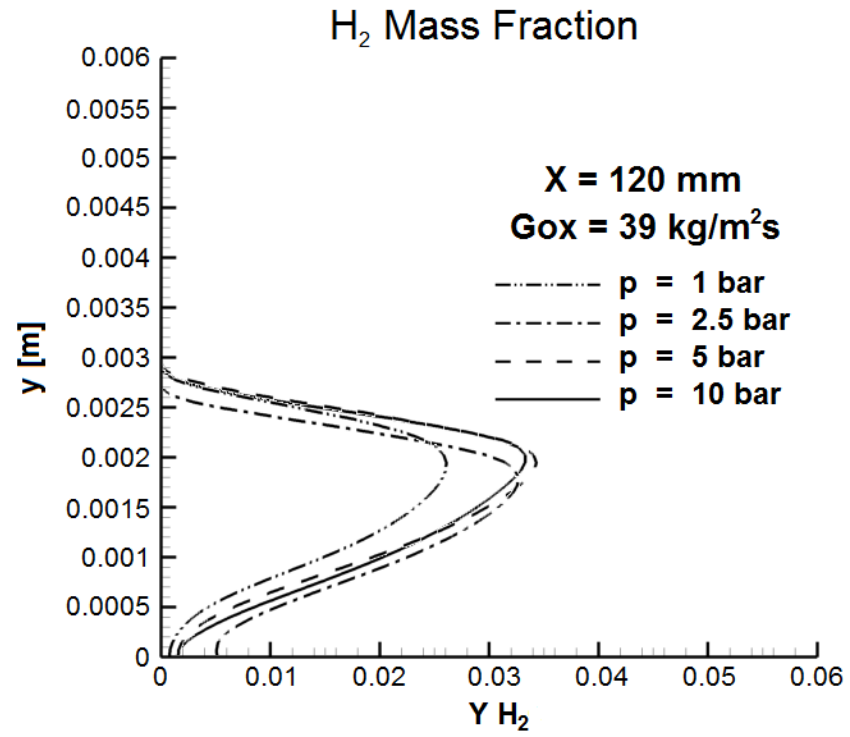

Figure 6.69: Section profiles of H_2 mass fraction - PaSR, with diffusion of enthalpy; $x = 120mm$, $G_{Ox} = 39kg/m^2s$, $Re_h = 11700$. Single slab.

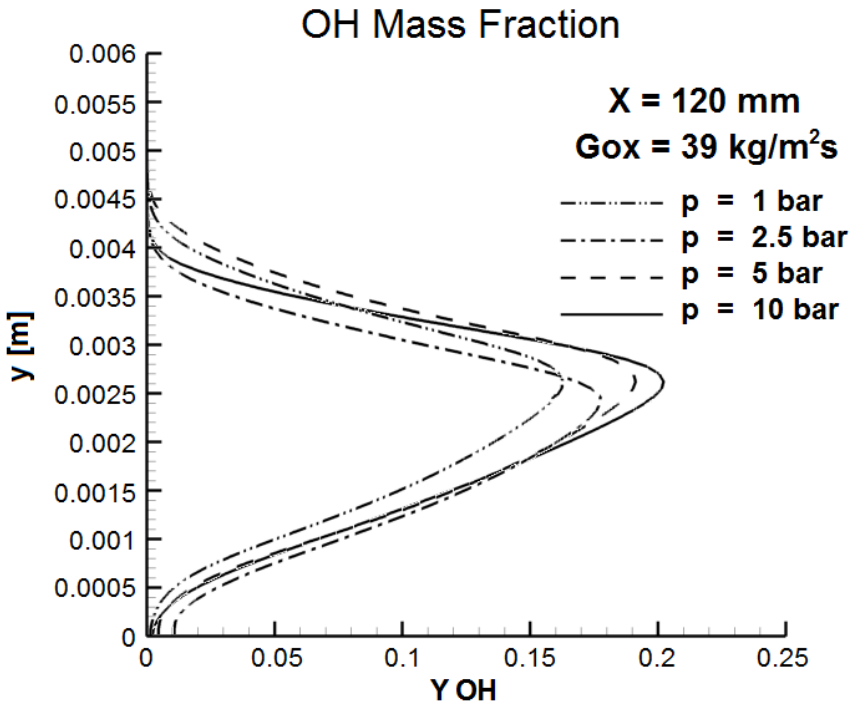

Figure 6.70: Section profiles of OH mass fraction - PaSR, with diffusion of enthalpy; $x = 120mm$, $G_{Ox} = 39kg/m^2s$, $Re_h = 11700$. Single slab.

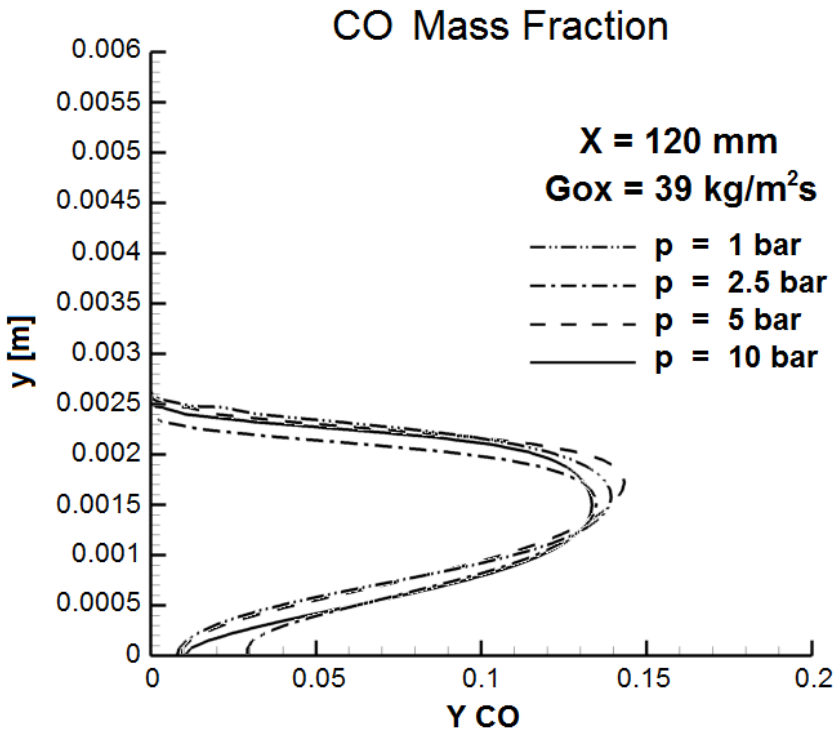

Figure 6.71: Section profiles of CO mass fraction - PaSR, with diffusion of enthalpy; $x = 120mm$, $G_{Ox} = 39kg/m^2s$, $Re_h = 11700$. Single slab.

6.6.1 Considerations on Computational Time

Computations were performed on an Intel Core i7-940 2.93 GHz quad-core machine with 8 GB of RAM memory. With reference to table 6.60, some considerations on computational time for the testcases indicated can be performed. Each PSR testcases at 1 bar pressure took approximatively 168 hours of computational time to reach the steady state. Testcases at same pressure with PaSR approach took approximatively 210 hours to reach the steady state, with an increase of computational time near 25%. This is dependant on the PaSR correction applied to each computational cell. As said, increasing the pressure required lower CFL values to reach convergenec: therefore the time required to reach steady state is additionally increased in higher pressure testcases. In particular, for the 10 bar pressure, each testcase took approximatively 450 hours of computational time to reach the steady state.

6.7 Regression Rate Results

Regression rate is one of the most important parameters for the evaluation of both hybrid rocket engine performance and solid fuel quality. It represents the speed at which the solid fuel grain is consumed during combustion. As a general trend, the higher the regression rate, the better the fuel. When studying hybrid rocket engine combustion chambers (numerically or experimentally), without the presence of a nozzle, parameters such as thrust and specific impulse are not directly available. Therefore regression rates is the most important parameters to assess and to use for comparison. Within this framework, regression rate measurement is of utmost importance to validate numerical results from COOLFluiD simulations. Next sections show results obtained.

6.7.1 Influence of Oxidizer Mass Flux and Pressure

Regression rate analysis involves the calculation of regression rate using the appropriate boundary condition described in chapter 5, as in equation (5.26), (5.27) and (5.28). All results shown are for single-slab testcases. Fuel surface temperature over slab length and local regression rate over slab length are presented and, coherently with the spirit of the present work, for the most accurate conditions available: fully turbulent chemistry source term (PaSR) and the contribution of diffusion of enthalpy at fuel surface are considered. All results were however examinated and it is importand to understand that this does not reduces the general validity of the conclusions pointed out. Nevertheless less accurate cases mean regression rate is used for the final comparison. Results are therefore shown in figures from 6.72 to 6.81. Figures 6.72 and 6.73 show respectively the local surface temperature and the local regression rate for increasing oxidizer inlet velocity (and therefore increasing oxidizer inlet mass flux) for the testcases with 1 bar of pressure. Figures 6.74 and 6.75 show again the local surface temperature and the local regression rate for increasing oxidizer inlet velocity (and therefore increasing oxidizer mass flux) for the testcases with 2.5 bar of pressure. Figures 6.76 and 6.77 show the same for the testcases with 5 bar of pressure and figures 6.78 and 6.79 show surface temperature and regression rate for the testcases with 10 bar of pressure. Three main considerations are possible:

- the increase of oxidizer inlet velocity corresponds to an increase of regression rate at the fuel grain head-end;
- the regression rate is not constant along the fuel grain, but has a peak in the fuel grain head-end;
- this behavior is very similar, with littel variations, for all the pressures investigated.

This behavior is coherent with experimental results, as shown by [114]. The behavior depicted by figures from 6.72 to 6.81 might partially explain the different behavior noticed in literature. In fact the head-end effect seems to be very important for the correct measurement of hybrid rocket engines regression rate and, at the same time, this effect is

more significant for shorter fuel slabs, where the reduced local regression rate along the grain is less compensating within the averaging procedure.

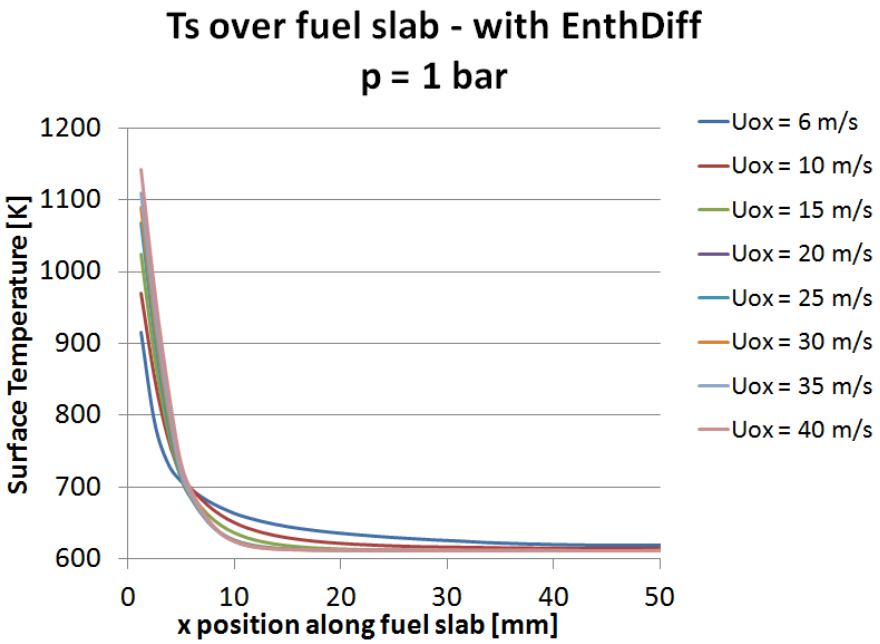

Figure 6.72: Computed fuel surface temperature vs. grain length. PsSR with diffusion of enthalpy. Pressure 1 bar

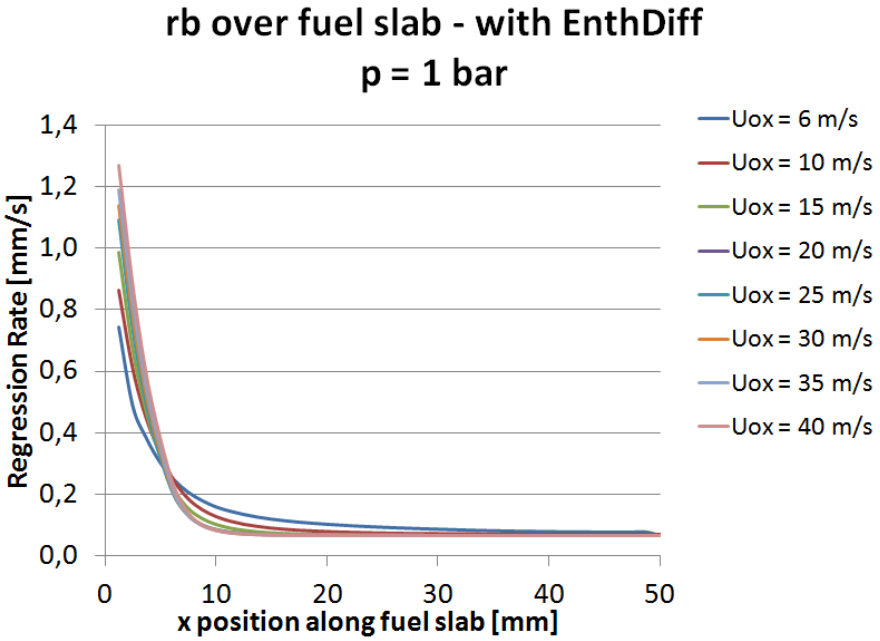

Figure 6.73: Computed fuel regression rate vs. grain length. PsSR with diffusion of enthalpy. Pressure 1 bar

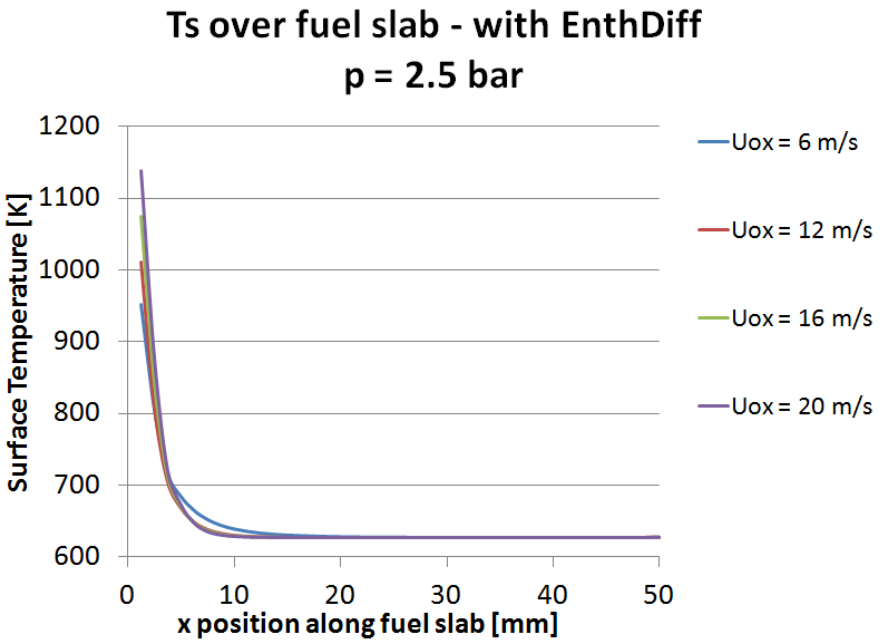

Figure 6.74: Computed fuel surface temperature vs. grain length. PsSR with diffusion of enthalpy. Pressure 2.5 bar

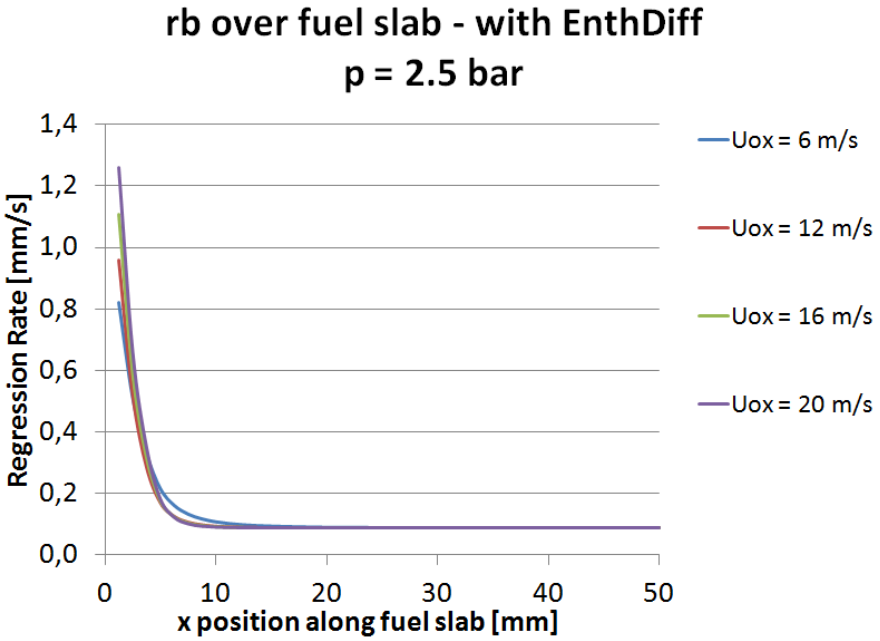

Figure 6.75: Computed fuel regression rate vs. grain length. PsSR with diffusion of enthalpy. Pressure 2.5 bar

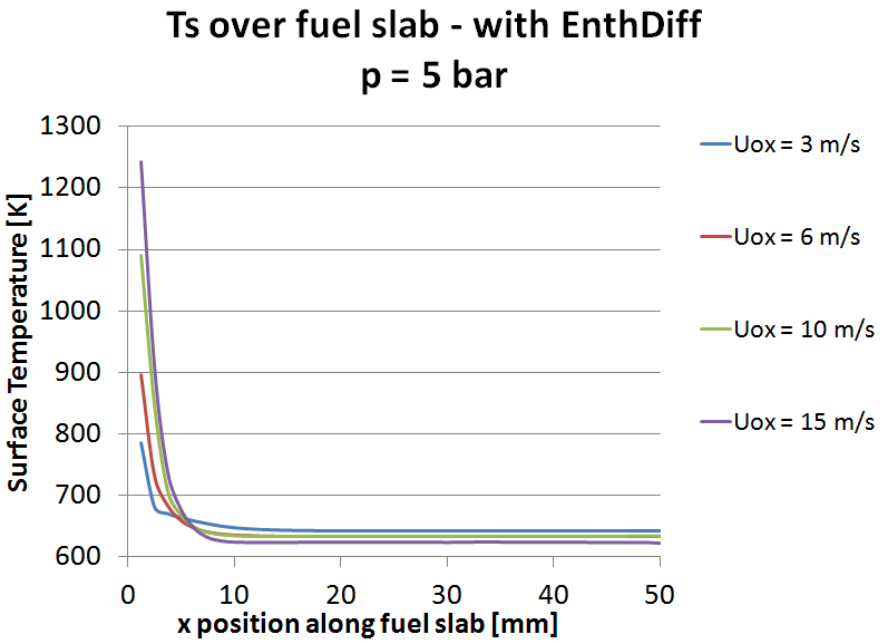

Figure 6.76: Computed fuel surface temperature vs. grain length. PsSR with diffusion of enthalpy. Pressure 5 bar

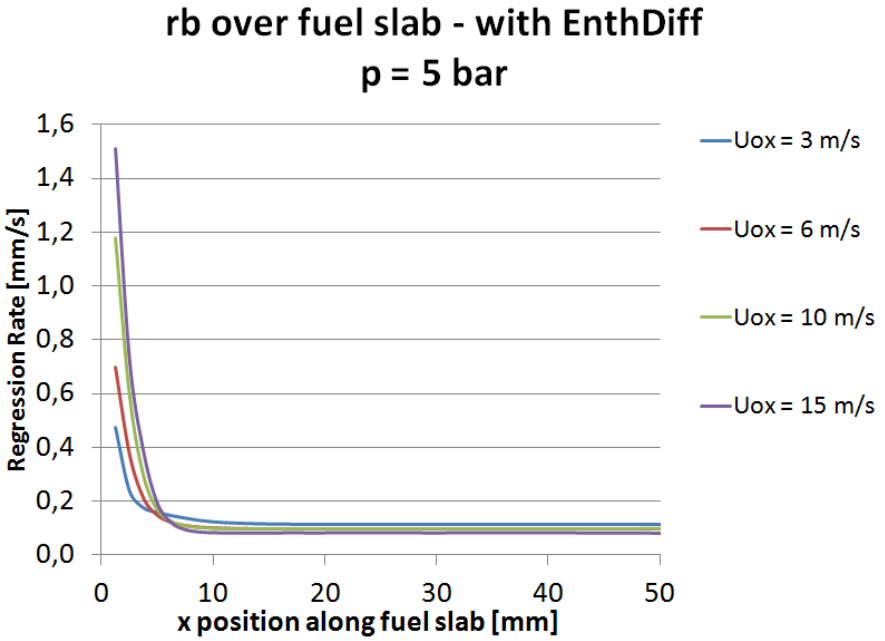

Figure 6.77: Computed fuel regression rate vs. grain length. PsSR with diffusion of enthalpy. Pressure 5 bar

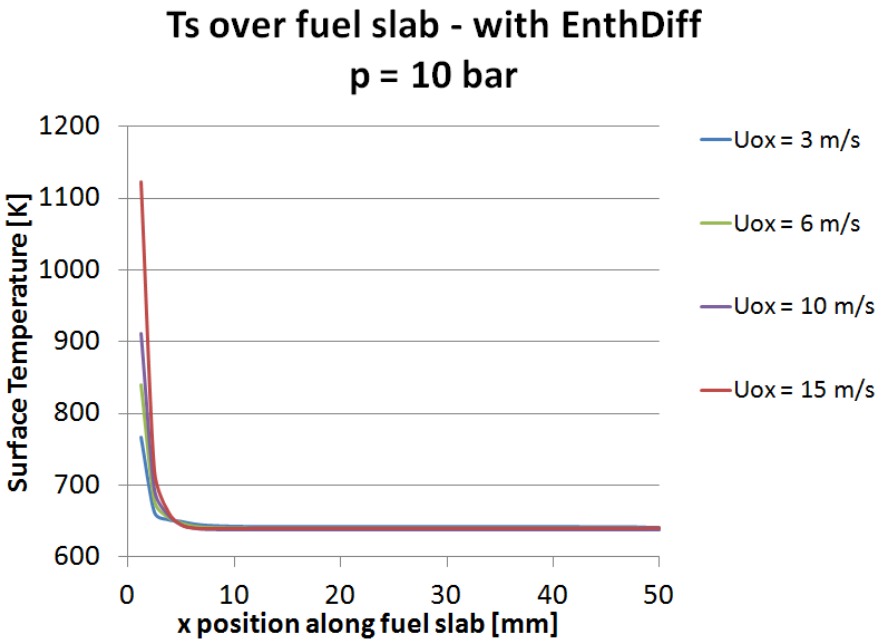

Figure 6.78: Computed fuel surface temperature vs. grain length. PsSR with diffusion of enthalpy. Pressure 10 bar

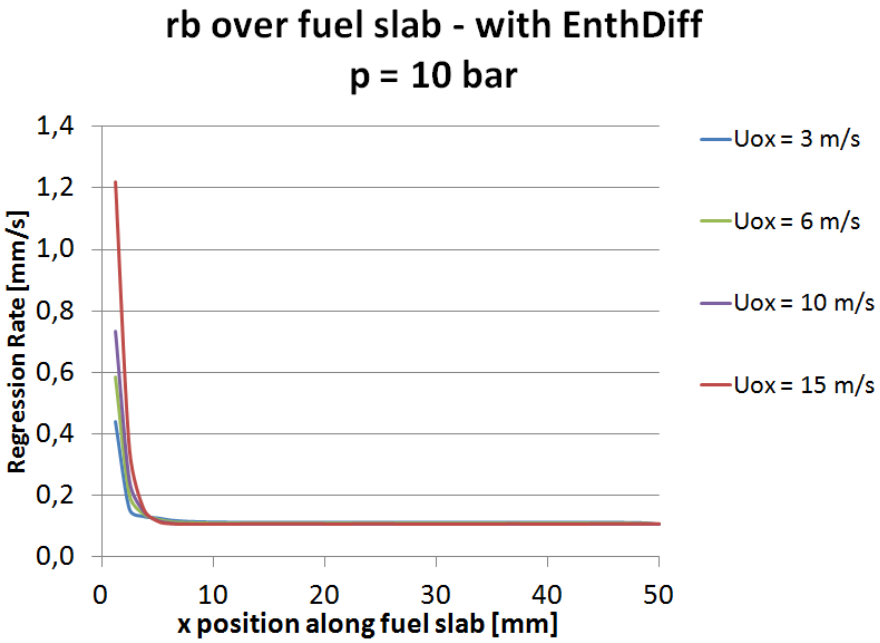

Figure 6.79: Computed fuel regression rate vs. grain length. PsSR with diffusion of enthalpy. Pressure 10 bar

In order to compare the effects of pressure on local fuel surface temperature and local regression rate along the fuel slab lenght, two additiona figures are presented. Figure 6.80

and 6.81 shows these values for increasing pressure (1, 2.5, 5, 10 bar) and fixed oxidizer mass flux $G_{Ox} = 39 kg/m^2 s$ or Reynolds number $Re_h = 11700$.

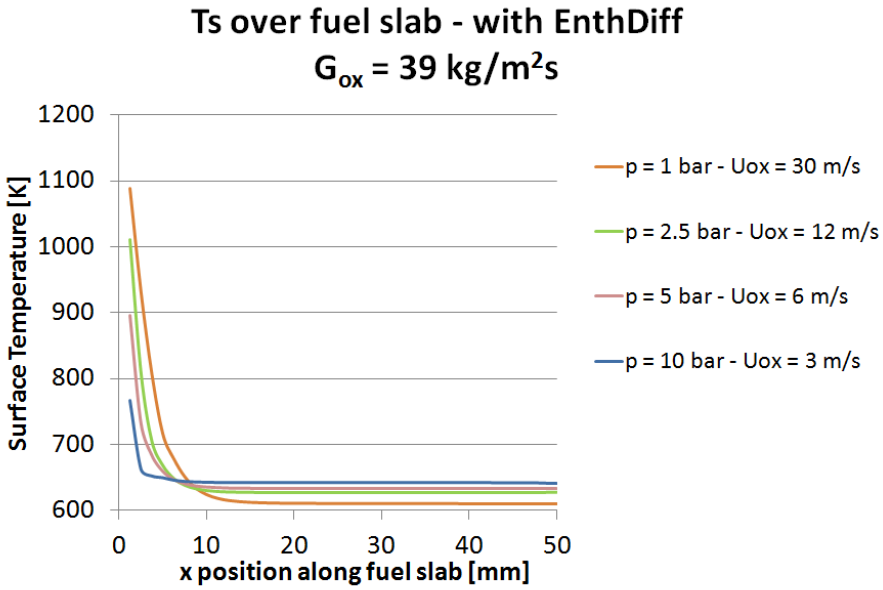

Figure 6.80: Computed fuel surface temperature vs. grain length. PsSR with diffusion of enthalpy. Oxidizer mass flux $39\, kg/m^2 s$, $Re_h = 11700$

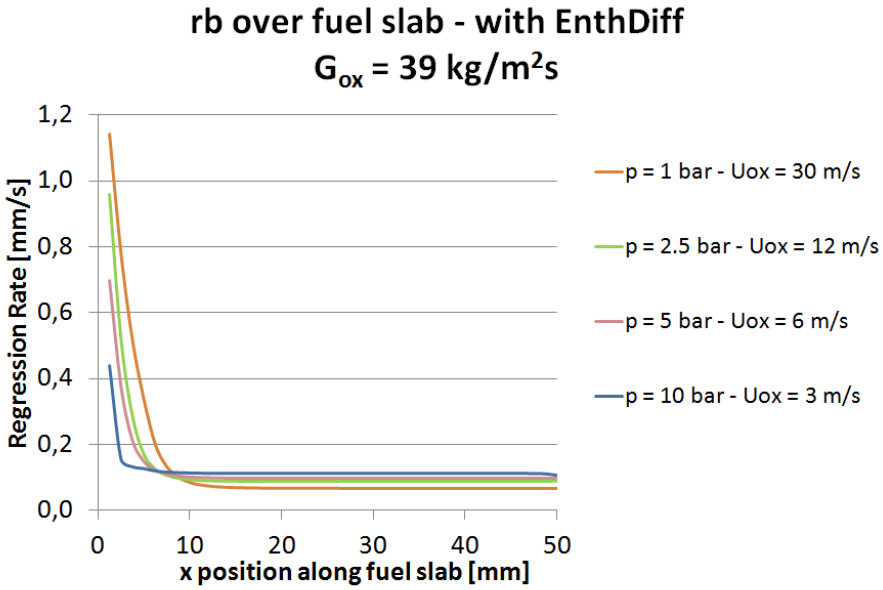

Figure 6.81: Computed fuel regression rate vs. grain length. PsSR with diffusion of enthalpy. Oxidizer mass flux $39\, kg/m^2 s$, $Re_h = 11700$

In correspondance of the head-end side of the fuel slab the peak temperature and therefore regression rate are noticeable higher at lower pressures. On the other hand,

proceeding downstream along the fuel grain an inversion of this phenomena is present: after a certain section, which advances towards the combustor end with decreasing pressure, at higher pressures corresponds an higher local regression rate. This could partially explain the different experimental results present in hybrid rocket literature concerning average regression rate. In fact an increasing, decreasing or neutral behavior can be identified with dependance on fuel grain length, pressure and location of the regression rate measurement devices. In particular it should be considered the ratio between head-end zone length (ehere a local regression rate peak is noticeable) and the length of the whole fuel slab. In fact it is foreseeable that globally longer fuel grains average regression rate will be influenced less by head-end local regression rate peaks. In addition the position of the sampling could influence the average regression rate by including or excluding a different number of peak, increasing, decreasing or neutral local regression rate regions. In the present work the average regression rate has been calculated along the whole grain, with one sample per computational cell, using an integral mean. Figure 6.82 shows a comparison between the different COOLFluiD results and regression rates from literature.

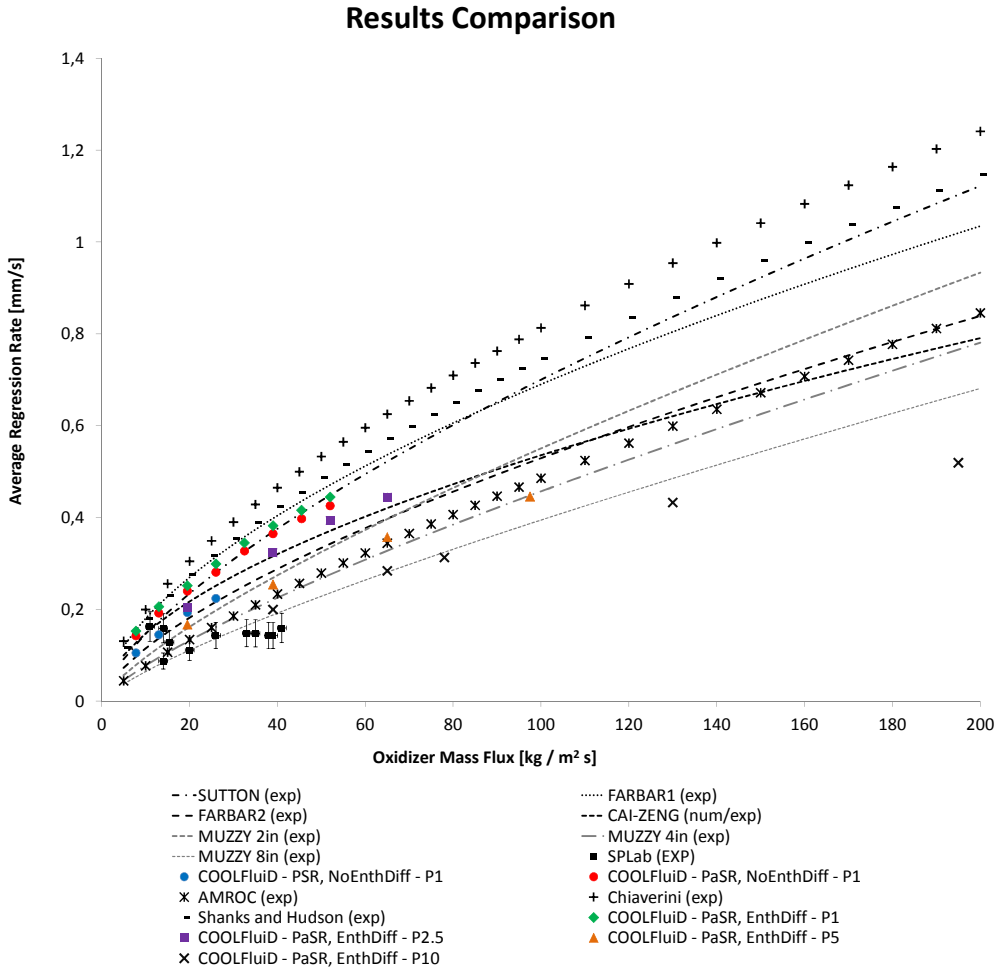

Figure 6.82: Average regression rates comparison between COOLFLuiD computations and literature data.

Noticeably, all COOLFluiD results are coherent with literature results from both numerical and experimental tests, as in [100], [118], [119], [120], [121], [2] and [122]. As shown in [100], the range of oxidizer inlet mass flux investigated extends over the typical range by single slab fuel configurations and the maximum value shown, near $200\,kg/m^2s$ is close to the maximum value reached by experimental facilities. In addition, it is possible to discuss the differences between different COOLFluiD regression rate results. Some comparisons are possible:

1. PaSR results versus PSR results, both without the contribution from diffusion;
2. PaSR results with and without the contribution from diffusion;
3. pressure increase for same oxidizer mass fluxes;

The first comparison shows that PaSR measured regression rate is on average 23% higher than PSR measured regression rate. It is possible to explain this phenomenon by the significant difference in peak temperature region area, which is significantly higher with

PaSR approach. A wider hot area, which is therefore nearer the wall with respect to PSR, consists in an enhanced heat return to the wall, thus PaSR wall temperature is higher. An higher wall temperature corresponds to an higher regression rate. The second comparison shows that a small contribution to regression rate from diffusion of enthalpy at wall exists, but this is on average in the order of 5%. The general trend for regression rate, however, is not affected. The third comparison confirms that, for small lenght of fuel grains, the increase of pressure has an overall effect of reduction in average regression rates. Table 6.1 shows the regression rate power laws in which r_b is a function of oxidizer mass flux G_{Ox}, as in $r_b = aG_{Ox}^n$.

Regression Rate Laws $r_b = aG_{Ox}^n$		
Case	**a**	**n**
PSR, No EnthDiff, $p = 1$ bar	0.0283	0.6384
PaSR, No EnthDiff, $p = 1$ bar	0.0430	0.5813
PaSR, EnthDiff, $p = 1$ bar	0.0477	0.5663
PaSR, EnthDiff, $p = 2.5$ bar	0.0292	0.6551
PaSR, EnthDiff, $p = 5$ bar	0.0267	0.6166
PaSR, EnthDiff, $p = 10$ bar	0.0223	0.6030

Table 6.1: Regression rate laws

In addition it is possible to compare average regression rate points at each pressure for corresponding values of oxidizer inlet mass flux, as shown in figure 6.83. Figure 6.83 shows again that pressure has an overall effect of reduction on average regression rate and that an increase in oxidizer inlet mass flux greatly increases average regression rate. In addition it is possible to notice that the reducing effect of pressure on average regression rate decreases with increasing pressure. For very high pressures a neutral behavior of pressure increase on average regression rate is foreseeable.

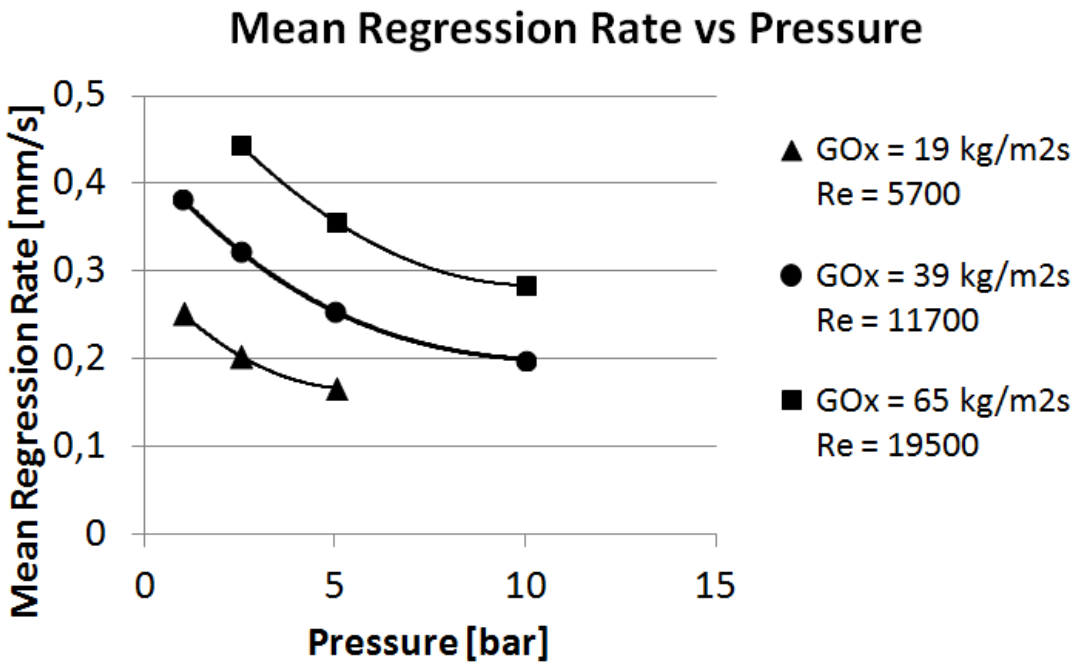

Figure 6.83: Average regression rates comparison at different oxidizer mass fluxes.

Chapter 7

Conclusions and Future Work

This chapter tries to draw some conclusions from the present work and to give some indications for future developments.

7.1 Conclusions

The present doctoral thesis work was devoted to the developement of a numerical tool for the simulation of combustion processes inside hybrid rocket engine combustion chambers. This work is a possible approach to address and possibly overcome the limits found in both previous and current research works, which lead essentially to results which are to be generally considered qualitative and not quantitative due to the strong approximations in the closure of governing equations. The main reason of these approximations is the difficulty inherent in the modelization of such complex and interconnnected phenomena as those involved in hybrid rocked combustion.

Therefore, in this work, an accurate closure of governing equations was found and implemented, in order to model with precision the physical phenomena involved.

Moreover, different chemical reaction models were investigated in order to conjugate accuracy, reliability and computational cost requirements. A global reaction scheme with six reaction and nine chemical species was identified as a suitable choice for the simulation of traditional HTPB-based hybrid rocket fuel formulations.

Numerical simulations were performed in order to test the influence of increase in oxidizer mass flux on main combustor parameters, such as temperature, axial velocity and chemical species mass fractions distribution. A link was found between the increase in oxidizer inlet mass fraction and the increase in both fluid axial velocity at combustor end and peak temperature. This results is useful as a base validation of the code functionality, which demonstrates itself able to correctly capture the problem physics.

Even if the nature of the physico-chemical and fluid-dynamic phenomena involved in the combustion processes of hybrid rocket engines are intrinsecally turbulent, the vast majority of results available in literature are obtained under quasi-laminar assumptions. Therefore, tests were also performed in order to assess the differences between a fully tur-

bulent fluid-dynamic model under quasi-laminar hypothesis for chemistry source term and the same fully turbulent model, but with a more accurate description of chemistry source term, now in a turbulent fashion under partially stirred reactor approach. The most important information obtained lies in the fact that without a turbulent treatment of chemistry source term, even if the governing equations are fully turbulent, the flame shows a geometry very similar to laminar conditions from literature. This is shown by the differante shape of high temperature regions of PSR and PaSR simulated testcases and also by the profiles of oxidizer and fuel species mass fractions. The conclusion that fully and accurately modeled turbulent governing equations is not a sufficient condition to achieve a turbulent flame might seem trivial, but it was never openly assessed before. In fact this work shows that a fully turbulent chemistry source term is necessary in order to obtain a fully turbulent flame, independently on the level of accuracy in the closure of turbulent terms in the energy conservation equation.

Tests are also performed in order to estimate a measure for both local and average solid fuel regression rate, with an accurate boundary condition description. This boundary condition also accounts for the effect of diffusion of chemical species enthalpy at the fuel surface, an accurate approach which is not always performed in literature works. These tests are performed with increasing oxidizer inlet mass flux and increasing pressure, in order to assess both effects on regression rate estimation.

The effects of pressure on hybrid rocket combustion processes and on both local and average regression rate are yet an open research problem. As discussed, different results are available in literature. These results, even if conflicting, are all scientifically valid and to be considered carefully within the limits of each approach. In particular, the average regression rate measurement could be affected by several factors, such as the length of fuel grain and the sampling measurement positions.

The characteristics of the simulated testcases of present work are in accord with literature sources which consider average fuel regression rates as decreasing with an increase of chamber pressure. In addition the general trend that assesses a peak in local regression rate in the fuel head-end region is confirmed.

The results obtained using the developed code are also compared not only with literature results but also with experimental tests performed in an ad-hoc test facility.

In conclusion, results are in good accord with problem physics. Temperature range and regression rate values are both coherent with literature data and experimental results.

7.2 Future Work

Inbetween the possible future developments for the present work, a few appear particularly promising.

1. the simulation of 2D and 3D geometries of complete hybrid rockets, including injector head, pre-chamber, post-chamber and gasdynamic nozzle. This can be done because the model developed in this work is also 3D;

2. the implementation of a radiation model, able to describe precisely the radiative heating effects inside the combustion chamber;

3. extensive testing on a wider range of operational conditions, with particular attention to further increase in oxidizer mass flux, pressure and fuel slab length;

4. the development of a comprehensive strategy for the simulation of innovative, paraffin-based fuel formulations.

First three suggestions are self-explainatory, however the fourth requires further discussion. In order to fully simulate the family of paraffin-based fuels, some very important steps are necessary.

First step is to identify the main gaseous product of paraffin-based fuel pyrolisis, which is an open research issue: gaseous hydrocarbons such as decane $(C_{10}H_{22})$, undecane $(C_{11}H_{24})$, dodecane $(C_{12}H_{26})$ and their mixture is the most promising choice. Noticeably these hydrocarbons are very similar to the ones used for simulation of diesel, kerosene and JP-1 fuels.

As a second step, it is necessary to find/develop and validate a physico-chemical model for the chosen hydrocarbons. This involves not only reaction chemistry, which is not readily available, but also the identification of specific models for thermodynamic and transport properties. The *CombustionModelLibrary2* is already able to accept data for paraffin-based fuels in terms of viscosity, thermal conductivity, specific heat, enthalpy and chemical/stoichiometric coefficients.

The third step, probably the most challenging, requires the identification and the implementation of governing equations for liquefying fuels with *entrainment* effect. Since the fuel burns as a spray, this task involves the choice of an adequate model for droplet mass, momentum and energy exchange with the fluid and droplet-to-droplet. A suitable approach seems to be the Eulerian-Eulerian one, as described in the works of Laurent [123], Jaegle [124] and Massot [125]. In addition, the injection of fuel droplets (also without the modeling of the thin liquid film layer) requires the development and the implementation of an accurate and consistent boundary condition.

Bibliography

[1] G.A. Marxman, C.E. Wooldridge, and R.J. Muzzy, *Fundamentals of Hybrid Boundary Layer Combustion*, 1963. AIAA 63-505.

[2] M.J. Chiaverini, N. Serin, D.K. Johnson, Y.C. Lu, and G.A. Risha, *Regression Rate Behavior of Hybrid Rocket Solid Fuels*, Journal of Propulsion and Power, 16(1), 2000.

[3] Venkateswaran, S. and C. L. Merkle. 1996. Size Scale-Up in Hybrid rocket Motors. *AIAA Paper 1996-0647*. 34th Aerospace Sciences Meeting and Exhibit. Reno, NV.

[4] Cheng, G.C., Farmer, R.C., Jones, H.S. and J.S. McFarlane. 1994. Numerical Simulation of the Internal Ballistic of a Hybrid Rocket Motor. *AIAA Paper 94-0554*. 32nd Aerospace Sciences Meeting and Exhibit, Reno, NV.

[5] Chen, Y.S., Chou, T.H., Gu, B.R., Wu, J.S., Wu, B., Lian, Y.Y. and L. Yang. 2011. Multiphysics simulations of rocket engine combustion. *Computers and Fluids*. 45:29-36.

[6] D. Altman, *Hybrid Rocket Development History*, 1991. AIAA 91-2515.

[7] P.N. Estey, and G.R. Whittinghill, *Hybrid Rocket Motor Propellant Selection Alternatives*, 1992. AIAA 92-3592.

[8] R.J. Kniffen, B. McKinney, and P. Estey, *Hybrid Rocket Development at the American Rocket Company*, 1990. AIAA 90-2762.

[9] C. Oiknine, *New Perspectives for Hybrid Propulsion*, 2006. AIAA 2006-4674.

[10] M.A. Karabeyoglu, B.J. Cantwell, and D. Altman, *Development and Testing of Paraffin-based Hybrid Rocket Fuels*, 2001. AIAA 2001-4503.

[11] G.A. Marxman, and C.E. Wooldridge, *Research on the Combustion Mechanism of Hybrid Rocket*, Combustion and Propulsion Panel, AGARD, NATO, April 1965.

[12] C.E. Wooldridge, G.A. Marxman, and R.J. Kier, *Investigation of Combustion Instability in Hybrid Rockets*, NASA internal report, contract NAS 1-7310, Stanford Research Inst., 1969.

[13] M.J. Chiaverini, K.K. Kuo, A. Peretz, and G.C. Harting, *Regression-Rate and Heat-Transfer Correlations for Hybrid Rocket Combustion*, AIAA Journal, 17(1): 99-110, 2001.

[14] M.A. Karabeyoglu, D. Altman, and B.J. Cantwell, *Combustion of Liquefying Hybrid Propellants: part 1, General Theory*, Journal of Propulsion and Power, 18(3): 610-620, 2002.

[15] M.A. Karabeyoglu, and B.J. Cantwell, *Combustion of Liquefying Hybrid Propellants: part 2, Stability of Liquid Films*, Journal of Propulsion and Power, 18(3): 621-630, 2002.

[16] M.A. Karabeyoglu, G. Zilliac, B.J. Cantwell, S. De Zilwa, and P. Castelluci, *Scale-up Tests of High Regression Rate Liquefying Hybrid Rocket Fuels*, 2003. AIAA 2003-1162.

[17] P.N. Estey, D. Altman, and J. McFarlane, *An Evaluation of Scaling Effects for Hybrid Rocket Motors*, 1991. AIAA 91-2517.

[18] A. Gany, *Scale Effects in Hybrid Motors under Similarity Conditions*, 1996. AIAA 96-2846.

[19] B.J. Evans, N.A. Favorito, E. Boyer, G.A. Risha, R.B. Wehrman, and K.K. Kuo, *Characterization of Nano-Sized Energetic Particle Enhancement of Solid-Fuel Burning Rates in an X-Ray Transparent Hybrid Rocket Engine*, 2004. AIAA 2004-3821.

[20] S. Kim, J. Lee, G. Kim, J. Cho, H. Moon, H. Sung, and J. Kim, *Combustion Characteristics of the Cylindrical Multi-port Grain for Hybrid Rocket Motor*, 2009. AIAA 2009-5112.

[21] C.E. Woolridge, and G.A. Marxman, *Combustion Instability and the Role of Chemical Kinetics in Hybrid Combustion*, 1968. AIAA 68-498.

[22] M. Wessel, B. Thibaudeau, and B. Minaeff, *Hybrid Rocket Instability*, ME-S06-01, 2001.

[23] S. De Zilwa, A. Karabeyoglu, G. Zilliac, and L. King, *Combustion Oscillations in High-Regression-Rate Hybrid Rockets*, 2003. AIAA 2003-4465.

[24] Karabeyoglu, A., Stevens, J. Advanced Hybrid Rockets for Future Space Launch. 5th European Conference for Aeronautics and Space Sciences. Munich, Germany, 1-5 July 2013.

[25] G.A. Risha, E. Boyer, R.B. Wehrman, and K.K. Kuo, *Performance Comparison of HTPB-based Solid Fuels Containing Nano-sized Energetic Powder in a Cylindrical Hybrid Rocket Motor*, 2002. AIAA 2002-3576.

[26] C. Lee, Y. Na, and G. Lee, *The Enhancement of Regression Rate of Hybrid Rocket Fuel by Helical Grain Configuration and Swirl Flow*, 2005. AIAA 2005-3906.

[27] K. Kitagawa, T. Mitsutani, T. Ro, and S. Yuasa, *Effects of Swirling Liquid Oxygen Flow on Combustion of a Hybrid Rocket Engine*, 2004. AIAA 2004-3479.

[28] K.H. Shin, C. Lee, S.Y. Chang, and J.Y. Koo, *The Enhancement of Regression Rate of Hybrid Rocket Fuel by Various Methods*, 2005. AIAA 2005-0359.

[29] P. George, S. Krishnan, P.M. Varkey, M. Ravindran, and L. Ramachandran, *Fuel Regression Rate in Hydroxyl-Terminated-Polybutadiene/Gaseous-Oxygen Hybrid Rocket Motors*, Journal of Propulsion and Power, 17(1), 2001.

[30] A.V. Potapkin, and T.S. Lee, *Experimental Study of Thrust Performance of a Hybrid Rocket Motor with Various Methods of Oxidizer Injection*, Combustion, Explosion, and Shock Waves, 40(4): 386-392, 2004.

[31] C. Carmicino, and A. Russo Sorge, *Role of Injection in Hybrid Rockets Regression rate Behavior*, Journal of Propulsion and Power, 21(4), 2005.

[32] C. Carmicino, and A. Russo Sorge, *Performance Comparison between two Different Injector Configurations in a Hybrid Rocket*, Aerospace Science and Technology, 11: 61-67, 2007.

[33] C. Carmicino, and A. Russo Sorge, *The Effects of Oxidizer Injection Design on Hybrid Rockets Combustion Stability*, 2006. AIAA 2006-4677.

[34] Lin, C.L., and H.H. Chiu. 1995. Numerical Analysis of Spray Combustion in Hybrid Rockets. In: AIAA Paper 95-2687.

[35] Venkateswaran, S. 2007. Computational Fluid Dynamics Modeling of Hybrid Rocket Flowfields. In: *Progress in Astronautics and Aeronautics*, Vol. 218, Fundamentals of Hybrid Rocket Combustion and Propulsion, pp. 323-349.

[36] Coronetti, A., and W.A. Sirignano, 2013. Numerical Analysis of Hybrid Rocket Combustion. In: *Journal of Propulsion and Power*, Vol. 29, N. 2, pp. 371-384.

[37] Nakagawa, I., S. Hikane, and T. Suzuki, 2009. A study on the Regression Rate of Paraffin-based Hybrid Rocket Fuels. AIAA 2009-4935.

[38] Bellomo, N., Lazzarin, M., and F. Barato, 2010. Numerical Investigation of the Effect of a Diaphragm on the Performance of a Hybrid Rocket Motor. AIAA 2010-7033.

[39] Chen, Y.S., Chou, T.H., Gu, B.R., Wu, J.S., Wu, B., Lian, Y.Y., and L. Yang, 2010. Multiphysics Simulations of Rocket Engine Combustion. Computers and Fluids 45(2011)29-36.

[40] Cheng, G.C., Farmer, R.C., Jones, H.S., and J.S. McFarlane, 1994. Numerical Simulation of the Internal Ballistics of a Hybrid Rocket Motor. AIAA 94-0554.

[41] Gao, X., Groth, C., A Parallel Solution - Adaptive Method for Three-Dimensional Turbulent Non-Premixed Combusting Flow, Journal of Computational Physics, 229: 3250 - 3275, 2010.

[42] M. Lazzarin, N. Bellomo, M. Faenza, F. Barato, A. Bettella, and D. Pavarin. Analysis of Fluid-dynamic Systems to Increase Combustion Efficiency in Hybrid Rockets. 5th European Conference for Aeronautics and Space Sciences. Munich, Germany, 1-5 July 2013.

[43] Grosse, M. Effect of a Diaphragm on Performance and Regression of a Laboratory Scale Hybrid Rocket Motor Using Nitrous Oxide and Paraffin, 45th AIAA/ASME/SAE/ASEE Joint Propulsion Conference & Exhibit, Denver, CO, 2009. AIAA-2009-5113

[44] D. Bianchi, A. Urbano, B. Betti, and F. Nasuti. Numerical Simulation of Hybrid Rocket Engine Flowfields. 5th European Conference for Aeronautics and Space Sciences. Munich, Germany, 1-5 July 2013.

[45] OpenCFD, OpenFOAM foundation, www.openfoam.com.

[46] F. Palacios, M. R. Colonno, A. C. Aranake, A. Campos, S. R. Copeland, T. D. Economon, A. K. Lonkar, T. W. Lukaczyk T. W. R. Taylor and J. J. Alonso. Stanford University Unstructured (SU^2): An open-source integrated computational environment for multi-physics simulation and design. 51st AIAA Aerospace Sciences Meeting including the New Horizons Forum and Aerospace Exposition. 7 - 10 January 2013, Grapevine (Dallas/Ft. Worth Region), Texas. AIAA 2013-0287.

[47] L. Merotto and A. Mazzetti, 2013. Numerical Simulations of Combustion Processes in Hybrid Rocket Engines Using OpenFoam and COOLFluiD Codes. 5th EUCASS, Munich (Germany).

[48] Merotto, L. and A. Mazzetti. Numerical Simulation of Combustion Processes in Hybrid Rocket Engines using OpenFOAM and COOLFluiD codes. 5th European Conference for Aeronautics and Space Sciences. Munich, Germany, 1-5 July 2013.

[49] Veynante, D., Vervisch, L., Turbulent Combustion Modeling, Progress in Energy and Combustion Science, 28: 193 - 266, 2002.

[50] Veynante, D., Poinsot, T., Theoretical and Numerical Combustion, R.T. Edwards, P.O. Box 27388, Philadelphia, PA, 19118; USA; 2001.

[51] Kuo, K.K., Principles of Combustion, 2nd Ed., Chapter 3. John Wiley & Sons, New York, NY; 2005.

[52] Williams, F.A., Combustion Theory, The Benjamin/Cummings Publishing Company, Inc., 1985.

[53] Giovangigli, V., Multicomponent Flow Modeling, MESST Series, Birkhauser Boston, 1999.

[54] Wilcox, D.C., Turbulence Modeling for CFD, 3rd Ed. Chapter 5. DCW Industries, 5354 Palm Drive, La Cañada, Calfornia, 91011; USA; 2006.

[55] Kays, W.M. Turbulent Prandtl Number - Where Are We?. Journal of Heat Transfer. 116(2):284-295. 1994.

[56] Venkateswaran, S., Merkle, C.L., Size Scale-Up in Hybrid Rocket Motors, AIAA Aerospace Sciences Meeting and Exhibit, 34th, Reno, NV; USA; 15-18 January, 1996, AIAA Paper 1996-0647.

[57] Golovitchev, V.I. 2001. Development of Universal Model of Turbulent Spray Combustion. *TFR Research Proposal*. Chalmers University of Technology.

[58] Arisawa, H., Brill, T.B., Flash Pyrolisis of Hydroxil-Terminated Polybutadiene (HTPB) I: Analysis and Implications of the Gaseous Products, Combustion and Flame 106: 131 - 143, 1996.

[59] Arisawa, H., Brill, T.B., Flash Pyrolisis of Hydroxil-Terminated Polybutadiene (HTPB) II: Implications of the Kinetics to Combustion of Organic Polymers, Combustion and Flame 106: 144 - 154, 1996.

[60] Westbrook, C.K., Dryer, F.L., Simplified Reaction Mechanisms for the Oxidation of Hydrocarbon Fuels in Flames, Combustion Science and Technology, 27: 31-43, 1981.

[61] Jones, W.P., Lindstedt, R.P., Global Reaction Schemes for Hydrocarbon Combustion, Combustion and Flame, 73(3): 233 - 249, 1988.

[62] Lazzarin, M., Bellomo, N., Faenza, M., Barato, F., Rondini, D., Manente, M., Bettella, A. and D. Pavarin. 2012. Numerical Investigation of Hybrid Motors for the EU FP7 SPARTAN Program. AIAA Paper 2012-3748. 48th AIAA/ASME/SAE/ASEE Joint Propulsion Conference & Exhibit. Atlanta, Georgia

[63] Golovitchev, V.I. and J. Chomiak. 2001. Numerical Modelling of High Temperature Air Flameless combustion.*The 4th international symposium on high temperature air combustion and gasification*. Rome. Italy.

[64] Nordin, N. 2001. Complex Chemistry Modeling of Diesel Spray Combustion. PhD Thesis. Chalmers University of Technology.

[65] Sabel'nikov, V. and C. Fureby. 2013. LES combustion modeling for high Re flames using a multi-phase analogy. *Combustion and Flame*. 160:83-96.

[66] Svehla, R.A., Transport Coefficients for the NASA Lewis Chemical Equilibrium Program, NASA Technical Memorandum 4647, NASA-TM-4647, National Aeronautics and Space Administration Lewis Research Center, Cleveland, Ohio, 44135 - 3191; USA; 1995; available online at http://www.sti.nasa.gov/STI-public-homepage.html.

[67] Green, D.W., Perry, R.H., Perry's Chemical Engineer Handbook, 8th Ed., McGraw-Hill, 2008.

[68] Chung, T.H., Lee, L.L., Starling, K.E., Applications of Kinetic Gas Theories and Multiparameter Correlation for Prediction of Dilute Gas Viscosity and Thermal Conductivity, Industrial and Engineering Chemical Fundamentals, 23(1): 8 - 13, 1984.

[69] Wilke, C.R., A Viscosity Equation for Gas Mixtures, The Journal of Chemical Physics, 18(4): 517 - 519, 1950.

[70] Stiel, L.I., Thodos, G., The Thermal Conductivity of Nonpolar Substances in the Dense Gaseous and Liquid Regions, American Institute of Chemical Engineers Journal, 10(1): 26 - 30, 1964.

[71] Yaws, C.L., Transport Properties of Chemical and Hydrocarbons, William Andrew Publishing, Boston, 2009.

[72] Senftleben, H., New values of thermal conductivity and specific heat at different temperatures for a series of gases, Zeitschrift fur angewandte Physik, 17(2): 6 - 7, 1964.

[73] Lambert J.D., Cotton K.J., Pailthorpe M.W., Robinson A.M., Scrivins J., Vale W.R.F., Young R.M., Transport Properties of Gaseous Hydrocarbons, Proceedings of the Royal Society of London, Series A , 231, 280-290, 1955.

[74] Mason, E.A., Saxena, S.C., Approximate Formula for the Thermal Conductivity of Gas Mixtures, The Physics of Fluids, 1(5): 361 - 369, 1958.

[75] Burcat, A., Ruscic, B., Third Millennium Ideal Gas and Condensed Phase Thermochemical Database for Combustion with Updates from Active Thermochemical Tables, Argonne Report ANL 05/20 and Technion Aerospace Report TAE N. 960, September 2005.

[76] McBride, B. J., Heimel, S., Ehlers, J. G., Gordon, S., Thermodynamic Properties to 6000 K for 210 Substances Involving the First 18 Elements. NASA-SP-3001 (1963).

[77] Ramshaw, J.D., Self-Consistent Effective Binary Diffusion in Multicomponent Gas Mixtures, Journal of Non-Equilibrium Thermodynamics, 15(3): 295 - 300, 1990.

[78] Hirschfelder, J.O., Curtiss, C.F., Bird, B.R., Molecular Theory of Gases and Liquids, John Wiley & Sons, New York, NY; 1954.

[79] Poling, B.E., Prausnitz, J.M., O'Connell, J.P., The Properties of Gases and Liquids, 5th Ed.,McGraw-Hill, 2001.

[80] Smith, L.W., Taylor, R., Film Models for Multicomponent Mass Transfer: A Statistical Comparison, Industrial and Engineering Chemistry Fundamentals, 22(1): 97 - 104, 1983.

[81] Cussler, E.L., Diffusion: Mass Transfer in Fluid Systems, 3rd Ed., Cambridge University Press, Cambridge, New York, NY, 10011-4211; USA; 2009.

[82] Fuller, E.N., Schettler, P.D., Giddings, J.C., A new method for prediction of binary gas-phase diffusion coefficients, Industrial and Engineering Chemistry, 58(5):19-27, 1966.

[83] Wilke, C.R., Lee, C.Y., Estimation of Diffusion Coefficients for Gases and Vapors, Industrial and Engineering Chemistry, 47(6):1253 - 1257, 1955.

[84] Chapman, S., Cowling, T.G., The Mathematical Theory of Non-Uniform Gases, 3rd Ed., Cambridge University Press, New York, NY, 10011-4211 1990.

[85] Lugg, G.A., Diffusion Coefficients of Some Organics and Other Vapors in Air, Analytical Chemistry, 40(7):1072-1077, 1968.

[86] Todd, B., Young, J.B., Thermodynamic and transport properties of gases for use in solid oxide fuel cell modeling, Journal of Power Sources, 110:186 - 200

[87] Lani, A. 2008. An Object riented and High Performance Platform for Aerothermodynamics Simulation. PhD Thesis. Université Libre de Bruxelles and von Karman Institute for Fluid Dynamics, Aeronautics and Aerospace Department.

[88] Quintino, T. 2008. A component environment for high-performance scientific computing - design and implementation. PhD Thesis. Katolieke Universiteit Leuven and von Karman Institute for Fluid Dynamics, Aeronautics and Aerospace Department.

[89] Wuilbaut, T., Algorithmics Developments for a Multiphysics Framework, Ph.D. Thesis, Université Libre de Bruxelles, December 2008.

[90] Liou, M.-S., A Sequel to AUSM, Part II: AUSM+-up, Journal of Computational Physics, 214: 137- 170, 2006.

[91] Balay, S., Gropp, W.D., Curfman McInnes, L. and B.F. Smith. 1997. Efficient Management of Parallelism in Object Oriented Numerical Software Libraries. Modern Software Tools in Scientific Computing. Editors: Arge, E., Brauset, A.M., and H.P. Langtangen. Birkhäuser Press. 163-202.

[92] LeVeque, R.J. Finite-Volume Methods for Hyperbolic Problems. Cambridge University Press. 2002.

[93] Hirsch, C. Numerical Computation of Internal and External Flows, volume 2. John Wiley & Sons, 1990.

[94] Barth, T., Ohlberger, M. Finite volume methods: foundation and analysis. Encyclopedia of Computational Mechanics, Volume 1, Fundamentals. 2004.

[95] Godunov, S.K. A difference method for numerical calculation of discontinuous solutions of the equations of hydrodynamics". Matematicheskii Sbornik, number 47, pages 271-306. 1959.

[96] Liou, M.-S. and Steffen, C., A New Flux Splitting Scheme, Journal of Computational Physics, 107: 23-39, 1993.

[97] Liou, M.-S., A Sequel to AUSM: AUSM+, Journal of Computational Physics, 129: 364-382, 1996.

[98] Liou, M.-S., A further development of the ausm+ scheme towards robust and accurate solutions for all speeds. In 16th AIAA Computational Fluid Dynamics Conference, Orlando, Florida, June 2003. AIAA 2003-4116.

[99] M. Delanaye, M. J. Aftosmis, M. J. Berger, Y. Liu, and T. Pulliam. Automatic hybrid-cartesian grid generation for high-reynolds number ows around complex geometries. In AIAA Paper 99-0777, Reno(NV), Jan 1999. 37th AIAA Aerospace Science Meeting and Exhibit. 126, 127.

[100] Mazzetti, A. 2010. Indagine teorica e sperimentale dei processi di combustione eterogenea in endoreattore ibrido. MSc Thesis. Politecnico di Milano, Aerospace Engineering Department.

[101] Menter, F.R. 1994. Two-Equation Eddy-Viscosity Turbulence Models for Engineering Applications. AIAA Journal. Vol. 32, No. 8, 1598-1605.

[102] Kataoka, I. 1986. Local Instant Formulation of Two-Phase Flow. International Journal of Multiphase Flow. Vol. 12, No. 5, pp. 745-758.

[103] L. Merotto, M. Boiocchi, A. Mazzetti, F. Maggi, L. Galfetti, and L.T. De Luca. Characterization of a family of paraffin-based solid fuels. 4th European Conference for Aeronautics and Space Sciences. St. Petersburg, Russia, 4-8 July 2011.

[104] Chapra, S.C. Applied Numerical Methods W/MATLAB: for Engineers & Scientists. 3rd Edition. McGraw-Hill. 2011.

[105] Brent, R. P. Algorithms for Minimization without Derivatives. Chapter 4. Englewood Cliffs, NJ: Prentice-Hall. 1973.

[106] Ridders, C. A new algorithm for computing a single root of a real continuous function. IEEE Transactions on Circuits and Systems 26: 979-980. 1979.

[107] Chiaverini, M.J., Harting, G.C., Yeu-Cheng Lu, Kuo, K.K., Peretz, A., Jones, S.H., Wygle, B.S. and J.P. Arves. Pyrolysis behavior of hybrid-rocket solid fuels under rapid heating conditions. Journal of Propulsion and Power 15 (7): 888-895. 1999.

[108] Incropera, F.P., DeWitt, D.P., Bergman, T.L. and A.S. Lavine. Fundamental of Heat and Mass Transfer. 6th Edition. John Wiley & Sons. 2006.

[109] Mazzetti, A. and P. Barbante. Object Oriented Techniques for the Numerical Simulation of Combustion Processes in Hybrid Rocket Engines. 5th European Conference for Aeronautics and Space Sciences. Munich, Germany, 1-5 July 2013.

[110] Abernathy, F.H., Film Notes for Fundamentals of Boundary Layers, National Committee for Fluid Mechanics Film, Encyclopedia Britannica Educational Corporation, 425 North Michigan Avenue, Chicago, IL, 1970

[111] Barbante P. and O. Chazot. Flight Extrapolation of Plasma Wind Tunnel Stagnation Region Flowfield. Journal of Thermophysics and Heat Transfer. 20(3): 493-498. 2006.

[112] Cai, G. and H. Tian. 2006. Numerical Simulation of the Operation Process of a Hybrid Rocket Motor. *AIAA Paper 2006-4506*. 42nd AIAA/ASME/SAE/ASEE Joint Propulsion Conference & Exhibit. Sacramento, CA.

[113] Law, C.K. 2006. Combustion Physics, 1st Edition. Cambridge University Press. New York. NY.

[114] De Luca L.T., Galfetti, L., Colombo G., Maggi F., Bandera A., Boiocchi M., Gariani, G., Merotto, L., Paravan, C., and A. Reina. Time-Resolved Burning of Solid Fuels for Hybrid ROcket Propulsion. EUCASS Advances in Aerospace Sciences, Luigi T. De Luca et al. (Ed.), Torus press & EDP Sciences, Moscow, 2011, ISBN: 9782759806737, p. 405-426.

[115] Price, C.F. and L.D. Smoot. Regression rates of nonmetalized hybrid fuel systems. 1965. AIAA Journal. Vol.3: 1408-1413.

[116] Yash, P., Kalpit, K. and P.K. Dash. Regression Rate Study of PVC/HTPB Hybrid Rocket Fuels. 2011. International Journalof Mechanical and Industrial Engineering. Volume 1(1): 64-67

[117] Risha, G. A., Harting, G.C., Kuo, K. K., Peretz, A., Koch, D.E., Jones, H.S. and J. P. Arves. Pyrolysis and Combustion of Solid Fuels in Various Oxidizing Environments. 1998. AIAA Paper 1998-3184, 34th AIAA/ASME/SAE/ASEE Joint Propulsion Conference and Exhibit, Cleveland, OH.

[118] Sutton, G. P. and O. Biblarz. 2001. Rocket Propulsion Elements. Seventh Edition. Wiley and Sons. Data from 2 in. lab-scale motor, Thiokol, 1989.

[119] Farbar, E., Louwers, J., ant T. Kaya. Investigation of metallized and nonmetallized hydroxyl terminated polybutadiene/hydrogen peroxide hybrid rockets. Journal of Propulsion and Power 23 (2). 2007.

[120] Cai, G., Zeng, P., Li, X., Tian, H. and N. Yu. 2013. Scale effect of fuel regression rate in hybrid rocket motor. Aerospace Science and Technology. 24: 141-146. 2013.

[121] Wooldridge, C.E. and R.J. Muzzy. Internal ballistic considerations in hybrid rocket design. Journal of Spacecraft and Rockets 4 (2): 255-262. 1967.

[122] Shanks, R.B. and M.K. Hudson. The design and control of a labscale hybrid rocket facility for spectroscopy studies. AIAA paper 94-3016, June 1994.

[123] Laurent, F. *Modélisation mathématique et numérique de la combustion de brouillards de gouttes polydispersés*. Ph.D. Thesis. Université Claude Bernard - Lyon I. 2002.

[124] Jaegle, F., Senoner, J.-M., Garcìa, M., Bismes, F., Lecourt, R., Cuenot, B., and T. Poinsot. *Eulerian and Lagrangian Spray Simulations of an aeronautical multipoint injector*. Proceedings of the Combustion Institute. 33: 2099-2107. 2011.

[125] Kah, D., Laurent, F., Massot, M. and S. Jay. *A high order moment method simulating evaporation and advection of a polydisperse liquid spray*. Journal of Computational Physics. 231: 394-422. 2012.